

INTERNATIONAL JOURNAL OF MODERN ENGINEERING

Spring/Summer 2017
Volume 17, No. 2

The Leading Journal of Engineering, Applied Science and Technology

Industrial

Electronics

Biomedical

Civil

Aerospace

Computer

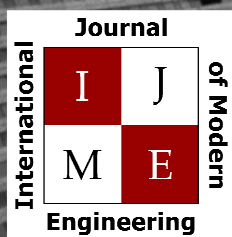
Electrical

Chemical

Mechanical



ENGINEERING



www.ijme.us

Print ISSN: 2157-8052
Online ISSN: 1930-6628



www.iajc.org

INTERNATIONAL JOURNAL OF MODERN ENGINEERING

ABOUT IJME:

- IJME was established in 2000 and is the first and official flagship journal of the International Association of Journal and Conferences (IAJC).
- IJME is a high-quality, independent journal steered by a distinguished board of directors and supported by an international review board representing many well-known universities, colleges and corporations in the U.S. and abroad.
- IJME has an impact factor of **3.00**, placing it among the top 100 engineering journals worldwide, and is the #1 visited engineering journal website (according to the National Science Digital Library).

OTHER IAJC JOURNALS:

- The International Journal of Engineering Research and Innovation (IJERI)
For more information visit www.ijeri.org
- The Technology Interface International Journal (TIIJ).
For more information visit www.tiij.org

IJME SUBMISSIONS:

- Manuscripts should be sent electronically to the manuscript editor, Dr. Philip Weinsier, at philipw@bgsu.edu.

For submission guidelines visit
www.ijme.us/submissions

TO JOIN THE REVIEW BOARD:

- Contact the chair of the International Review Board, Dr. Philip Weinsier, at philipw@bgsu.edu.

For more information visit
www.ijme.us/ijme_editorial.htm

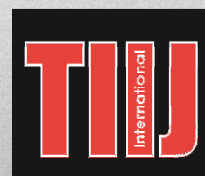
INDEXING ORGANIZATIONS:

- IJME is currently indexed by 22 agencies.
For a complete listing, please visit us at www.ijme.us.

Contact us:

Mark Rajai, Ph.D.

Editor-in-Chief
California State University-Northridge
College of Engineering and Computer Science
Room: JD 4510
Northridge, CA 91330
Office: (818) 677-5003
Email: mrajai@csun.edu



www.tiij.org



www.ijeri.org

INTERNATIONAL JOURNAL OF MODERN ENGINEERING

The INTERNATIONAL JOURNAL OF MODERN ENGINEERING (IJME) is an independent, not-for-profit publication, which aims to provide the engineering community with a resource and forum for scholarly expression and reflection.

IJME is published twice annually (fall and spring issues) and includes peer-reviewed articles, book and software reviews, editorials, and commentary that contribute to our understanding of the issues, problems, and research associated with engineering and related fields. The journal encourages the submission of manuscripts from private, public, and academic sectors. The views expressed are those of the authors and do not necessarily reflect the opinions of the IJME editors.

EDITORIAL OFFICE:

Mark Rajai, Ph.D.
Editor-in-Chief
Office: (818) 677-2167
Email: ijmeeditor@iajc.org
Dept. of Manufacturing Systems
Engineering & Management
California State University-
Northridge
18111 Nordhoff Street
Northridge, CA 91330-8332

THE INTERNATIONAL JOURNAL OF MODERN ENGINEERING EDITORS

Editor-in-Chief:

Mark Rajai

California State University-Northridge

Associate Editors:

Alok Verma

Old Dominion University

Li Tan

Purdue University Northwest

Production Editor:

Philip Weinsier

Bowling Green State University-Firelands

Subscription Editor:

Morteza Sadat-Hossieny

Northern Kentucky University

Web Administrator:

Saeed Namyar

Advanced Information Systems

Executive Editor:

Paul Wilder

Vincennes University

Manuscript Editor:

Philip Weinsier

Bowling Green State University-Firelands

Copy Editor:

Li Tan

Purdue University Northwest

Technical Editors:

Michelle Brodke

Bowling Green State University-Firelands

Marilyn Dyrud

Oregon Institute of Technology

Publisher:

Bowling Green State University Firelands

TABLE OF CONTENTS

<i>Editor's Note (In This Issue): Modeling Critical Responses of High-Rise Buildings</i>	3
Philip Weinsier, IJME Manuscript Editor	
<i>Simplified Transient Two-Phase Model for Pipe Flow</i>	5
Olusola Oloruntoba, Cranfield University; Fuat Kara, Cranfield University	
<i>Effect of Temperature on Elastic and Yielding Behavior of Epoxy Using a Reactive Force Field</i>	13
Olanrewaju Aluko, University Of Michigan-Flint; Shankara Gowtham, Michigan Technological University; Gregory Odegard, Michigan Technological University	
<i>Improving FiWi Access Network Downstream Performance: A Distributed Approach</i>	20
ASM Delowar Hossain, City University of New York; Muhammad Ummy, City University of New York; Abdullah Hossain, City University of New York	
<i>Probabilistic Models for Critical Responses of High-Rise Buildings</i>	26
Mohammad T Bhuiyan, West Virginia State University; Roberto Leon, Virginia Tech	
<i>Phase Transitions in Interconnection Networks with Finite Buffers</i>	33
Yelena Rykalova, UMass Lowell; Lev B. Levitin, Boston University	
<i>Gate Drive and Efficiency Analysis for a Silicon Carbide MOSFET-Based Electric Motor Drive</i>	41
Todd D. Batzel, Pennsylvania State University, Altoona College; Taylor R. Leach, Pennsylvania State University, Altoona College	
<i>Modeling Fluid Flow through a Flexible Tube</i>	53
Abdessamad Mehdari, Mohammed V University; Mohamed Hasnaoui, Royal Air Force School; Mohamed Agouzoul, Mohammed V University	
<i>Short-Term Forecasting of Wind Power Generation by Adaptive Neural Networks</i>	59
Hong Li, The City University of New York; Ali Setoodehnia, ECPI University	
<i>Instructions for Authors: Manuscript Submission Guidelines and Requirements</i>	65

IN THIS ISSUE (P.26)

MODELING CRITICAL RESPONSES OF HIGH-RISE BUILDINGS

Philip Weinsier, IJME Manuscript Editor

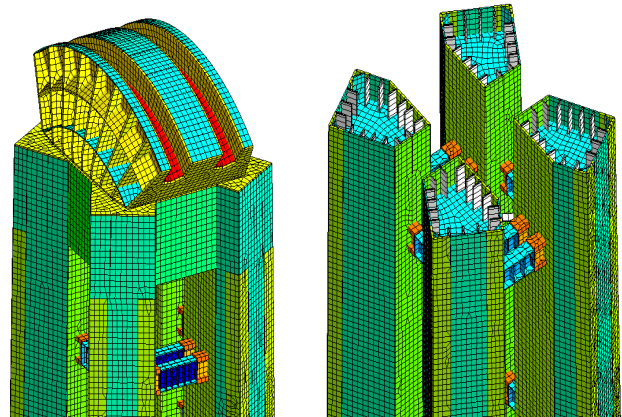
In the most recent issues of IJME and its sister journal, IJERI (the International Journal of Engineering Research and Innovation), we published two other articles related to tall buildings or structures. [*The Effects of Anchor Rod Failure on the Performance of the New Bay Bridge Tower* (Astaneh-Asl et al. IJME fall/winter 2016 v17 n1 p.37). *Pushover Analysis of the New Self-Anchored Suspension Bay Bridge Tower* (Astaneh-Asl and Qian, IJERI fall/winter 2016 v8 n2 p.62).] If you haven't already, I encourage you to read each of those articles as well as, of course, the one noted in this current issue.



The New Bay Bridge Tower

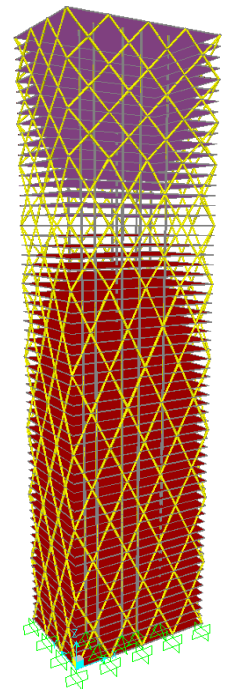
I don't feel out of line by suggesting that everyone understands the importance of safety, when it comes to infrastructure in this country. I also feel safe in saying that we tend to take it for granted. You drive across a bridge, you don't worry that you might not make it to the other side. You stay on the 20th floor of a hotel, you don't worry about the rock collection in your suitcase causing the structure to collapse in on you. But stop and think for a minute about other countries. Whether or not you've been there in person or not—though I have been—even if you've only seen images on TV, there are plenty of places in the world where building codes are either lax or nonexistent.

How about the terrorist attacks on the World Trade Center towers? Is it possible that the structures could have survived the attacks, had they been built better? The answer is actually yes, as was explained to us by the only structural engineer allowed to examine the carnage on site, and who presented his findings to us as the keynote speaker at our 2016 IAJC international conference. Dr. Astaneh-Asl also happens to be the author of two of the articles noted here.



From the studies I've noted, the images above show a finite element model of the SAS Bay Bridge tower in San Francisco, CA. On the left is the tower's saddle and grillage; on the right is a cross-section of the tower's grillage. All critical structural components of the main tower, including all three types of shear links, vertical stiffeners of the tower shafts, and horizontal diaphragms inside the tower shafts, were modeled.

The authors of the article in this current issue (*Probabilistic Models for Critical Responses of High-Rise Buildings*, p.26) present their findings on probabilistic performance-based design and assessment of structures, taking into account the uncertainty in the estimation of seismic hazards, structural response (as a function of the ground motion intensity level), and structural capacity. The objective of this study was to develop statistical models for critical building responses (such as roof drift, roof acceleration, base shear, etc.) which might help in the development and/or assessment of guidelines for the seismic design of high-rise buildings. This image shows a statistical model for critical building responses such as roof drift, roof acceleration, and base shear for the 64-story building used in this study.



Editorial Review Board Members

Mohammed Abdallah	State University of New York (NY)	Gengehen Liu	University of California-Davis (CA)
Nasser Alaraje	Michigan Tech (MI)	Guoxiang Liu	University of North Dakota (ND)
Ammar Al-Farga	University of Jiangnan (CHINA)	Louis Liu	University of New Orleans (LA)
Aly Mousaad Aly	Louisiana State University (LA)	Peng Liu	Washington State University (WA)
Paul Akangah	North Carolina A&T State University (NC)	Mani Manivannan	ARUP Corporation
Lawal Anka	Zamfara AC Development (NIGERIA)	G.H. Massiha	University of Louisiana (LA)
Jahangir Ansari	Virginia State University (VA)	Jim Mayrose	Buffalo State College (NY)
Kevin Berisso	Ohio University (OH)	Thomas McDonald	University of Southern Indiana (IN)
Pankaj Bhambri	Guru Nanak Dev Engineering (INDIA)	David Melton	Eastern Illinois University (IL)
Water Buchanan	Texas A&M University (TX)	Shokoufeh Mirzaei	Cal State Poly Pomona (CA)
John Burningham	Clayton State University (GA)	Bashir Morshed	University of Memphis (TN)
Shaobiao Cai	Penn State University (PA)	Sam Mryyan	Excelsior College (NY)
Vigyana Chandra	Eastern Kentucky University (KY)	Jessica Murphy	Jackson State University (MS)
Isaac Chang	Illinois State University (IL)	Wilson Naik	University of Hyderabad (INDIA)
Shu-Hui (Susan) Chang	Iowa State University (IA)	Arun Nambiar	California State University Fresno (CA)
Bin Chen	Purdue University Northwest (IN)	Ramesh Narang	Indiana University-Purdue University (IN)
Wei-Yin Chen	University of Mississippi (MS)	Anand Nayyar	Institute Management and Tech (INDIA)
Rigoberto Chinchilla	Eastern Illinois University (IL)	Aurenice Oliveira	Michigan Tech (MI)
Phil Cochrane	Indiana State University (IN)	Reynaldo Pablo	Indiana University-Purdue University (IN)
Emily Crawford	Southern Wesleyan University (SC)	Basile Panoutsopoulos	Community College of Rhode Island (RI)
Brad Deken	Southeast Missouri State University (MO)	Shahera Patel	Sardar Patel University (INDIA)
Z.T. Deng	Alabama A&M University (AL)	Jose Pena	Purdue University Calumet (IN)
Sagar Deshpande	Ferris State University (MI)	Karl Perusich	Purdue University (IN)
David Domermuth	Appalachian State University (NC)	Thongchai Phairoh	Virginia State University (VA)
Dongliang Duan	University of Wyoming (WY)	Huyu Qu	Honeywell Corporation
Marilyn Dyrud	Oregon Institute of Technology (OR)	John Rajadas	Arizona State University (AZ)
Mehran Elahi	Elizabeth City State University (NC)	Vijaya Ramnath	Sri Sairam Engineering College (CHENNAI)
Ahmed Elsayy	Tennessee Technological University (TN)	Desire Rasolomampionona	Warsaw University of Tech (POLAND)
Rasoul Esfahani	DeVry University (OH)	Mohammad Razani	New York City College of Tech (NY)
Dominick Fazarro	Sam Houston State University (TX)	Sangram Redkar	Arizona State University-Poly (AZ)
Ignatius Fomunung	University of Tennessee Chattanooga (TN)	Michael Reynolds	University of Arkansas Fort Smith (AR)
Ahmed Gawad	Zagazig University EGYPT	Nina Robson	California State University-Fullerton (CA)
Daba Gedafa	University of North Dakota (ND)	Marla Rogers	Wireless Systems Engineer
Mohsen Hamidi	Utah Valley University (UT)	Dale Rowe	Brigham Young University (UT)
Mamoon Hammad	Abu Dhabi University (UAE)	Karen Ruggles	DeSales University (PA)
Gene Harding	Purdue Polytechnic (IN)	Anca Sala	Baker College (MI)
Youcef Himri	Safety Engineer in Sonelgaz (ALGERIA)	Alex Sergeev	Michigan Technological University (MI)
Xiaobing Hou	Central Connecticut State University (CT)	Hiral Shah	St. Cloud State University (MN)
Shelton Houston	University of Louisiana Lafayette (LA)	Siles Singh	St. Joseph University Tanzania (AFRICA)
Kun Hua	Lawrence Technological University (MI)	Ahmad Sleiti	University of North Carolina Charlotte (NC)
Ying Huang	North Dakota State University (ND)	Jiahui Song	Wentworth Institute of Technology (MA)
Dave Hunter	Western Illinois University (IL)	Yuyang Song	Toyota Corporation
Christian Hyeng	North Carolina A&T University (NC)	Carl Spezia	Southern Illinois University (IL)
Pete Hylton	Indiana University Purdue (IN)	Michelle Surerus	Ohio University (OH)
Ghassan Ibrahim	Bloomsburg University (PA)	Jalal Taheri	Bostan Abad Islamic Azad University (IRAN)
John Irwin	Michigan Tech (MI)	Li Tan	Purdue University Northwest (IN)
Toqeer Israr	Eastern Illinois University (IL)	Harold Terano	Camarines Sur Polytechnic (NABUA)
Sudershan Jetley	Bowling Green State University (OH)	Sanjay Tewari	Louisiana Tech University (LA)
Rex Kanu	Ball State University (IN)	Vassilios Tzouanas	University of Houston Downtown (TX)
Tolga Kaya	Central Michigan University (MI)	Jeff Ulmer	University of Central Missouri (MO)
Satish Ketkar	Wayne State University (MI)	Mihaela Vorvoreanu	Purdue University (IN)
Manish Kewalramani	Abu Dhabi University (UAE)	Phillip Waldrop	Georgia Southern University (GA)
Tae-Hoon Kim	Purdue University Northwest (IN)	Abraham Walton	Purdue University (IN)
Chris Kluse	Bowling Green State University (OH)	Haoyu Wang	Central Connecticut State University (CT)
Doug Koch	Southeast Missouri State University (MO)	Liangmo Wang	Nanjing University of Science/Tech (CHINA)
Ognjen Kuljaca	Brodarski Institute (CROATIA)	Boonsap Witchayangkoon	Thammasat University (THAILAND)
Chakresh Kumar	Uttar Pradesh Tech University (INDIA)	Alex Wong	Digilent Inc.
Zaki Kuruppallil	Ohio University (OH)	Shuju Wu	Central Connecticut State University (CT)
Edward Land	Johns Hopkins Medical Institute	Baijian "Justin" Yang	Ball State University (IN)
Jane LeClair	Excelsior College (NY)	Eunice Yang	University of Pittsburgh Johnstown (PA)
Shiyoun Lee	Penn State University Berks (PA)	Mijia Yang	North Dakota State University (ND)
Soo-Yen Lee	Central Michigan University (MI)	Xiaoli (Lucy) Yang	Purdue University Northwest (IN)
Solomon Leung	Idaho State University (ID)	Faruk Yildiz	Sam Houston State University (TX)
Chao Li	Florida A&M University (FL)	Yuqui You	Morehead State University (KY)
Jimmy Linn	Eastern Carolina University (NC)	Pao-Chiang Yuan	Jackson State University (MS)
Dale Litwhiler	Penn State University (PA)	Jinwen Zhu	Missouri Western State University (MO)

SIMPLIFIED TRANSIENT TWO-PHASE MODEL FOR PIPE FLOW

Olusola Oloruntoba, Cranfield University; Fuat Kara, Cranfield University

Abstract

Two-phase flow analyses are critical to successful design and operations of two-phase and multiphase pipe flow applications found in major industrial fields, such as petroleum, nuclear, chemical, geothermal and space industries. Due to difficulties in obtaining analytical transient solutions, approximate solutions have been applied to two-phase pipe flow. However, these approximate solutions neglect convective terms in two-phase Navier-Stokes equations. The aim of this current study was to develop transient tools to predict transient two-phase pipe flow. The objectives of this study were to develop a simplified transient model and to validate the proposed model with published experimental data. A simplified transient two-phase pipe flow model was obtained in this study by simplifying the two-phase Navier-Stokes equations. The simplified equations include: (i) a transient continuity equation of combined two-phase flow that includes two new dimensionless terms; (ii) transient two-phase momentum equations that account for convective terms only; and, (iii) a steady state pressure gradient.

Introduction

Multiphase flow occurs in major industrial fields, including the petroleum, chemical, geothermal, nuclear, and space industries. Steady state and transient prediction models are required for adequate design of these multiphase applications in these industries [1, 2]. Unfortunately, rigorous analytical solutions are limited to but a few flow scenarios. Numerical methods provide approximate solutions but are limited, due to high demand for computational time and resources; especially for transient simulations [3]. Mechanistic methods, which rely on physical analyses based on flow pattern, have been successfully applied for steady state flows [1]. Therefore, simplified transient models have been sought after to achieve fast transient simulators.

Taitel et al. [4] proposed a simplified transient two-phase model that treats liquid continuity as the only transient equation; momentum equations for gas and liquid, and a gas continuity equation were treated in a quasi-steady state. These assumptions are valid for slow transient flow variations. The model of Taitel et al. was modified by Minami and Shoham [5] using an implicit scheme instead of an explicit scheme implemented in the original model. Minami

and Shoham also developed a new flow regime transition model for transient flow. The modified model from Taitel et al. was tested against experimental data collected in a 420m long and 7.79 cm diameter pipe, in an air-kerosene two-fluid system. The validation results showed good agreement between their model and the experimental data, with the exception of the liquid blowdown test. During the liquid blowdown test, when the liquid flow rate is set to zero with the gas flow rate sustained, complete liquid removal was not achieved. Li [6] developed a simplified two-phase transient model by treating continuity equations as transient, but with momentum equations in a quasi-steady state. Li validated this model using the data from Vigneron et al. [7]. Later, Choi et al. [8] developed a simplified transient two-phase model to solve modified continuity equations, but treated momentum equations as an extended drift flux equation in the quasi-steady state.

Existing simplified transient models assume complete quasi-steady state conditions for momentum equations. Consequently, an alternative simplified transient two-phase model can be developed by considering convective terms in momentum equations, as well as continuity equations in the transient state. This alternative simplified transient model was developed in this study.

Model Description

Navier-Stokes Equations

One-dimensional two-phase Navier-Stokes equations [3], with negligible contribution from the energy equation and mass transfer between the phases, were considered and are presented in the continuity equations of Equations (1) and (2), and the momentum equations of Equations (3) and (4):

$$\frac{\partial}{\partial t}(\rho_G \alpha_G) + \frac{\partial}{\partial x}(\rho_G \alpha_G U_G) = 0 \quad (1)$$

$$\frac{\partial}{\partial t}(\rho_L \alpha_L) + \frac{\partial}{\partial x}(\rho_L \alpha_L U_L) = 0 \quad (2)$$

$$\begin{aligned} \frac{\partial}{\partial t}(\rho_G \alpha_G U_G) + \frac{\partial}{\partial x}(\rho_G \alpha_G U_G^2) \\ = -\alpha_G \frac{\partial P_G}{\partial x} - \tau_{GW} - \tau_{GL} - \alpha_G \rho_G g \sin \theta \end{aligned} \quad (3)$$

$$\begin{aligned} \frac{\partial}{\partial t}(\rho_L \alpha_L U_L) + \frac{\partial}{\partial x}(\rho_L \alpha_L U_L^2) \\ = -\alpha_L \frac{\partial P_L}{\partial x} - \tau_{LW} + \tau_{GL} - \alpha_L \rho_L g \sin \theta \end{aligned} \quad (4)$$

Modified Navier-Stokes Equations

The Navier-Stokes equations presented in Equations (1)-(4) consist of four equations, with eight unknown variables, namely: ρ_G , ρ_L , α_G , α_L , U_G , U_L , P_G , and P_L . To simplify the Navier-Stokes, and to achieve zero degrees of freedom, the following modifications were introduced.

Modifications introduced from previous studies:

- Incompressible flow was assumed [3]
- Superficial velocities are defined as $U_{SG} = \alpha_G U_G$ and $U_{SL} = \alpha_L U_L$ [1]
- Steady state pressure gradient was assumed (valid for slowly varying flow, such as in the petroleum industry [1])
- Single pressure applies to gas and liquid by $P_G = P_L = P$ [9]
- Summation of phase fractions is unity, given as $\alpha_G + \alpha_L = 1$ [3]

Modifications introduced in this study:

- In this study, the average of Equations (1) and (2) was determined in order to obtain a combined continuity equation; noting that incompressibility was assumed and that $\alpha_G = 1 - \alpha_L$.
- Two new dimensionless terms, α_L / H_L and $(1 - \alpha_L)/(1 - H_L)$, were introduced in the combined continuity equation. This was aimed at introducing transient liquid holdup dependence on liquid holdup distribution along the length of the pipe. The dimensionless terms represent ratio of transient phase fraction to steady state phase fraction. Theoretically, these terms should converge to unity, as transient simulations approach steady state conditions.
- Convective terms in the momentum equations—Equations (3)-(4)—were retained as part of the simplified transient model.

Application of these modifications to Equations (1)-(4) yields the simplified transient two-phase model, as presented by the combined continuity equation of Equation (5) and the simplified momentum equations of Equations (6) and (7):

The conservation variables are α_L , U_{SG} , and U_{SL} .

$$\frac{\partial}{\partial t}(\alpha_L) - \frac{1}{2\rho_G} \frac{\partial}{\partial x} \left\{ \left(\frac{1-\alpha_L}{1-H_L} \right) \rho_G U_{SG} \right\} + \frac{1}{2\rho_L} \frac{\partial}{\partial x} \left\{ \left(\frac{\alpha_L}{H_L} \right) \rho_L U_{SL} \right\} = 0 \quad (5)$$

$$\frac{\partial}{\partial t}(U_{SG}) + \frac{1}{\rho_G} \frac{\partial}{\partial x} \left\{ \left(\frac{\rho_G}{1-\alpha_L} \right) U_{SG}^2 \right\} = 0 \quad (6)$$

$$\frac{\partial}{\partial t}(U_{SL}) + \frac{1}{\rho_L} \frac{\partial}{\partial x} \left\{ \left(\frac{\rho_G}{\alpha_L} \right) U_{SL}^2 \right\} = 0 \quad (7)$$

where, the steady state pressure gradient equations are given in Equations (8) and (9).

$$-\frac{dP}{dx} = \frac{2f_m \rho_m U_m^2}{D} \quad (8)$$

$$f_m = F_2 + \frac{F_1 - F_2}{\left[1 + \left(\frac{Re}{t^*} \right)^c \right]^d} \quad (9)$$

Equation (8) expresses the steady state pressure gradient model of Garcia et al. [10]. The model of Garcia et al. was employed for its simplicity and applicability to all flow regimes [8]. The friction factor, f_m , is given in Equation (9). The authors defined the following power laws: $F_1 = a_1 Re^{b_1}$ and $F_2 = a_2 Re^{b_2}$; Reynold's number of mixture flow $Re = U_m D / \nu_L$; mixture velocity $U_m = U_{SG} + U_{SL}$; mixture density $\rho_m = \rho_L \lambda_L + \rho_G (1 - \lambda_L)$; and, kinematic viscosity of liquid $\nu_L = \mu_L / \rho_L$. Coefficients a_1 , b_1 , a_2 , b_2 , c , d , and t^* are defined as 13.98, -0.9501, 0.0925, -0.2534, 4.864, 0.1972, and 293, respectively.

Steady state liquid holdup, H_L , was calculated iteratively using Equation (10) and the method of Choi et al. [11]. An initial guess value of $\alpha_G = 0.5$ was applied. At subsequent iteration steps, $\alpha_G = 1 - H_L$. The distribution parameter, C_0 , is given in Equation (11):

$$H_L = 1 - \frac{U_{SG}}{C_0 U_m + U_D} \quad (10)$$

$$C_0 = \frac{2}{1 + \left(\frac{Re}{1000} \right)^2} + \frac{1.2 - 0.2 \sqrt{\frac{\rho_G}{\rho_L}} (1 - \exp(-18\alpha_G))}{1 + \left(\frac{1000}{Re} \right)^2} \quad (11)$$

Drift velocity, U_D , is given in Equation (12):

$$U_D = A \cos \theta + B \left(\frac{g \sigma (\rho_L - \rho_G)}{\rho_L^2} \right)^{1/4} \cos \theta \quad (12)$$

where, $Re = \rho_L U_m D / \mu_L$ is the Reynold's number and coefficients A and B are given as 0.0246 and 1.606, respectively.

Validation of Steady State Equations

The steady state pressure gradient of Equation (8) was validated using published experimental data [12-15]. The data of Asante [12] consisted of 255 and 243 data points of stratified and annular/mist flow regime, respectively. The experiment was carried out for an oil-water-air flow in a horizontal pipe with a diameter range of 0.0254m - 0.0762m at standard conditions. A total of 38 slug flow data points were obtained from Hernandez [13]. The experiment of Hernandez was carried out for water-air flow in a 0.038m diameter pipe, inclined between 0° and 90°. The data of Marruaz et al. [14] consisted of 23 data points of slug flow regime. The experiment of Marruaz et al. was carried out for oil-water-gas flow in a 0.15m diameter horizontal pipe. The data obtained from Tullius [15] consisted of 101 data points of slug flow regime. The experiment of Tullius was conducted for oil-water-air flow in a 0.101m diameter horizontal pipe.

The average percentage of error is defined in Equation (13):

$$\varepsilon_{ave} = \left(\frac{\text{experimental data} - \text{prediction}}{\text{prediction}} \right) \times 100 \% \quad (13)$$

Figure 1 shows that the validation results from Equation (8) predict 83% of experimental pressure gradient data within $-30\% \leq \hat{a}_{ave} \leq +30\%$.

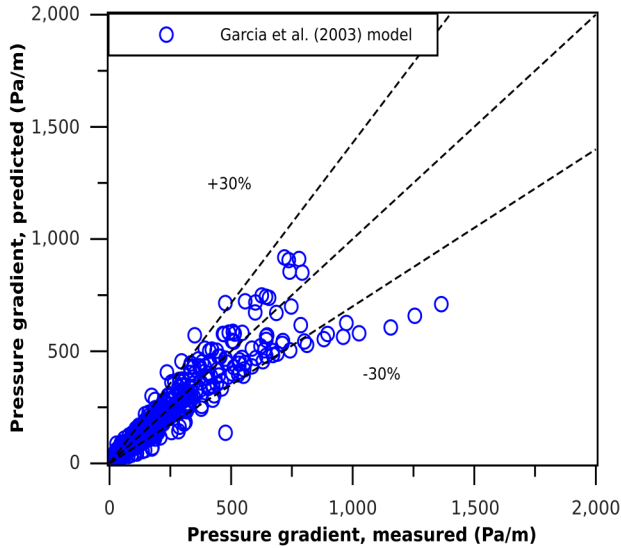


Figure 1. Validation of the Steady State Pressure Gradient Model Given in Equation (8)

Numerical Discretization

The proposed simplified transient two-phase model was discretized using a finite volume upwind scheme, with a scattered grid arrangement in the spatial domain. Time marching was implemented explicitly. Equation (14) is the combined continuity equation. Equations (15) and (16) are the simplified momentum equations of gas and liquid, respectively. Slope limiter, β , was defined for gas and liquid velocities at computational nodes in order to determine flow directions [3]. For example, gas slope limiter at volume node $(i + 1/2)$ was defined as

$$\beta_{i+1/2}^G = (U_{SG})_{i+1/2}^n / |(U_{SG})_{i+1/2}^n|$$

$$\frac{(\alpha_L)_i^{n+1} - (\alpha_L)_i^n}{\Delta t} =$$

$$A_1 \left((U_{SG})_{i-1/2}^n \left[1 - (\alpha_L)_{i-1}^n \right] \right)$$

$$+ A_2 \left((U_{SG})_{i+1/2}^n \left[1 - (\alpha_L)_i^n \right] \right) \quad (14)$$

$$+ A_3 \left((U_{SL})_{i-1/2}^n (\alpha_L)_{i-1}^n \right)$$

$$+ A_4 \left((U_{SL})_{i+1/2}^n (\alpha_L)_i^n \right)$$

where,

$$A_1 = \left(\frac{1}{2\rho_G} \right)_i \left(\frac{-1}{\Delta x} \right)_i \left\{ \left(\frac{1 + \beta_{i-1/2}^G}{2} \right) \left(\frac{\rho_G}{1 - H_L} \right)_{i-1} + \left(\frac{1 - \beta_{i-1/2}^G}{2} \right) \left(\frac{\rho_G}{1 - H_L} \right)_i \right\}^n$$

$$A_2 = \left(\frac{1}{2\rho_G} \right)_i \left(\frac{1}{\Delta x} \right)_i \left\{ \left(\frac{1 + \beta_{i+1/2}^G}{2} \right) \left(\frac{\rho_G}{1 - H_L} \right)_i + \left(\frac{1 - \beta_{i+1/2}^G}{2} \right) \left(\frac{\rho_G}{1 - H_L} \right)_{i-1} \right\}^n$$

$$A_3 = \left(\frac{1}{2\rho_L} \right)_i \left(\frac{1}{\Delta x} \right)_i \left\{ \left(\frac{1 + \beta_{i-1/2}^L}{2} \right) \left(\frac{\rho_L}{H_L} \right)_{i-1} + \left(\frac{1 - \beta_{i-1/2}^L}{2} \right) \left(\frac{\rho_L}{H_L} \right)_i \right\}^n$$

$$A_4 = \left(\frac{1}{2\rho_L} \right)_i \left(\frac{-1}{\Delta x} \right)_i \left\{ \left(\frac{1 + \beta_{i+1/2}^L}{2} \right) \left(\frac{\rho_L}{H_L} \right)_i + \left(\frac{1 - \beta_{i+1/2}^L}{2} \right) \left(\frac{\rho_L}{H_L} \right)_{i-1} \right\}^n$$

$$\frac{(U_{SG})_{i+1/2}^{n+1} - (U_{SG})_{i+1/2}^n}{\Delta t} = B_1 \left\{ \frac{\left[(U_{SG})_{i-1/2}^n \right]^2}{1 - (\alpha_L)_{i-1/2}^n} \right\} \quad (15)$$

$$+ B_2 \left\{ \frac{\left[(U_{SG})_{i+1/2}^n \right]^2}{1 - (\alpha_L)_{i+1/2}^n} \right\} + B_3 \left\{ \frac{\left[(U_{SG})_{i+3/2}^n \right]^2}{1 - (\alpha_L)_{i+3/2}^n} \right\}$$

where,

$$B_1 = \left(\frac{1}{\rho_G} \right)_{i+\frac{1}{2}}^n \left(\frac{1}{\Delta x} \right)_{i+\frac{1}{2}} \left\{ \left(\frac{1 + \beta_{i+\frac{1}{2}}^G}{2} \right) (\rho_G)_{i-\frac{1}{2}} \right\}^n$$

$$B_2 = \left(\frac{1}{\rho_G} \right)_{i+\frac{1}{2}}^n \left(\frac{-1}{\Delta x} \right)_{i+\frac{1}{2}} \left\{ \beta_{i+\frac{1}{2}}^G (\rho_G)_{i+\frac{1}{2}} \right\}^n$$

$$B_3 = \left(\frac{1}{\rho_G} \right)_{i+\frac{1}{2}}^n \left(\frac{-1}{\Delta x} \right)_{i+\frac{1}{2}} \left\{ \left(\frac{1 - \beta_{i+\frac{1}{2}}^G}{2} \right) (\rho_G)_{i+\frac{3}{2}} \right\}^n$$

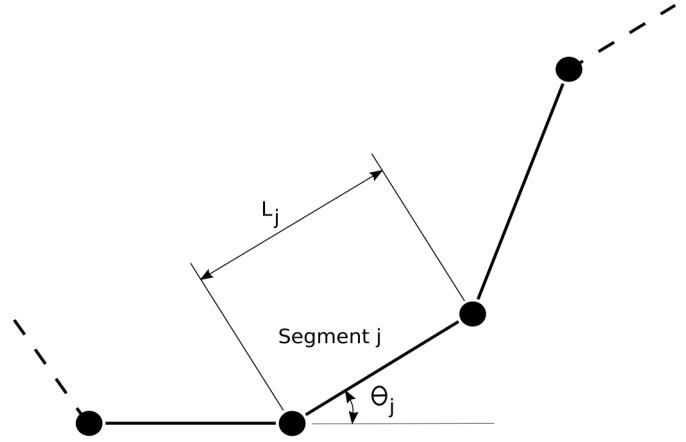


Figure 2. Pipe Profile Divided into Segments: L_j = Length of Segment j [m]; θ_j = Inclination Angle of Segment j [degree]

$$\frac{(U_{SL})_{i+\frac{1}{2}}^{n+1} - (U_{SL})_{i+\frac{1}{2}}^n}{\Delta t} = C_1 \left\{ \frac{[(U_{SL})_{i-\frac{1}{2}}^n]^2}{(\alpha_L)_{i-\frac{1}{2}}^n} \right\} \quad (16)$$

$$+ C_2 \left\{ \frac{[(U_{SL})_{i+\frac{1}{2}}^n]^2}{(\alpha_L)_{i+\frac{1}{2}}^n} \right\} + C_3 \left\{ \frac{[(U_{SL})_{i+\frac{3}{2}}^n]^2}{(\alpha_L)_{i+\frac{3}{2}}^n} \right\}$$

where,

$$C_1 = \left(\frac{1}{\rho_L} \right)_{i+\frac{1}{2}}^n \left(\frac{1}{\Delta x} \right)_{i+\frac{1}{2}} \left\{ \left(\frac{1 + \beta_{i+\frac{1}{2}}^L}{2} \right) (\rho_L)_{i-\frac{1}{2}} \right\}^n$$

$$C_2 = \left(\frac{1}{\rho_L} \right)_{i+\frac{1}{2}}^n \left(\frac{-1}{\Delta x} \right)_{i+\frac{1}{2}} \left\{ \beta_{i+\frac{1}{2}}^L (\rho_L)_{i+\frac{1}{2}} \right\}^n$$

$$C_3 = \left(\frac{1}{\rho_L} \right)_{i+\frac{1}{2}}^n \left(\frac{-1}{\Delta x} \right)_{i+\frac{1}{2}} \left\{ \left(\frac{1 - \beta_{i+\frac{1}{2}}^L}{2} \right) (\rho_L)_{i+\frac{3}{2}} \right\}^n$$

Pipe Geometry and Discretization

Figure 2 shows how the pipe profile was supplied as pipe segments based on pipe inclination angle. Each segment was discretized into elements, such that a uniform grid was obtained.

Boundary Conditions

Figure 3 depicts the computational domain and boundary conditions for the simplified transient two-phase model. The computational domain was $0 \leq x \leq L$. The inlet and outlet boundaries were given for $(\alpha_L, U_{SG}, U_{SL})$ at $x = 0$, and for (P) at $x = L$, respectively. Ghost cells are generally required to estimate conservation variables at the boundaries [3].

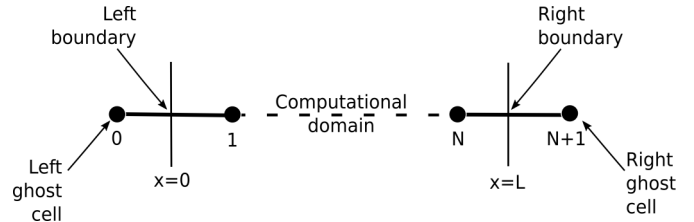


Figure 3. Computational Domain and Boundary Conditions

Sensitivity Analysis

Spatial and temporal sensitivity analyses were carried out for pressure gradient predictions using the proposed simplified transient two-phase model. For the spatial sensitivity analysis, the percentage of relative error was calculated relative to pressure drop at $N + 1 = 656$. For the temporal sensitivity analysis, the computational time ratio was calculated as $t_{ratio} = t_{N+1}/t_{42}$. Figures 4 and 5 present results of the spatial and temporal sensitivity analyses, respectively.

Validation of the Simplified Transient Two-Phase Model

The simplified transient two-phase model proposed in this study was validated using experimental data from Vigneron et al. [7]. The experiment of Vigneron et al. was carried out

in a 0.0779m diameter, 420m long horizontal steel pipeline, using an air-kerosene fluid system. The test station was at 61.4m from the air-kerosene mixing point.

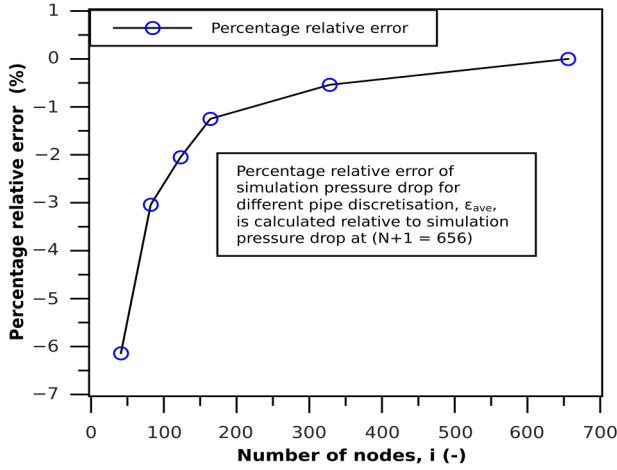


Figure 4. Sensitivity Analysis for the Spatial Steady State Pressure Gradient

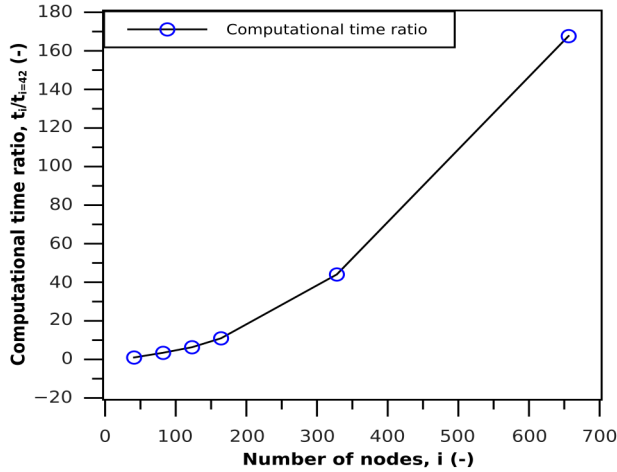


Figure 5. Sensitivity Analysis for the Temporal Steady State Pressure Gradient

Two test cases were used for validation. The first test case (Test 1-B) was at a gas flow rate of 400 Sm³/d and consisted of initial and final liquid flows rate at 8.4 m³/d and 31.8 m³/d, respectively. The corresponding initial and final flow regimes were stratified smooth and stratified wavy, respectively. The second test case (Test 1-C) was at a gas flow rate of 4055 Sm³/d and consisted of initial and final liquid flow rates at 8.4 m³/d and 32 m³/d, respectively. The stratified wavy flow regime was observed for the initial and final liquid flow rates.

Transient Algorithm

Figure 6 shows the algorithm for implementing the simplified transient two-phase model.

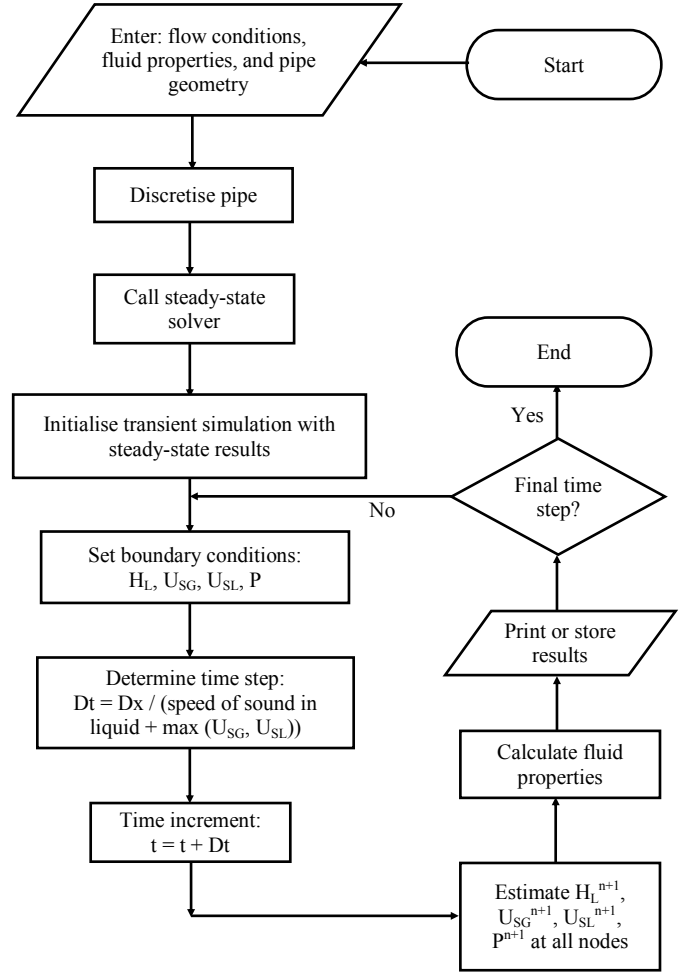


Figure 6. Algorithm for the Simplified Transient Two-Phase Model

Results and Discussion

Figures (7)-(8) and Figures (9)-(10) show predictions of the proposed simplified transient two-phase model for test cases 1-B and 1-C, respectively. Figure 7 shows the prediction of the proposed simplified transient two-phase model for pressure at test stations for test case 1-B. The figure also shows that the proposed model predicted experimental pressure data at $\epsilon_{ave} = -4.07\%$ and $\epsilon_{ave} = -4.40\%$ for initial (I) and final (F) flow conditions, respectively. Figure 8 shows a similar prediction for liquid holdup at $\epsilon_{ave} = 33.57\%$ and $\epsilon_{ave} = 41.00\%$, for initial and final flow, respectively.

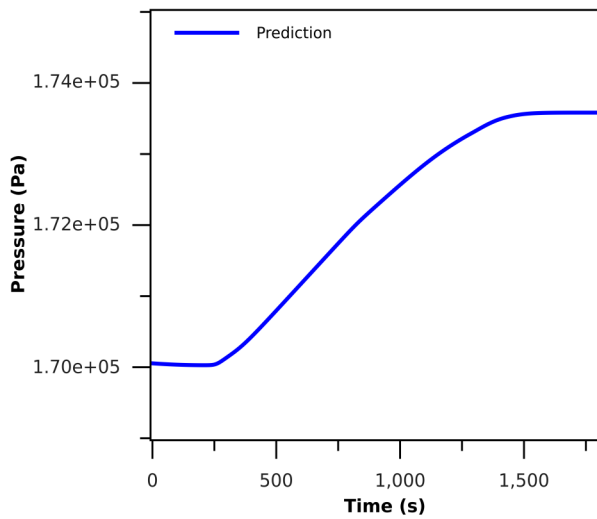


Figure 7. Simplified Transient Model Compared with Experimental Data [7] (pressure results for test 1-B)

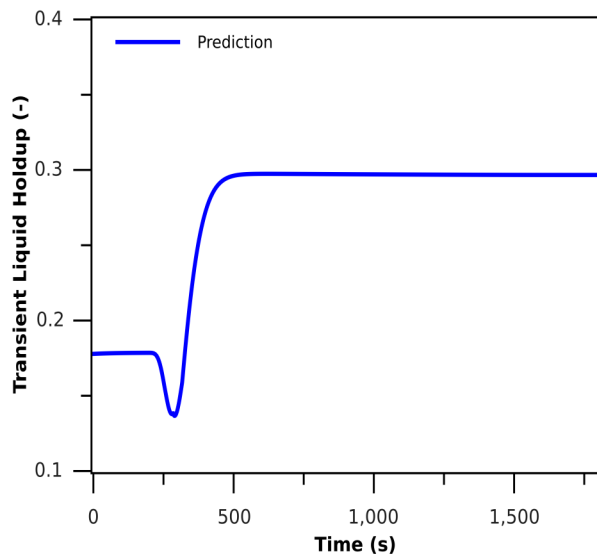


Figure 8. Simplified Transient Model (liquid holdup results for test 1-B)

Figure 9 shows the prediction of the proposed simplified transient two-phase model for pressure at test stations for test case 1-C. The result showed that the proposed simplified transient two-phase model predicts experimental pressure data at $\varepsilon_{ave} = 1.91\%$ and $\varepsilon_{ave} = -3.32\%$, for initial (I) and final (F) flow conditions, respectively. Figure 10 shows a similar prediction for liquid holdup at $\varepsilon_{ave} = -54.84\%$ and $\varepsilon_{ave} = -11.92\%$, for initial and final flow, respectively.

Conclusions

Based on the simplifications to the two-phase Navier-Stokes equations, a simplified transient two-phase model was obtained, which was capable of predicting pressure and liquid holdup.

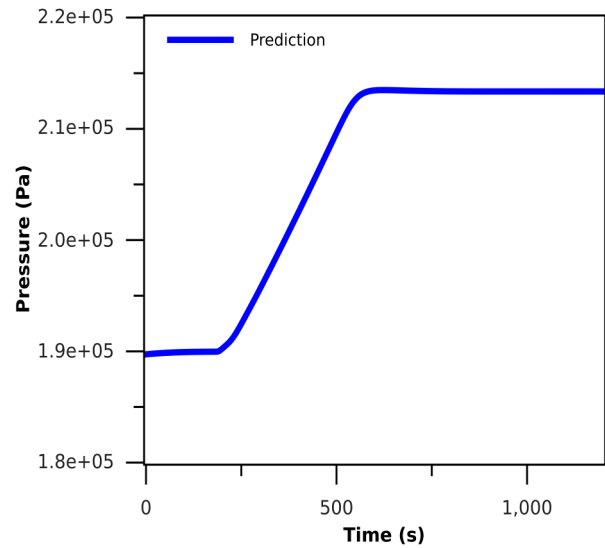


Figure 9. Simplified Transient Model (pressure results for test 1-C)

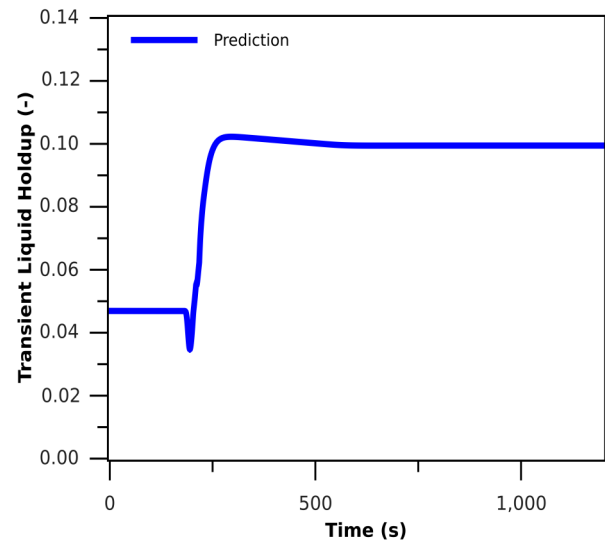


Figure 10. Simplified Transient Model Compared with Experimental Data [7] (liquid holdup results for test 1-C)

Nomenclature

α_G	=	Gas fraction [-]
α_L	=	Liquid fraction or transient liquid holdup [-]
β	=	Slope limiter to determine flow direction [-]
C_0	=	Coefficient of Bubble distribution in flow [-]
D	=	Internal diameter of pipe [m]
ε_{ave}	=	Average percentage error [%]
f_m	=	Friction factor of mixture flow in pipe [-]
g	=	Acceleration due to gravity [m/s ²]
H_L	=	Steady state liquid holdup [-]
λ_L	=	No-slip liquid holdup [-]
μ_G	=	Gas viscosity [Pa.s]
μ_L	=	Liquid viscosity [Pa.s]
ν_L	=	Kinematic viscosity [m ² /s]
N	=	Number of elements in computational domain
$N + 1$	=	Number of nodes in computational domain
P	=	Pressure [Pa]
P_G	=	Gas pressure [Pa]
P_L	=	Liquid pressure [Pa]
P_{sep}	=	Separator Pressure [bar]; 1 bar \equiv 100000 Pa
θ	=	Angular inclination of pipe [degree]
ρ_G	=	Gas density [Kg/m ³]
ρ_L	=	Liquid density [Kg/m ³]
ρ_m	=	Density of gas-liquid mixture [Kg/m ³]
Re	=	Reynolds number [-]
σ	=	Surface tension [N/m]
t	=	time [s]
t_{N+1}	=	computation time at $N+1$ pipe discretization [s]
t_{42}	=	computation time at 42 pipe discretization [s]
τ_{GW}	=	Gas-wall shear stress [Pa]
τ_{GL}	=	Gas-liquid interface shear stress [Pa]
τ_{LW}	=	Liquid-wall shear stress [Pa]
U_D	=	Drift velocity [m/s]
U_G	=	Gas velocity [m/s]
U_L	=	Liquid velocity [m/s]
U_m	=	Mixture velocity [m/s]
U_{SG}	=	Gas superficial velocity [m/s]
U_{SL}	=	Liquid superficial velocity [m/s]
x, L	=	Length [m]
Δt	=	time step [s]
Δx	=	spatial increment [m]

Superscript

n	=	Previous time step
$n+1$	=	Current time step
G	=	Gas
L	=	Liquid

Subscript

i	=	node of discretized pipe
j	=	element of discretized pipe

References

- [1] Shoham, O. (2005). *Mechanistic modeling of gas-liquid two-phase flow in pipes*. Society of Petroleum Engineers.
- [2] Brill, J. P. (1987). *Multiphase Flow in Wells*. Society of Petroleum Engineers.
- [3] Prosperetti, A., & Tryggvason, G. (2007). *Computational Methods for Multiphase Flow*. Cambridge University Press.
- [4] Taitel, Y., Shoham, O., & Brill, J. P. (1989). Simplified transient solution and simulation of two-phase flow in pipelines. *Chemical Engineering Science*, 44 (6), 1353–1359.
- [5] Minami, K., & Shoham, O. (1994). Transient two-phase flow behavior in pipelines-experiment and modeling. *International Journal of Multiphase*, 20(4), 739-752.
- [6] Li, M. (2010, May). *Transient Two-Phase Flow Modeling*. In Seventy Sixth Semi-Annual Advisory Board Meeting Brochure and Presentation, Tulsa University Fluid Flow Projects.
- [7] Vigneron, F., Sarica, C., & Brill, J. P. (1995, June). Experimental analysis of imposed two-phase flow transients in horizontal pipelines. *In the 7th International Conference, Multiphase* (pp. 199-217).
- [8] Choi, J., Pereyra, E., Sarica, C., Lee, H., Jang, I. S., & Kang, J. (2013). Development of a fast transient simulator for gas-liquid two-phase flow in pipes. *Journal of Petroleum Science and Engineering*, 102, 27-35.
- [9] Bendiksen, K. H., Maines, D., Moe, R., & Nuland, S. (1991). The dynamic two-fluid model OLGA: Theory and application. *SPE Production Engineering*, 6 (02), 171-180.
- [10] Garcia, F., Garcia, R., Padrino, J. C., Mata, C., Tralero, J. L., & Joseph, D. D. (2003). Power law and composite power law friction factor correlations for laminar and turbulent gas-liquid flow in horizontal pipelines. *International Journal of Multiphase Flow*, 29(10), 1605-1624.
- [11] Choi, J., Pereyra, E., Sarica, C., Park, C., & Kang, J. M. (2012). An efficient drift-flux closure relationship to estimate liquid holdups of gas-liquid two-phase flow in pipes. *Energies*, 5(12), 5294-5306.
- [12] Asante, B. (2000). *Multiphase Transport of gas and Low Loads of Liquids in Pipelines*. Unpublished doctoral dissertation, University of Calgary.
- [13] Hernandez Perez, V. (2008). *Gas-liquid two-phase flow in inclined pipes*. Unpublished doctoral dissertation, University of Nottingham.
- [14] Marruaz, K. S., Gonçalves, M. A., Ribeiro, G. S., França, F. A., & Rosa, E. S. (2001). Horizontal slug

flow in a large-size pipeline: experimentation and modeling. *Journal of the Brazilian Society of Mechanical Sciences*, 23(4), 481-490.

- [15] Tullius, L. (2000). *A study of drag reducing agents in multiphase flow in large diameter horizontal pipelines*. Unpublished doctoral dissertation, Ohio University.

Biographies

OLUSOLA OLORUNTOBA received his MSc degree in Offshore and Ocean Technology from Cranfield University in 2012. His areas of research are related to subsea engineering, flow assurance, and computational modeling. Olusola may be reached at o.a.oloruntoba@cranfield.ac.uk

FUAT KARA is a lecturer at Cranfield University. Fuat's research areas are related to subsea engineering, pipeline engineering, fluid-structure interaction, marine hydrodynamics, marine hydroelasticity, and offshore renewable energy systems (offshore wind, wave, and tidal devices). Fuat may be reached at f.kara@cranfield.ac.uk

EFFECT OF TEMPERATURE ON ELASTIC AND YIELDING BEHAVIOR OF EPOXY USING A REACTIVE FORCE FIELD

Olanrewaju Aluko, University Of Michigan-Flint; Shankara Gowtham, Michigan Technological University;
Gregory Odegard, Michigan Technological University

Abstract

The crosslinked and relaxed molecular models of the EPON 862 and DETDA system were constructed using a computational molecular dynamics method under a reactive force field. The methodologies for evaluating and validating the models are described, and the effect of temperature on the elastic and yielding behavior of EPON/DETDAs structures are presented. The elastic properties of epoxy materials, such as Young's modulus and Poisson's ratio, and also the yield strength, showed a remarkable response to temperature changes. The predicted data were validated with experimental data found in the literature.

Introduction

Materials that have high strength but low weight are in high demand in today's high-technological industries, such as aerospace, medicine, and automotive. These demands have led to use of fiber-reinforced composites with polymeric matrices, as engineers strive to create products with the ability to meet the requirements for structural components. Researchers have begun to focus on fiber-reinforced epoxy composite materials [1-20], due to their high modulus and strength per unit weight. The computational molecular dynamics method can be used to enhance the performance capability of epoxy materials under different force fields. Abbott et al. [1] documented a general method for structural generation of amorphous polymers using simulated polymerization and a multi-step molecular dynamics equilibration, a method that favors high- T_g polymers. The simulations were validated with experiments for different structural, adsorption, and thermal properties.

Yarovsky and Evans [2] devised a method that was used in low molecular weight water-soluble epoxy resins, crosslinked with different hardening agents that are being considered for use as a primer coating on steel. Their simulations can be applied to predict the crosslink density and the amount of free crosslinking sites in the coatings. The barrier properties of model coatings were predicted and the shrinkage of the resin upon curing was reproduced. Their methodology has the potential to enhance the design and production

of new coatings with better barriers and adhesion characteristics. Varshney et al. [3] studied a crosslinking procedure using a consistent valence force field (CVFF) and predicted molecular and material properties of epoxy-based thermoset (EPON 862/DETDAs). They discussed different approaches for building a heavily crosslinked polymer network and a multi-step technique for relaxing the developed molecular structure during crosslinking. Their predicted material properties—such as density, glass transition temperature, thermal expansion coefficient, and volume shrinkage during curing—were validated with experimental data.

Littell et al. [4] performed tension, compression, and shear tests using small specimens on epoxy resin at different strain rates. Their experimental data have been useful as standards for computational results. Komarov et al. [5] utilized a different computational method, where the polymer network was polymerized at a coarse-grained level and then mapped into a fully atomistic model. The molecular dynamics were then utilized under the OPLS force field. Their simulated T_g was found to be 20K lower than that of experimental data; this difference between the two results assumingly would be resolved once the extremely high cooling rates of molecular dynamics is taken into account.

Li and Strachan [6] predicted the atomic structure and properties of the thermosetting polymer epoxy (EPON-862) and hardener (DETDAs) using molecular dynamics with a DREIDING force field as well as a procedure to describe the chemical reactions. They proposed an efficient simulation to describe charge evolution based on the observation that atomic charges evolve significantly only during chemical reactions and in a repeatable manner. Two chemistry models were used with different relative rates for primary and secondary amine reactions to describe the hardening phenomenon in two extreme cases of processing conditions. They demonstrated that different rates of chemical reaction of interest affect properties for intermediate conversion degrees (~40-70%), but not for the higher conversion rates of interest in most applications. Their estimated density, coefficient of thermal expansion, glass transition temperature, and elastic constants of the crosslinked polymer agree with experiments.

Doherty et al. [7] utilized molecular dynamics simulations that allow a progressive crosslinking and polymerization reaction. Other simulations [8, 9] on crosslinking of epoxies for relatively small-model systems (less than 2200 atoms) have been done. Wu and Xu [10] carried out simulations on the crosslinking of epoxy resin system based on DGEBA (diglycidyl ether bisphenol A) and IPD (isophorone diamine). They used the DREIDING force field with charge equilibration and a COMPASS force field to build the structure and predict the properties, respectively. Their findings showed that COMPASS gives a more accurate description of elastic properties. Their DREIDING prediction of Young's modulus (about 50 GPa) does not agree well with the prediction from Li and Strachan [6], who employed the same force field to obtain Young's modulus in the range of 3.2-3.5 GPa.

Aluko et al. [11] constructed a molecular dynamics model employing an all-atoms OPLS force field to predict the thermo-mechanical response of the crosslinked epoxy. Their predictions were validated with both the computational and experimental data found in the literature. Lin and Khare [12] documented a one-step polymerization method for modeling the atomistic structures of crosslinked polymers. All crosslinking bonds were created in a single step when pairs of reacting atoms within a cutoff distance are identified using a simulated annealing algorithm. Bandyopadhyay et al. [13] established well-relaxed, validated molecular models of the EPON862-DETDA epoxy system that have different crosslinking densities using molecular dynamics and mechanics simulations in a united-atom force field. They used their models to predict glass transition temperature, thermal expansion coefficients, and elastic properties of each crosslinking system. They established that glass transition temperature and elastic properties increase with increased crosslink density, but the thermal expansion coefficient decreases with increased crosslink density, regardless of whether they are above or below T_g temperatures. Their data also showed reasonable correlation with those found in the literature.

For industrial grade epoxy systems [14-18], a wide range of crosslink densities (60-95%) is usually observed in experiments. Odegard et al. [19] applied the reactive force field (ReaxFF) to the molecular dynamics simulations of crosslinked epoxies; their obtained stiffness and Poisson's ratio agree closely with experiments. In spite of the significant time-scale differences between experiments and MD modeling, their results also demonstrated that the elastic/yield response from the large different strain rates can be correlated. Despite the fact that the reax force field (ReaxFF) was initially developed to model bond breaking and formation in carbon-based materials [20], Odegard et al.

[19] established from their studies that the ReaxFF can be used to predict the structure and elastic characteristics of a crosslinked epoxy material. The potential energy in the ReaxFF is defined as a function of bond order with energy penalties for nonequilibrium configurations.

Considering the fact that the yielding behavior of epoxy at elevated temperatures has not been reported in the literature, this current study focused on predicting temperature effects on the elastic and yield behavior of epoxy using a reactive force field and molecular dynamics approach. This investigation showed that the reactive force field can be used beyond bond dissociation and formation to predict elastic properties and the yielding response of crosslinked epoxy materials over a wide range of temperatures. This was established using a computational molecular dynamics simulation and the well-equilibrated models of the EPON 862-DETDA epoxy system to predict the mechanical behaviors at elevated temperatures. The simulated results were validated with the experimental data and the computational results in the literature.

Computational Method

The information on the construction of uncrosslinked epoxy resin monomers—EPON 862 (Di-glycidyl ether of Bisphenol-F) and the hardener, DETDA (Diethylene Toluene Diamine)—was first given. Then, the methodology of crosslinking and how the structure is relaxed before evaluating the mechanical behavior of the system using LAMMPS (large-scale atomic/molecular massively parallel simulator) is described.

Structure of Resin and Hardener Molecule

BioChemDraw Ultra 14.0 was used to build the EPON 862 (epoxy resin) and DETDA (hardener) monomers. The information from the output of this software package was used to define the 3D coordinates of the atoms of both monomers, their bonds, angles, and dihedrals geometries. Figure 1 shows the molecules of EPON 862 and DETDA. A stoichiometry ratio of two molecules of EPON 862 and a DETDA molecule was modeled, based on the reaction between them. After writing the molecules geometrical data obtained from ChemBioDraw into a data file in LAMMPS format, the bond, angle, and dihedral parameters were established using the OPLS all-atom force field [21-23]. This force field defines the total energy of the molecular system to be the algebraic sum of all the individual energies of the bond, angle, and dihedral, and 12-6 Lennard-Jones interactions. It should be noted that an interaction cutoff radius of 10\AA was used to model the non-bonded Van der Waals interactions.

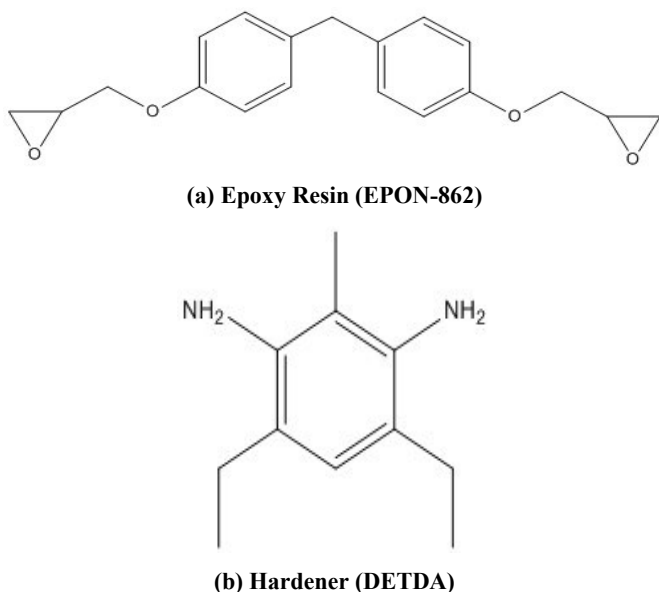


Figure 1. Molecular Structure the Resin and Hardener

The molecules of EPON 862 and DETDA were modified for easy crosslinking to obtain the pre-crosslinked configurations shown in Figure 2. The stress relaxation of these structures was carried out using MD simulations under NVT (constant volume and temperature) ensemble at 300 K. In order to further reduce the internal forces and the internal residual stresses that were generated from the initial construction of bonds, angles, and dihedrals, the material system was minimized using the conjugate gradient stopping criterion. This process was executed in LAMMPS for 400 ps at a temperature of 300 K.

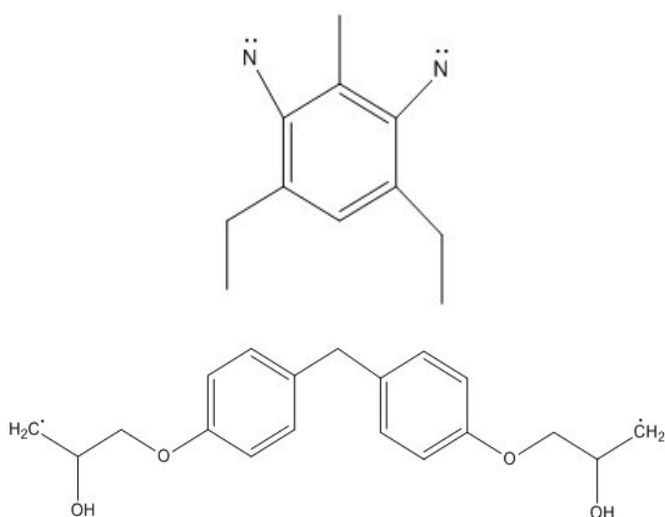


Figure 2. Molecular Structure of Pre-crosslinked Epoxy Resin (EPON 862) and Hardener (DETDA) Monomers

A system of stoichiometric mixture of 128 EPON 862 molecules and 64 DETDA molecules consisting of 7488 atoms was replicated in a periodic box after the initial 2:1 equilibrated structure. These initial MD were performed using an OPLS all-atoms force field in LAMMPS software, provided by Sandia National Laboratories. Then, the replicated system was relaxed using NVT ensemble for 400 ps at atmospheric pressure and a temperature of 300 K. The Noose-Hoover thermostat and barostat were used for temperature and pressure control, respectively. Furthermore, the system was minimized before compressing the simulation box in stages under NVT ensemble and in quasi-equilibrium condition until a density of 1.2 g/cm^3 was achieved. It is important to note that, at the end of each stage of box reduction, one or two minimizations were performed on the EPON 862-DETDA system to allow molecular relaxation of the atoms' coordinates in the new volume space of the simulation box. At the end of box reduction, when the system density was 1.2 g/cm^3 , the system was further subjected to the molecular minimization and equilibration before crosslinking the material system.

Modeling and Crosslinking of Polymers

As mentioned by Odegard et al. [19], in order to efficiently establish the crosslinked structure, it is essential to first create the model with a traditional fixed-bonding force field (OPLS). The fix bond/create command can be used in OPLS to create the crosslink bonds between atoms and reactive groups for specified distances. However, the ReaxFF does not allow this command to be used. It is important to note that the modified molecules of EPON 862 and DETDA, shown in Figure 2, circumvent the initial hydration and activation process of crosslinking [3, 11]. The dots on the top of the nitrogen and carbon atoms show the reactivity of active amine groups in the DETDA and methylene groups in EPON 862, respectively, toward crosslinking.

The crosslinking assumes equal reactivity of primary and secondary amine and is also based on the active sites. Crosslinking was performed using the NVT ensemble at a temperature of 300 K and one atmosphere. Since it is important to ascertain that the simulation time in between successive reactions is sufficiently long for the unreacted species to move around, the system was relaxed for 2 ps at each successive crosslinking. It should be noted that all the new additional covalent terms (bonds, angles and dihedrals) were added to the connectivity definition, after the new bonds were formed. Based on the fact that chemical reactions were not modeled in the simulations, a crosslinking distance between active sites was defined in order to prevent structural configurations that have high residual stresses after bond formation, which may be difficult to relax during energy

minimization and molecular dynamic simulation. Hence, a cut-off distance of 4.6Å was chosen for crosslinking, based on prior work [3], to achieve a crosslinking limit. The crosslink density is the ratio of the number of crosslinks formed compared to the number of crosslinks that could be formed. Knowing that, for industrial-grade epoxies, a broad range of crosslink densities (60-95%) is typically observed in experiments [14-18], the simulated crosslink density was chosen to span part of this range. It is important to mention that energy minimization and stress relaxations were executed at regular time intervals under NVT ensemble during this process of crosslinking. Figure 3 shows the crosslinked and equilibration structure of the EPON 862 and DETDA system. Three different samples of relaxed and crosslinked EPON 862/DETDA molecular dynamics models were built with OPLS.

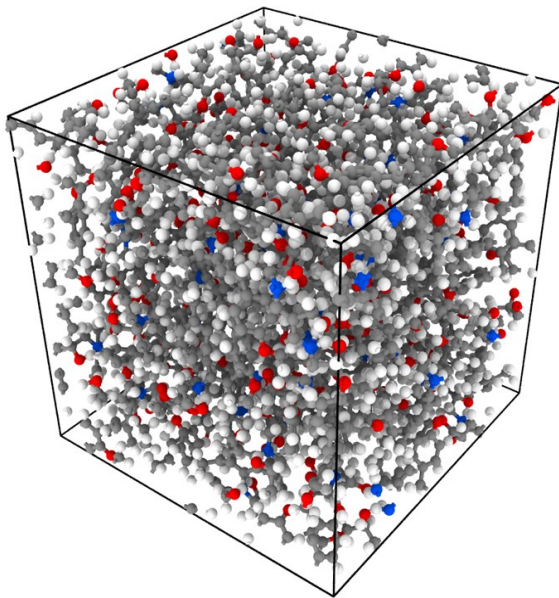


Figure 3. Molecular Structure of Crosslinked and Relaxed Epoxy System

After the initial process of crosslinking and relaxation, the process was brought to completion under the OPLS force field, and the relevant information regarding the molecular configuration of the established structures (the atom's masses, coordinates, types, ID, and charge balance), which satisfies the requirements for ReaxFF, were written into a new data file. Then, the system with the parameterizations by Liu et al. [24] was equilibrated in NVT [25], using the ReaxFF in LAMMPS. The temperature was gradually increased from 0.0 to 300 K during these simulations for a period of 100 ps, using a time step of 0.1 fs, to ensure that the residual stress was taken out of the model. The final

equilibration of the system was done under NPT ensemble at 300 K for 100 ps, using a time step of 0.1 fs and Nose-Hoover barostat and thermostat in order to obtain a fully relaxed structure. On completion of these processes, uniaxial tension tests were performed on the samples at room and elevated temperatures, in order to characterize the mechanical performances (Young's modulus, Poisson's ratio, and yield strength) of the material system.

Results and Discussion

The mechanical characteristics of the crosslinked and relaxed EPON 862-DETDA system were evaluated at room and elevated temperatures. In general, to obtain the stress-strain relationship that can be used to evaluate the desired mechanical properties, it is important to note that different types of geometric deformations are usually carried out on the equilibrated structures. The sample was independently deformed under tensile loadings in the x and y directions, using a strain rate of 2×10^{-8} /s under NPH ensemble with barostat and thermostat control. The NPH ensemble accommodates Poisson's effect in the two lateral directions. This process of deformation was performed incrementally until a maximum of 20% axial strain was attained under a pressure of one atmosphere and a temperature of 300 K. The deformations were applied gradually for a period of 1000 ps, using a time step of 0.1 fs and the Poisson's ratio was obtained from the negative slope of the lateral/longitudinal strain curve up to the yield point. The predicted average Poisson's ratio from this investigation at a temperature of 300 K was 0.3478. Similarly, Table 1 documents the Poisson's ratio of the model for 400 and 500 K.

Table 1. Average Values for Poisson's Ratio for Crosslinked Structures at Different Temperatures

Property	ν Poisson's ratio @300 K	ν Poisson's ratio @ 400 K	ν Poisson's ratio @ 500 K
Present 85 % Crosslinking	0.3478	0.5394	0.5933
Li et al. [6]	0.43-0.47	-	-
Wu and Xu [10]	0.3507	-	-

Figure 4 shows the stress-strain curve of the EPON 862/DETDA system, both at room and elevated temperatures; the yield strength was calculated from this figure. The yield strength is the point where the straight line drawn from 0.2% strain ($\epsilon=0.002$) parallel to the elastic portion of the stress-strain curve intercepts the curve [25]. Figure 2 shows the estimated average value of the yield stress at the specified temperatures. Figures 5 and 6 shows the simulated val-

ues in comparison with experimental data from the literature [4] at room and 400 K, respectively. Also shown in these figures is the power-law least-squares fit of the experimental data [4]. As depicted from these figures, there is an agreement between predicted and experimental values when the effect of temperature is considered. It is important to note that the superposed lines show the trend of the experimental values. The power law in Figure 5 is given in Equation (1) and that of Figure 6 is given in Equation (2):

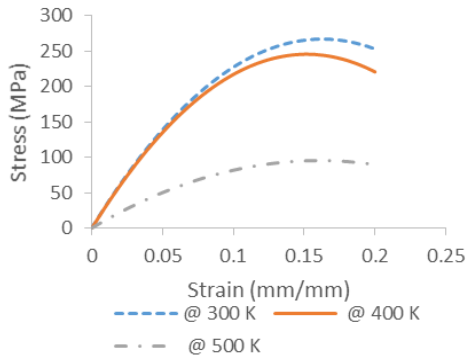


Figure 4. Stress/Strain Curve for EPON 862/DETDA at Specified Temperatures

$$\sigma_y = 83.92 \dot{\epsilon}^{0.0285} \quad (1)$$

$$\sigma_y = 60.805 \dot{\epsilon}^{0.0436} \quad (2)$$

where, σ_y = yield strength.

Table 2. Average Values for Yield Strength for Crosslinked Structures at Different Temperatures

Property (MPa)	σ_y Yield strength @300 K	σ_y Yield strength @ 400 K	σ_y Yield strength @ 500 K
Structure at 85 % crosslinking	127.000	120.963	75.570

Young's modulus was determined from the slope of the straight portion of the stress-strain curve in Figure 4, up to the yield point for the different temperatures evaluated. Figure 7 shows this simulated value, as compared with experimental data [4] at room temperature. Figure 7 also shows a power-law least-squares fit of the experimental data. The superposed lines show the trend of the experimental values; this line is given in Equation (3):

$$E = 3.0167 \dot{\epsilon}^{0.0149} \quad (3)$$

where, E is Young's modulus and $\dot{\epsilon}$ is strain rate.

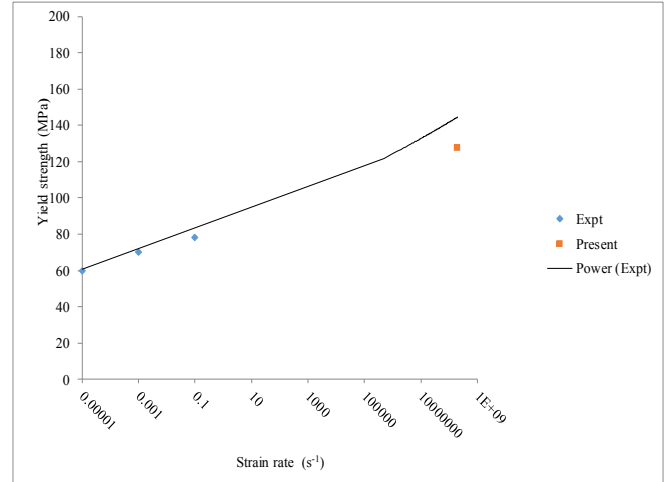


Figure 5. Predicted and Measured Yield Strength versus Strain Rate at a Temperature of 300 K

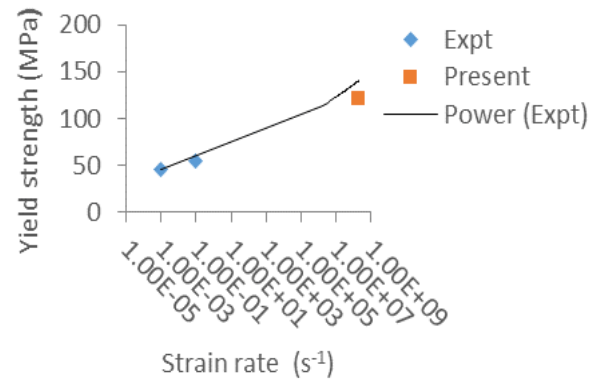


Figure 6. Predicted and Measured Yield Strength versus Strain Rate at a Temperature of 400 K

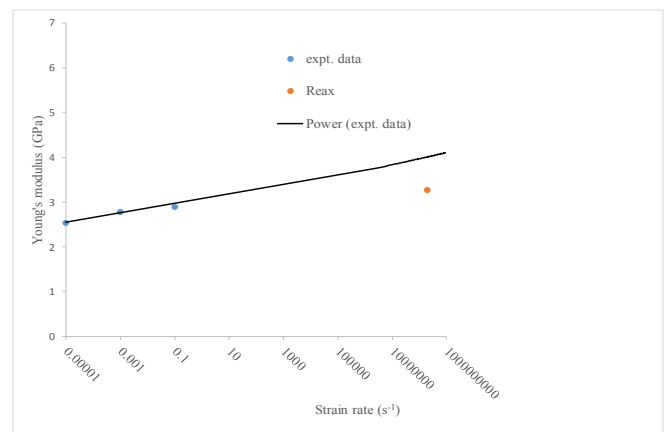


Figure 7. Predicted and Measured Young's Modulus versus Strain Rate at 300 K

Table 3 gives the average values for Young's moduli of the models at specified temperatures.

Table 3. Average Values for Modulus of Elasticity for Crosslinked Structures at Different Temperatures

Property (GPa)	E Young's modulus @ 300 K	E Young's modulus @ 400 K	E Young's modulus @ 500 K
Structure at 85% crosslinking	3.255	3.220	1.175
Li et al. [1]	3.2-3.5	-	-
Wu and Xu [10]	5.198	-	-

Conclusion

The computational molecular dynamics of an epoxy system was performed using the reactive force field with the parametrization of Liu et al. [24] to predict its mechanical properties at elevated temperatures. It was established from the results of the computational analysis that ReaxFF with Liu et al.'s parameter can be employed to predict the mechanical behavior of an epoxy system both at room and elevated temperatures. Furthermore, the predicted results consisting of the elastic properties, such as Young's modulus, Poisson's ratio, and the plastics behavior such as yield strength agree well with the available experimental data and simulated results.

Acknowledgements

One author would like to thank the Office of Research at the University of Michigan-Flint for providing financial support to him, and the Michigan Technological University for making the SUPERIOR, its high-performance computer cluster, available for this research work.

References

- [1] Abbot, L. J., Hart, K. E., & Colina, C. M. (2013). Polymatic: A Generalized Simulated Polymerization Algorithm for Amorphous Polymers. *Theor Chem ACC*, 132(1334), doi10.1007/s00214-013-13334-z.
- [2] Yarovsky, I., & Evans, E. (2002). Computer Simulation of Structure and Properties of Crosslinked Polymers: Application to Epoxy Resins. *Polymer*, 43(3), 963-969.
- [3] Varshney, V., Patnaik S. S., Roy, A. K., & Farmer, B. L. (2008). A molecular Dynamics Study of Epoxy-Based Networks: Cross-linking Procedure and Prediction of Molecular and Material Properties. *Macromolecules*, 41, 6837-6842.
- [4] Littell, J. D., Ruggeri, C. R., Goldberg, R. K., Roberts, G. D., Arnold, W.A., & Binienda, W. K. (2008). Measurement of Epoxy Resin Tension, Compression, and Shear Stress-Strain Curves Over a Wide Range of Strain Rates Using Small Test Specimens. *Journal of Aerospace Engineering*, 21, 162-173.
- [5] Komarov, P. V., Chiu, Y. T., Chen, S. M., Khalatur, P. G., & Reineker, P. (2007). Highly Cross-linked Epoxy Resin: Atomistic Molecular Dynamics Simulation Combined with a Mapping/Reverse Mapping Procedure. *Macromolecules*, 40, 8104-13.
- [6] Li, C., & Strachan, A. (2010). Molecular Dynamics Prediction of Thermal and Mechanical Properties of Thermoset Polymer EPON862/DETDA. *Polymer*, 51, 6058-6070.
- [7] Doherty, D. C., Holmes, B. N., Leung, P., & Ross, R. B. (1998). Polymerization Molecular Dynamics Simulations. I. Cross-linked Atomistic Models for (methacrylate) Networks. *Computational and Theoretical Polymer Science*, 891(2), 169-78.
- [8] Fan, H. B., & Yuen, M. M. F. (2007). Material Properties of the Cross-linked Epoxy Resin Compound Predicted by Molecular Dynamics. *Polymer*, 48(7), 2174-2178.
- [9] Fan, H. B., Chan, E. K. L., Wong, C. K.Y., & Yuen, M. M. F. (2007). *Journal of Electronic packaging*, 129(1), 35-40.
- [10] Wu, C. F., & Xu, W. J. (2006). Atomistic Molecular Modelling of Cross-linked Epoxy Resin. *Polymer*, 47, 6004-6009.
- [11] Aluko, O., Gotham, S., Chinkanjanarot, S., Radue, M., & Odegard, G. M. (2015). A Computational Molecular Dynamic study on Epoxy-based network: Thermo-mechanical properties, *Proceedings of the ASC, Conference, Paper # 1906*. Virginia VA.
- [12] Lin, P. H., & Khare, R. (2009). Molecular Simulation of Cross-linked Epoxy-POSS Nanocomposites. *Macromolecules*, 42, 4319-27.
- [13] Bandyopadhyay, A., Valavala, P. K., Clancy, T. C., Wise, K. E., & Odegard, G. M. (2011). Molecular Modeling of Cross-linked Epoxy Polymers: The Effect of Crosslink Density on Thermomechanical Properties. *Polymer*, 52, 2445-242.
- [14] Varley, R. J., Heath, G. R., Hawthorne, D. G., Hodgkin, J. H., & Simon, G. P. (1995) Toughening of a trifunctional Epoxy system. I. Near-infrared spectroscopy study of homopolymer cure. *Polymer*, 36(7), 1347-1355.
- [15] Wang, Q., Storm, B. K., & Houmoller, L. P. (2003). Study of the isothermal curing of an epoxy prepreg by near-infrared spectroscopy. *Journal of Applied Polymer Science*, 87(14), 2295-2305.

-
- [16] Musto, P., Martuscelli, E., Ragosta, G., & Russo, P. (2000). The curing process and moisture transport in a tetrafunctional epoxy resin as investigated by FT-NIR spectroscopy. *High Perform Polymer*, 12(1), 155-168.
- [17] Dannenberg, H. (1963). Determination of functional groups in epoxy resins by near-infrared spectroscopy. *SPE Transactions*, 3(1), 78-88.
- [18] George, G. A., Coleclarke, P., Stjohn, N., & Friend, G. (1991). Real-time monitoring of the cure reaction of a Tgddm/Dds epoxy-resin using fiber optic Ft-Ir. *Journal of Applied Polymer Science*, 42(3), 643-657.
- [19] Odegard, G. M., Jensen, B. D., Gowtham, S., Wu, J., He, J., & Zhang, Z. (2014). Predicting Mechanical Response of Cross-linked Epoxy using ReaxFF. *Chemical Physics Letters*, 391, 175-178.
- [20] Van Duin, A. C. T., Dasgupta, S., Lorant, F., Goddard W. A. (2001). *Journal of Physics: Chem A*, 105(41), 9396.
- [21] Jorgensen, W. L., Maxwell, D. S., & Tirado Rives, J. (1996). Development and Testing of OPLS All Atoms Force Field on Conformational Energetics and Properties of Organic Liquid. *Journal of American Chemical Society*, 118(45), 11225-11236.
- [22] Weiner, S. J., Kollman, P. A., Case, D. A., Singh, U. C., Ghio, C., Alagona, G., et al. (1984). *Journal of the American Chemical Society*, 106(3), 765-84.
- [23] Watkins, E. K., & Jorgensen, W. L. (2001). Perfluoroalkanes: Conformational Analysis of Liquid-State Properties from ab Initio and Monte Carlo Calculations. *Journal of Physical Chemistry A*, 105(16), 4118-4125.
- [24] Liu, L. C., Liu, Y., Zybin, S. V., Sun, H., & Goddard, W. A. (2011). ReaxFF-g: Correction of the ReaxFF Reactive Force Field for London dispersion, with Applications to the Equations of State for Energetic Materials. *Journal of Physical Chemistry A*, 115(40), 11016-11022.
- [25] Aluko, O., Gowtham, S., & Odegard, G. M. (2015). A Molecular Dynamic Modeling of Cross-linked Epoxy Resin Using Reactive Force Field: Thermo-mechanical properties. *Journal of Mechanics Engineering & Automation*, 5(12), 655-666.

SHANKARA GOWTHAM is an adjunct assistant professor of Physics and Electrical Engineering and also a director of Research Computing at Michigan Technological University. He earned his PhD in Physics from Michigan Technological University in 2007. His interests include parallel computing and visualization, and interaction of biological matter with nanomaterials. Dr. Gowtham may be reached at g@mtu.edu

GREGORY M. ODEGARD is a professor of Mechanical Engineering at Michigan Technological University. He earned his PhD in Mechanical Engineering from the University of Denver in 2000. His interests include computational mechanics and computational materials science. Dr. Odegard may be reached at gmodegar@mtu.edu

Biographies

OLANREWAJU ALUKO is an associate professor of Mechanical Engineering at the University of Michigan-Flint. He earned his PhD in Mechanical Engineering from Howard University in 2007. His interests include polymeric composite, nanocomposite, mechanics of materials and structures. Dr. Aluko may be reached at aluko@umflint.edu

IMPROVING FIWI ACCESS NETWORK DOWNSTREAM PERFORMANCE: A DISTRIBUTED APPROACH

ASM Delowar Hossain, City University of New York; Muhammad Ummay, City University of New York; Abdullah Hossain, City University of New York

Abstract

In a FiWi access network, the central office (CO) is responsible for downstream transmission and scheduling. In a typical centralized FiWi network, the CO is responsible for upstream bandwidth allocation tasks as well. Such upstream control tasks consume the CO's resources, negatively impacting the downstream performance. Therefore, from this study, the authors propose a distributed upstream control scheme by shifting the centralized task from the CO to the wireless nodes closely clustered at the access end. This scheme relieves the CO from the upstream tasks, paving the way for improved downstream performance.

Introduction

To address the issue of unlimited growth in mobile traffic, the radio access network (RAN) tends to utilize the passive optical network (PON) access infrastructure as a packet-based converged, fixed-mobile optical access networking transport architecture to backhaul both wireless and wireline traffic [1-3]. This hybrid access architecture is known as fiber-wireless (FiWi) [4] or wireless-optical broadband access network (WOBAN) [5]. It merges the unlimited bandwidth of fiber optics with the mobility offered by wireless technologies. It is an amalgamation of an optical backend and a wireless front-end for an optimum access network. A PON connects a number of optical network units (ONUs) located at the customer premises to an optical line terminal (OLT) located at the central office (CO-service provider's facility) via an optical splitter and distribution fiber [6]. The typical distance between the ONU and CO can be 20 km, but varies due to other requirements and the number of ONUs to be supported. It is typically a point-to-multipoint architecture in which passive optical splitters are utilized to allow a single optical fiber to serve multiple end-point ONUs/customers (closely dispersed ~1km radius), without having to provide point-to-point fibers between the OLT and ONUs. There are few different PON options available, namely time division-multiplexed (TDM-PON), orthogonal frequency division multiplexed PON (OFDM-PON), and time wavelength-division-multiplexed PON (TWDM-PON) [7]. Despite the expansion of WDM-PON research to enhance network throughput, research in TDM-PON is still essential for supporting per wavelength improvements [8].

In a FiWi access network, the wireless base station (BS) is connected to an ONU that is capable of communicating with wireless subscribers as well as among the BSs. Figure 1 shows how typical wireless traffic from a BS that is destined to go out of the access network is transported by the optical network via a correspondingly connected ONU. Furthermore, to support a FiWi network with an increased number of small cells, extensive fiber installation is necessary. Therefore, TDM-PON is a cost-effective candidate [9] for such an undertaking. Consequently, the authors of this current study prefer a TDM-PON-based FiWi access network. Recent FiWi access networks are primarily based on a centralized PON scheme in which a distant OLT is responsible for both upstream and downstream network resource allocation. The OLT's centralized task of upstream resource allocation hinders downstream performance of the PON/FiWi access network [10]. Therefore, from this current study, the authors propose to take advantage of the wireless plane of FiWi to support a distributed resource allocation scheme for PON. It simply transfers the centralized upstream control task from the distant central office (OLT) to the wireless nodes closely clustered at the access end. As a result, the typical downstream overhead needed for upstream tasks is eliminated, which paves the way for improved downstream performance.

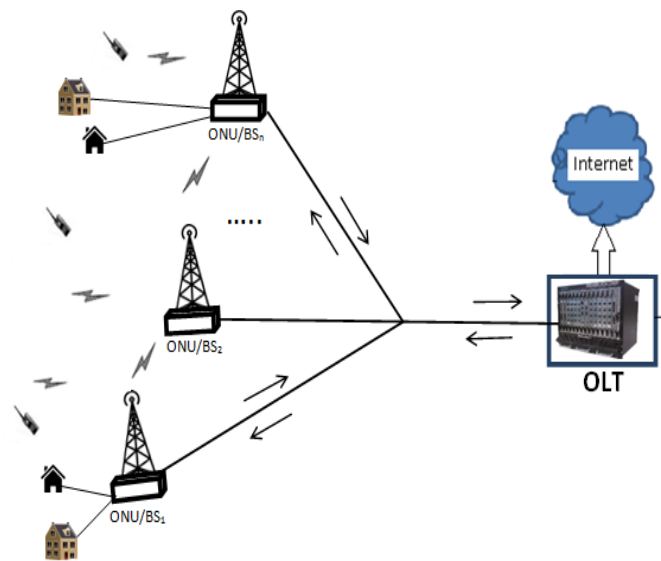


Figure 1. FiWi Network

PON

It is important to introduce the functional aspect of TDM-PON, because it is the transport medium for all traffic, optical and wireless. TDM-PON utilizes two wavelengths for transmission, one for downstream traffic (OLT to ONUs) and the other for upstream traffic (ONUs to OLT). For downstream traffic, the passive power splitter connects the OLT and ONUs through the distribution fiber. OLT houses N queues, each corresponding to an ONU. Incoming traffic is first sorted according to destination ONU addresses and then accepted into the corresponding queues. Periodically, the OLT checks the downstream queue occupancy and divides available downstream bandwidth among the queues and allocates transmission timeslots. The OLT then broadcasts frames from a queue (corresponding to a destination ONU/BS) in its allocated timeslot. An ONU/BS accepts the broadcasted frame matching its medium access control (MAC) address to frame destination address.

In a typical centralized architecture, the OLT is required to perform an additional function of arbitrating among the ONUs for sharing upstream bandwidth. To facilitate the implementation of upstream bandwidth allocation schemes, the OLT and ONUs exchange control messages—namely, REPORT and GATE messages. These control messages are defined by the IEEE 802.3ah taskforce through the development of multi-point control protocol (MPCP) [11]. A REPORT message is sent by an ONU to the OLT, informing it of its bandwidth requirements. Upon receiving a REPORT, the OLT passes the message to its DBA module to perform the bandwidth allocation computation. The OLT then grants the ONU a transmission timeslot by sending a GATE message indicating the start time and the duration of such a timeslot. The OLT’s cyclic task of GATE/REPORT messages and DBA calculation consumes downstream resources, thereby degrading downstream performance.

The total downstream overhead required for cyclic upstream GRANT depends upon the upstream cycle length and number of ONUs in the network. The upstream cycle length is variable between a certain minimum and maximum bound to accommodate variable traffic load. At a higher upstream load, the cycle time will be up to the maximum length. The maximum upstream cycle length is typically set to 2ms [10-12]. At a lower upstream load, cycle lengths are shorter. Note that the minimum cycle length cannot be shorter than the round trip time (RTT) between an ONU and OLT [10-12], because cycle length is the time between two consecutive GRANTs to a specific ONU, which is equivalent to at least one RTT (between the OLT and the ONU). The RTT between the OLT and the ONU depends on the distance between them (i.e., for ~20 km

trunk, the RTT is ~200 μ s; similarly for 10 km the RTT is ~100 μ s). Minimum upstream cycle length is defined by Equation (1):

$$T_{upstream_cycle_min} = MAX \begin{cases} T_{rtt} \\ N (T_{guard} + (R/R_{PON})) \end{cases} \quad (1)$$

where, R_{PON} is the ONU-to-OLT transmission line rate; R is the ONU report size; N is the number of ONUs; T_{guard} is the guard time between two ONU upstream transmissions; and, T_{rtt} is the round trip time between ONU and OLT.

While the upstream cycle length gets shorter, the number of upstream cycles per second increases significantly. Thus, at a low network load, the total number of grants/second issued by the OLT increases. The number of upstream grants per cycle is equal to the number of ONUs in the system. Therefore, upstream overhead increases along with the number of ONUs. The worst case downstream overhead wastage due to upstream tasks can be estimated using Equation (2):

$$B_{downstream_waste}^{GATE} = \frac{1}{T_{upstream_cycle_min}} (N * G) \quad (2)$$

where, G is GRANT size in bits; $T_{upstream_cycle_min}$ is the minimum duration of the upstream cycle; and, N is the number of ONUs.

To illustrate this point, a network of 32 ONUs (1Gbps line rate with 10 km trunk length) can require an overhead of up to 20% of the total network capacity (when the upstream network load is < 10%).

FiWi

A typical FiWi network consist of mainly two parts: optical backhaul and wireless front end. FiWi can be categorized into different types, depending on the interconnection between the optical and wireless part, such as independent or combined/hybrid architectures for the integration of PONs and wireless counterpart [13]. This study looked at TDM-PON-based FiWi, where the ONU can be either interconnected to or integrated into a BS (see Figure 1). In the downstream direction, the packet (either for ONU or BS) is transmitted via trunk fiber and the optical splitter splits the OLT signal equally among the ONUs. If the packet is destined to an ONU/BS, it accepts it as per MAC address and then forwards it to subscribers (wired or wireless network). Note that the OLT has an additional task of upstream re-

source allocation, as described previously. In the upstream direction, when wireless end users want to send packets, it contacts the closest BS and then traffic from the BS passes through the connected ONU to the OLT (via splitter and fiber network) as per transmission time window assigned by the OLT. This centralized scheme burdens the OLT with additional upstream tasks, resulting in sub-optimal downstream performance as detailed in the PON section. To alleviate this impediment, the authors took advantage of a wireless plane to propose a distributed control scheme, where the OLT is relieved from upstream tasks.

Proposed Distributed Control Scheme

The direct intercommunication among the access nodes facilitates signaling, queue reporting, grant scheduling, and handoff procedures that operate in a distributed manner. Therefore, the data plane is supported by the PON, while the control plane/reporting is supported by the wireless plane. It results in a fully distributed time division multiple access (TDMA) arbitration scheme in which the distant OLT is exempt from the arbitration process. In the proposed distributed scheme, the nodes exchange signaling and control information concerning their queue statuses (REPORT messages) and their transmission needs amongst themselves via a wireless plane. Then the nodes concurrently and independently run instances of the common DBA algorithm, resulting in identical bandwidth allocation outcomes. Once the algorithm has been run, the nodes transmit their traffic (wireless and wired) sequentially and in an orderly manner via PON, while eliminating the OLT's centralized task of upstream DBA. This scheme primarily relates to the upstream direction; however, as an additional advantage, it enhances the downstream performance. The detailed mechanism of this distributed scheme is discussed next.

BSs can directly communicate the status of their queues and radio resources and exchange signaling and control messages with one another. Upon discovery of the neighboring BSs, each BS sends overall ONU/BS queue information to its neighbors. Each access node maintains a database about the states of its own queue and every other queue on the network. This information is updated each cycle, whenever the node receives new REPORT messages from all other nodes. The REPORT message typically contains the desired size of the next timeslot, based on the current ONU and BS buffer occupancy. The wireless reporting starts at the end node of one side and travels forward towards the other end (forward transmission). Once the first (edge) node sends the report to next forward node, the second node appends its report to the first one and transmits to the next forward node (see Figure 2). This process continues sequentially. Once all of the appended messages (complete

network information—CNI) from all of the nodes are at the last node, they are shared with all the other nodes in that network by reversing the direction of sequential transmission (without appending any more information). That implies that the last node (Node_n) sends the CNI back (backward transmission) to the previous node (Node_{n-1}), then that node (Node_{n-1}) sends it to the node prior to it in sequence (Node_{n-2}); this process continues until all of the nodes receive the CNI (containing all BS/ONU queue reports of the entire network). Upon reception of the CNI, an identical dynamic bandwidth allocation (DBA) module, which resides at each access node, uses the REPORT messages during each cycle to calculate a new upstream timeslot assignment for each node (ONU/BS).

The execution of the DBA algorithm at each node starts once all of the nodes receive the CNI. Once the algorithm is executed, the nodes sequentially and orderly transmit their data without any collisions, eliminating the OLT's centralized task of processing requests and generating grants for bandwidth allocations. Similar to any typical TDM scheme, it requires a guard time between two successive transmissions of nodes. Thus, supported by the distributed control plane, most of the typical radio control functions, including radio resource management, handover control, admission control, etc., can be independently implemented at each node in a distributed manner without resorting to a distant centralized entity (OLT). Therefore, unlike the typical centralized scheme, the entire downstream resource is available to the downstream network and offers simplicity in the downstream DBA process.

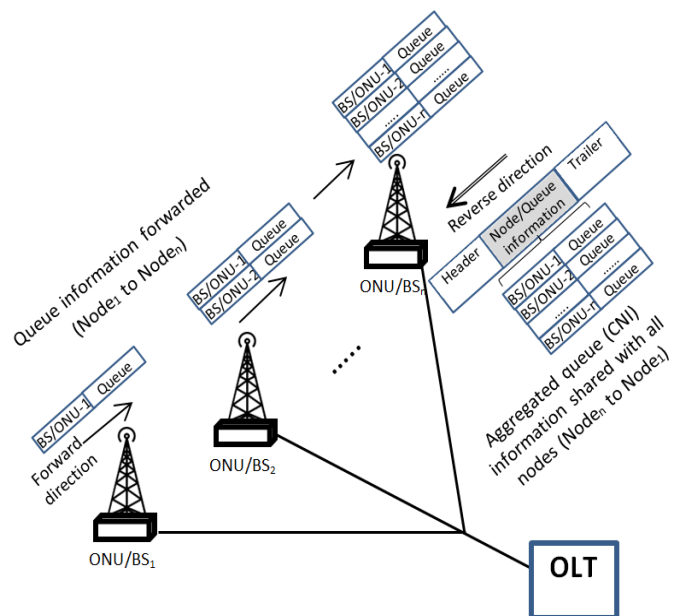


Figure 2. FiWi Network's Distributed Reporting Mechanism

As wireless bandwidth is costly, it is important to point out that the distributed scheme requires a minimal bandwidth from the wireless plane. First, the aggregated frame is not aggregated in terms of frame count (i.e., $n \times$ frames); rather, it is a single frame, where node IDs and queue sizes are appended into the payload (see Figure 2). This results in an overhead of a single frame with additional payload. To illustrate the impact of this scheme on wireless bandwidth, Table 1 shows an arbitrary scenario.

Table 1. Wireless Network Configuration

Number of BS	16
BS transmission rate (64QAM, 4x4 MIMO, 20 MHz) [14]	326 Mbps
Cycle time	2ms
Transmit report per cycle	2
Report frame overhead	12 bytes (96 bits)
Report size	10 bytes (80 bits)
Aggregated report size	$(16 \times 80) + 96 = 1376$ bits

As per the scenario noted above, the proposed scheme requires $(1/0.002 \times 1376 \times 2) \approx 1.4$ Mbps bandwidth per BS. Therefore, the required bandwidth per node is less than 0.5% of the BS transmission capacity. It is important to note that, as the MIMO and the modulation techniques advance, the impact of the proposed scheme on the wireless bandwidth is negligible.

Now the ease of downstream bandwidth allocation scheme is demonstrated within the proposed distributed paradigm. In every cycle, the available downstream bandwidth is divided among the queues using Equation (3):

$$B_i^{Granted} = \begin{cases} Q_i & \text{if } Q_i \leq B_{max} \\ B_{max} & \text{if } Q_i > B_{max} \end{cases} \quad (3)$$

where, $B_{max} = \frac{1}{N} [R_{PON} * T_{downstream_cycle_max}]$

and where, R_{PON} is the OLT-to-ONU (downstream) transmission line rate; N is the number of downstream queues in the OLT; $T_{downstream_cycle_max}$ is the maximum cycle time; and, Q_i is the OLT queue that corresponds to ONU/BS_{*i*}.

In other words, a queue is granted the requested number of bytes, but no more than a given predetermined B_{max} . A queue request exceeding the maximum limit (B_{max}) will be granted additional bandwidth in the next cycle. It is called the fixed maximum limit (FML) algorithm.

Simulation and Results

In this section, the simulation performance of the proposed distributed downstream scheme is compared with that of the centralized downstream scheme. An event-driven packet-based simulation model was developed using C++. Two simulation programs with identical network parameters were developed: one for the typical centralized scheme and another for the proposed distributed scheme. A simple FML algorithm for both centralized and proposed distributed schemes was employed to demonstrate the advantage of the proposed scheme. The performance metrics used here are average queuing delay, average maximum queuing delay, packet loss ratio, and average queue size. To compare the performance results of the proposed distributed scheme with that of the centralized scheme, the following system parameters were used: an OLT housing 16 queues corresponding to 16 ONUs/BS; a downstream link rate of 1Gb/s; an incoming data rate to the OLT queues of 100Mbps; individual queue sizes of 10 MB; a trunk length of ~ 10 km; and, a maximum downstream cycle time, T_{MAX} , of 2ms. Parameters specifically associated with the centralized scheme included an upstream link rate of 1Gbps; an inter-ONU upstream transmission guard time, T_G , of 1 μ s; and, a downstream GRANT message size of 84 bytes.

The traffic model used in this simulation was the same as that reported by Luo et al. [12]. All arriving downstream frames to the OLT are queued in a first-in-first-out buffer. Packets are generated with arrival times and sizes. As per arrival time, a packet is accepted in a queue. Once the packet is scheduled to be transmitted out, the queue is freed up from that packet. The queuing delay is the time between the packet's arrival to and departure from a queue. Each point on the following plots corresponds to a sample of 50 million packets averaged over three different runs. Plots are presented in reference to downstream total network load (TNL), which is defined as the average accumulative load of all queues at the OLT.

Figures 3 and 4 show the average and maximum downstream packet queuing delays for centralized and distributed schemes. The centralized delay is always longer than the distributed one (initially in microseconds and later in milliseconds). At low downstream TNL, the effective downstream bandwidth in the centralized scheme is about 20% less than the distributed scheme. Note that it is still adequate for serving the queues at low load. However, the OLT's additional GATE function in the centralized scheme causes the downstream cycle to be longer than that of the distributed scheme. The consequence is a comparatively longer buffer stay, resulting in a longer queuing delay in the centralized network, in spite of adequate bandwidth. On the other hand,

at higher TNL, the centralized scheme suffers from a lack of available bandwidth; therefore, it cannot serve as much traffic as in a distributed scheme. Packets have to wait in the queue for the next cycle, causing more queuing delay. This longer queue occupancy results in a comparatively larger queue size for the centralized scheme than that of distributed scheme (see Figure 5). At higher load, the queue sizes get larger, and at TNL~1 (100%), queues are saturated causing packet drops. Figure 6 depicts this very fact; since the centralized scheme has a comparatively larger queue size, it causes more packet drops than the distributed scheme.

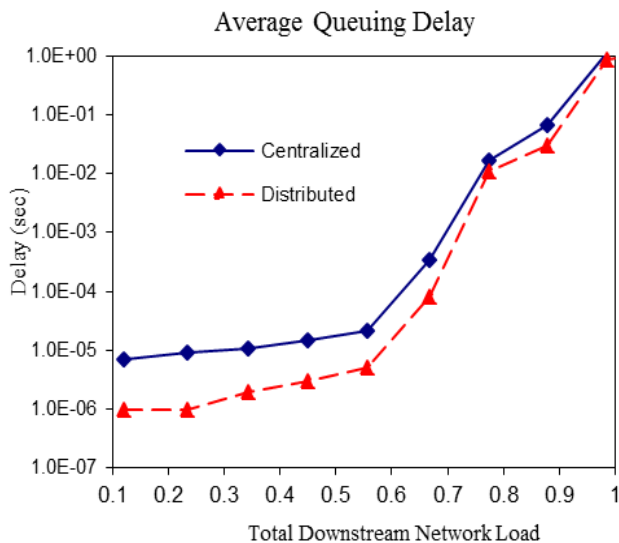


Figure 3. Average Queuing Delay for Both Schemes

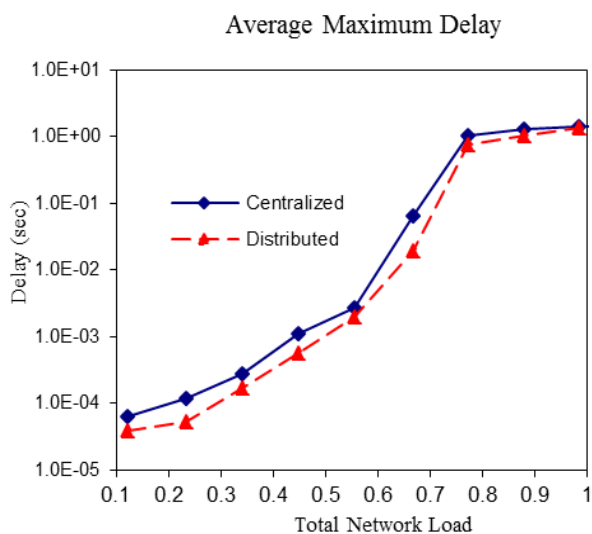


Figure 4. Average Maximum Queuing Delay for Both Schemes

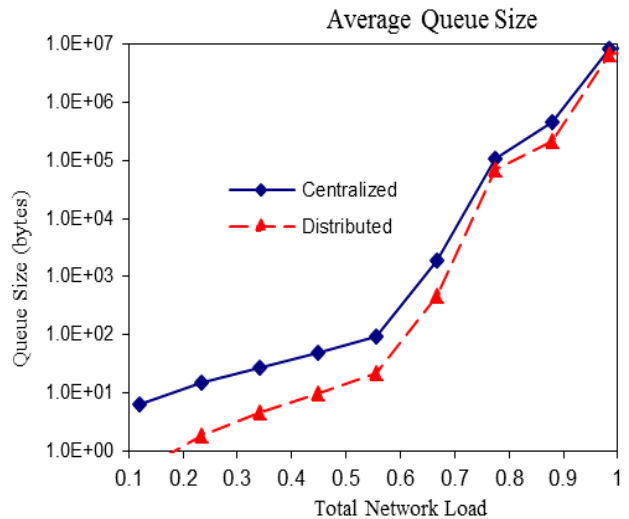


Figure 5. Average Queue Size for Both Schemes

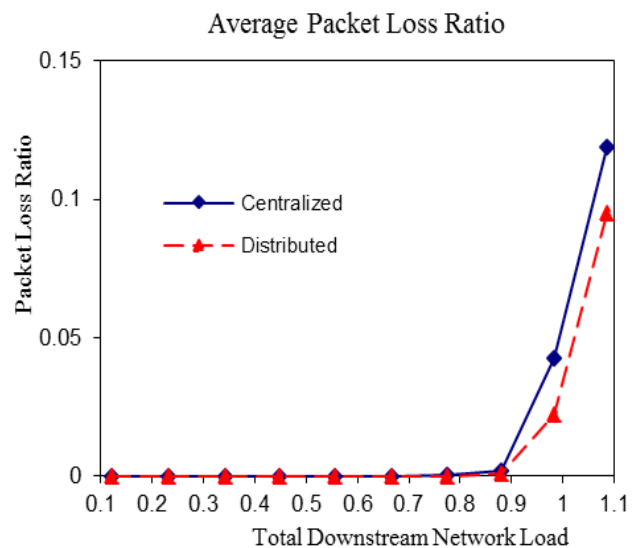


Figure 6. Average Packet Loss Ratio for Both Schemes

Conclusion

This work takes advantage of the wireless plane connectivity in FiWi access networks to exchange node queue information to support a fully distributed control plane, where the OLT is relieved from upstream resource allocation tasks. This lends the OLT more resources for downstream networks and consequently results in better network performance.

References

- [1] Zhang, J., Collings, I., Chen, C., Rouillet, L., Luo, L., Ho, S., et al. (2013). Evolving Small-Cell Communications towards Mobile-over-FTTx Networks. *IEEE Communications Magazine*, 51(12), 92-101.
- [2] Shaddad, R., Mohammad, A., Al-Gailani, A., Al-hetar, A., & Elmagzoub, M. (2014). Survey on access technologies for broadband optical and wireless networks. *Journal of Network and Computer Applications*, 41, 459–472.
- [3] Mali, N., & Jog, V. (2105). QoS Control in FiWi Access Network. *International Journal of Emerging Engineering Research and Technology*, 3(7), 53-60.
- [4] Ghazisaidi, N., Maier, M., & Assi, C. (2009). Fiber-Wireless (FiWi) Access Networks: A Survey. *IEEE Communication Magazine*, 47(2), 160-167.
- [5] Sarkar, S., Dixit, S., & Mukherjee, B. (2007). Hybrid Wireless-Optical Broadband-Access Network (WOBAN): A Review of Relevant Challenges. *Journal of Lightwave Technology*, 25(11), 3329-3340.
- [6] Kramer, G., & Pesavento, G. (2002). Ethernet Passive Optical Network (EPON): Building a Next Generation Optical Access Network. *IEEE Communication Magazine*, 40(2), 66–73.
- [7] Luo, Y., Zhou, X., Effenberger, F., Yan, X., Peng, G., Qian, Y., et al. (2013). Time and wavelength-division multiplexed passive optical network (TWDM-PON) for next-generation PON stage 2 (NG-PON2). *Journal of Lightwave Technology*, 31, 587–593.
- [8] Iannone, P., Gnauck, A., Veen, D., & Houtsma, V. (2016). Increasing TDM Rates for Access Systems Beyond NG-PON2. *Journal of Lightwave Technology*, 34(6), 1545-1550.
- [9] Pizzinat, A., Chanclou, P., Saliou, F., & Diallo, T. (2015). Things You Should Know About Fronthaul. *Journal of Lightwave Technology*, 33(5), 1077-1083.
- [10] Hossain, A., Dorsinville, R., Ali, M., Shami, A., & Assi, C. (2006). Ring-based local access PON architecture for supporting private networking capability. *Journal of Optical Networking*, 5(1), 26-39.
- [11] IEEE Standard for Ethernet. (2012). Retrieved from <https://standards.ieee.org/about/get/802/802>.
- [12] Kramer, G., Mukherjee, B., & Pesavento, G. (2002). IPACT: A Dynamic Protocol for an Ethernet PON (EPON). *IEEE Communications Magazine*, 40(2), 74-80.
- [13] Shen, G., Tucker, R., & Chae, C. (2007). Fixed Mobile Convergence Architectures for Broadband Access: Integration of EPON and WiMAX. *IEEE Communications Magazine*, 45(8), 44-50.
- [14] LTE-Advanced: Technology and Test Challenges. (2014). Retrieved from literature.cdn.keysight.com/litweb/pdf/5990-6706EN.pdf

Biographies

ASM DELOWAR HOSSAIN is an associate professor of Electrical Engineering Technology at The City University of New York. He earned his BS, MS, and PhD (2007) degrees in Electrical Engineering from The City University of New York. Dr. Hossain's interests include wireless and optical access networks. Dr. Hossain may be reached at ahossain@citytech.cuny.edu

MUHAMMAD UMMY is an associate professor of Electrical Engineering Technology at The City University of New York. He earned his BS (Mechanical Engineering, 1996), and PhD degrees (Electrical Engineering, 2008) from The City University of New York. Dr. Ummy's interests include fiber optics communications, fiber sensors, and fiber lasers. Dr. Ummy may be reached at maummy@citytech.cuny.edu

ABDULLAH HOSSAIN is a graduate student at The City University of New York. He earned his BS (Electrical Engineering, 2017) degree from The City University of New York. Mr. Hossain's interests include fiber optics communications. Mr. Hossain may be reached at ahossai12@citymail.cuny.edu

PROBABILISTIC MODELS FOR CRITICAL RESPONSES OF HIGH-RISE BUILDINGS

Mohammad T Bhuiyan, West Virginia State University; Roberto Leon, Virginia Tech

Abstract

Probabilistic performance-based design and assessment of structures takes into account the uncertainty in the estimation of seismic hazards, structural response (as a function of the ground motion intensity level), and structural capacity. The objective of this study was to develop statistical models for critical building responses (such as roof drift, roof acceleration, base shear, etc.) which might help in the development and/or assessment of guidelines for the seismic design of high-rise buildings. A 64-story diagrid high-rise building was selected for this study. A total of 435 non-linear time-history analyses were conducted in OpenSees, utilizing 145 recorded earthquake events of various magnitudes and distance bins.

The results indicated that roof drift ratio correlates well to spectral acceleration in the 1st mode period; roof acceleration correlates better to PGA (peak ground acceleration); base shear correlates better to spectral acceleration in the 2nd mode period; and, base moment correlates more to spectral acceleration in the 1st mode structural period. Further results showed that if a structure with a fundamental period of 5.0 seconds is designed for the Los Angeles area then a 0.6% roof drift will have a probability of exceedance of 10% for a 100-year lifetime. And a base shear of $0.25W$ (where, W is the seismic weight of the structure) has an annual rate of exceedance of $3.2e-3$ or a return period of roughly 300 years.

Introduction

The objectives of this study were to: 1) conduct a very large number of nonlinear dynamic analyses of tall buildings utilizing ground motions selected from various magnitudes and distance bins; 2) characterize key building responses to these ground motions; and, 3) develop statistical models for these critical building responses, which might help in the development and/or assessment of guidelines for the seismic design of high-rise buildings. For example, the kind of answer sought were:

- What is the annual rate (probability) that the roof drift ratio will exceed 1%?
- What should be the median roof drift ratio if one is designing the structure for a lifetime of 75 years?

The study was motivated by the work of the PEER Tall Building Initiative [2], where studies were performed with similar objectives for several concrete high-rise buildings.

Theoretical Foundation for Developing Statistical Models

The theoretical development for this study was based on the methodology developed by Jalayer and Cornell [1]. The probabilistic foundation developed here involved the derivation of a closed-form expression for the mean annual frequency of exceeding a specified limit state. The term “limit state frequency” will be used from now on for “the mean annual frequency of exceeding a specified limit state.” H_{LS} is defined as the product of the mean rate of occurrence of events with seismic intensity larger than a certain minimum level, ν , and the probability that demand D exceeds capacity C , when such an event occurs. This relationship is shown in Equation (1):

$$H_{LS} = \nu.P[D > C] \quad (1)$$

In order to determine H_{LS} , the strategy is to decompose the problem into more tractable pieces and then re-assemble them. First, a ground motion intensity measure, IM, (such as the spectral acceleration, S_a , at the 1st mode structural period) is introduced because a) the level of ground motion is the major determinant of the demand D , and b) this permits separation of the problem into a seismological part and a structural engineering part. To do this, a standard tool in applied probability theory, known as the total probability theorem (TPT), was used. This theorem permits the breakdown of the expression for limit state frequency with respect to an interface variable (here, the spectral acceleration). This is represented by Equation (2):

$$H_{LS} = \nu.P[D > C] = \nu.\sum_{\text{all } x} P[D > C | S_a = x].P[S_a = x] \quad (2)$$

In simple terms, the problem of calculating the limit state frequency was broken down into two problems. The first problem was to calculate the term $P[S_a = x]$, or the likelihood that the spectral acceleration will equal a specified level, x . This likelihood (together with ν) is a number we can get from a probabilistic seismic hazard analysis (PSHA) of the site. The second problem was to estimate the term $P[D > C | S_a = x]$, or the conditional limit state probability for a given level of ground motion intensity, here represented by $S_a = x$.

The hazard corresponding to a specific value of the ground motion intensity measure (or spectral acceleration, S_a) is defined as the mean annual frequency that the intensity of future ground motion events are greater than or equal to that specific value x and denoted by $H_{S_a}(x)$. The spectral acceleration hazard, referred to as $H_{S_a}(x)$, can be defined as the product of the rate parameter ν and the probability of exceeding the spectral acceleration value, x , denoted by $G_{S_a}(x)$, as given by Equation (3):

$$H_{S_a}(x) = \nu \cdot G_{S_a}(x) \quad (3)$$

The spectral acceleration hazard values, $H_{S_a}(x)$, are usually plotted against different spectral acceleration values, x ; this results in a curve that is usually referred to as a spectral acceleration hazard curve. It is advantageous to approximate such a curve in the region of interest by the power-law relationship [3] of Equation (4):

$$H_{S_a}(S_a) = P[S_a \geq x] = k_0 \cdot x^{-k} \quad (4)$$

where, k_0 and k are parameters defining the shape of the hazard curve.

Figure 1 shows a typical hazard curve for a southern California site that corresponds to a period of 1.8 seconds. As can be seen from this figure, a line with slope k and intercept k_0 is fit to the hazard curve (on the two-way logarithmic paper) around the region of interest (e.g., mean annual frequencies between 1/475 or 10% frequency of exceedance in 50 years, and 1/2475 or 2% frequency of exceedance).

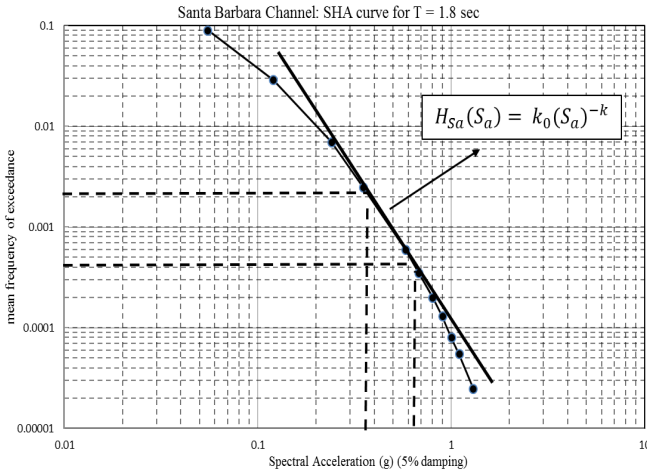


Figure 1. Typical Hazard Curve for Spectral Acceleration Corresponding to a Structural Fundamental Period of 1.8 Seconds

Note. From “A technical framework for probability-based demand and capacity factor design (DCFD) seismic formats,” by F. Jalayer, and A. Cornell, 2003, *PEER Report*. Reprinted with permission.

Median Relationship between Spectral Acceleration and Roof-Drift Demand

Observations of demand values are normally obtained from the result of structural time-history analyses performed for various ground motion intensity levels. Figure 2 shows such results for maximum roof drift, D , versus S_a . This figure also shows data points from an analysis that will be described later in this paper. For a given level of ground motion intensity, there will be variability in the demand results over any suite of ground motion records applied to the structure. It is convenient to introduce a functional relationship between the ground-motion intensity measure and a central value, specifically the median, η_D , of the demand parameter based on the data available from such time history analyses. In general, for a spectral acceleration equal to x , the functional relationship will be as given in Equation (5):

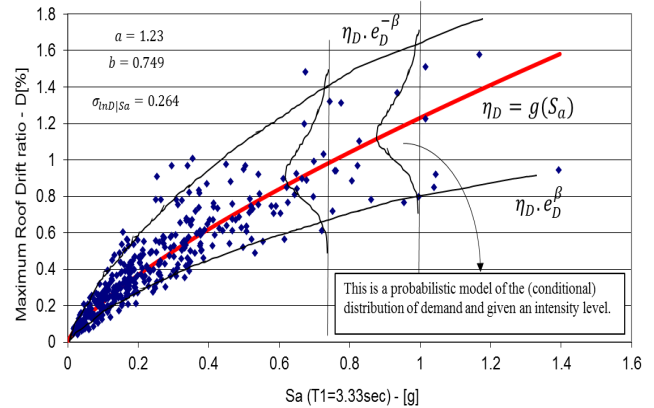


Figure 2. Spectral Acceleration and Demand Data Pairs, and the Regression Model Fit to These Data Points

$$\eta_D(x) = g(x) \quad (5)$$

This is called the conditional median of D given S_a (more formally denoted by $\eta_{D|S_a}(x)$, but the simpler notation was kept for this study). A full conditional probabilistic model can be constructed with the variability displayed in Figure 2 by using Equation (6):

$$D = \eta_D(x) \cdot \varepsilon = g(x) \cdot \varepsilon \quad (6)$$

where, ε is a random variable with a median equal to unity and a probability distribution to be lognormal. Linear regression is used in logarithmic space (i.e., $\ln \eta_D(x) = \ln a + b \ln x$).

Such a regression will result in the relationship of Equation (7) between spectral acceleration and (median) roof drift response:

$$\eta_D(x) = a \cdot x_a^b \quad (7)$$

A closed-form expression for the mean annual frequency of exceeding a certain demand value, d , also known as the drift hazard, $H_D(d)$, was derived by Jalayer and Cornell [1] and shown here as Equation (8):

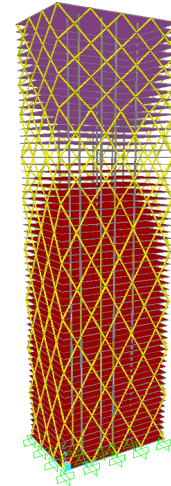
$$H_D(d) = k_0 \left(\frac{d}{a}\right)^{\frac{-k}{b}} \cdot e^{\frac{1}{2} \frac{k^2}{b^2} \beta_{D|S_a}^2} \quad (8)$$

Development of Statistical Models for Critical Building Responses

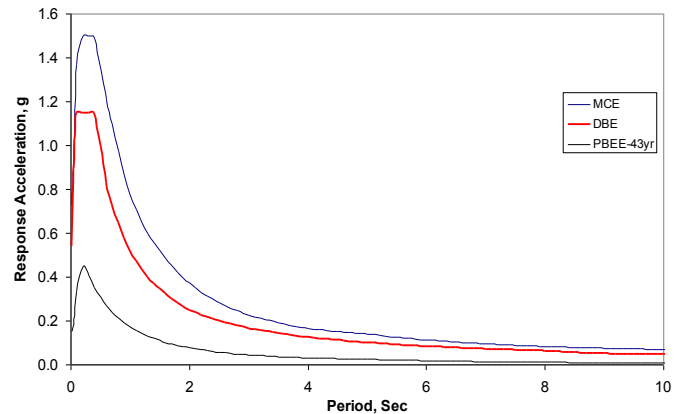
Statistical models for different critical building responses such as roof drift, roof acceleration, and base shear will be developed based on the theory presented here using the 64-story structure shown in Figure 3(a). One-hundred-forty-five ground motion events were used for this purpose. These ground motion events were provided by a research team from the PEER Center at the University of California Berkeley [5]. Three-component input ground motion events were used in the 3D non-linear time history analyses (NLTHA). Ground motion scaling factors of 1, 2, and 4 were used for all of the events; this meant that a total of 435 NLTHA were conducted in OpenSees for the 64-story diagrid building.

Figure 4 shows the variations in the structural responses. Figures 4(a) and 4(b) show the responses only for the ground motion events with a scaling factor (SF) of one. The images in Figure 4 also show a large variability in the responses observed, which means that the structural responses were very sensitive to the ground motion events. Higher-mode effects are visually noticeable in these figures. Figure 4 further shows the mean response and mean, plus or minus one standard deviation. A particular observation can be made from Figure 4(a), where maximum story accelerations are plotted. It is quite interesting to see that story accelerations are high throughout the height of the building, in the case of high-rise buildings. Figure 5 illustrates the effects of the scaling factor. The mean of the responses for each scaling factor are shown in those figures, which show the relative magnification in the responses when the input ground motion events are scaled by factors of 1, 2, and 4.

It is necessary to find the appropriate ground-motion parameter that correlates best with the engineering design parameter (EDP) of interest, such as roof drift, roof acceleration, base shear or others. Consider first the maximum roof drift in the x-direction. For each NLTHA, one value of absolute maximum roof displacement in x-direction from the time-series and ground-motion parameters for that particular input motion in x-direction were calculated.



(a) 3D View of the 64-Story Structure



(b) Response Spectrum Used in This Study

Figure 3. The 64-Story Structure Used to Develop the Theory and Statistical Models for This Study

Figure 6 presents a plot of maximum roof drift in x-direction versus spectral acceleration at the 1st mode structural period in x-direction ($T_{1X} = 3.33$ sec). Figure 7(a) shows a plot of maximum roof drift in the x-direction versus spectral acceleration in the 2nd mode structural period in x-direction ($T_{2X} = 0.91$ sec). Similarly, plots of roof drift versus other ground motion parameters are presented elsewhere [4]. After a close observation, it is evident that the roof-drift ratio correlates well with spectral acceleration at the 1st mode period ($Sa[TI]$). Similarly, it was found that roof acceleration correlates better with PGA [see Figure 7(b)], base shear correlates better with spectral acceleration in the 2nd mode period [see Figure 7(c)], and base moment correlates better with spectral acceleration at the 1st mode structural period. Therefore, it is evident that, for a high-rise building, it might not be a good idea to characterize EDP with a single ground-motion parameter.

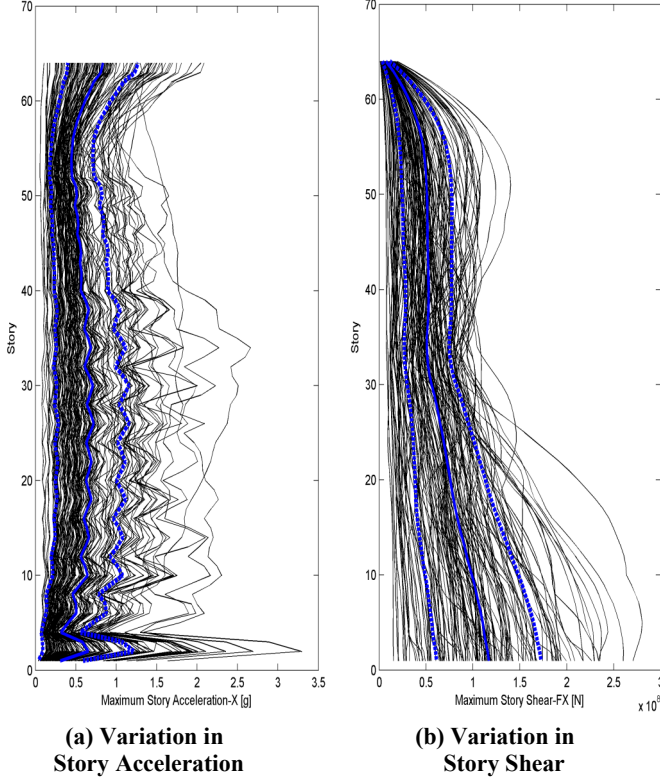


Figure 4. Variations in the Structural Responses of the Building [only motions with SF=1 are shown; mean and mean \pm std are also shown]

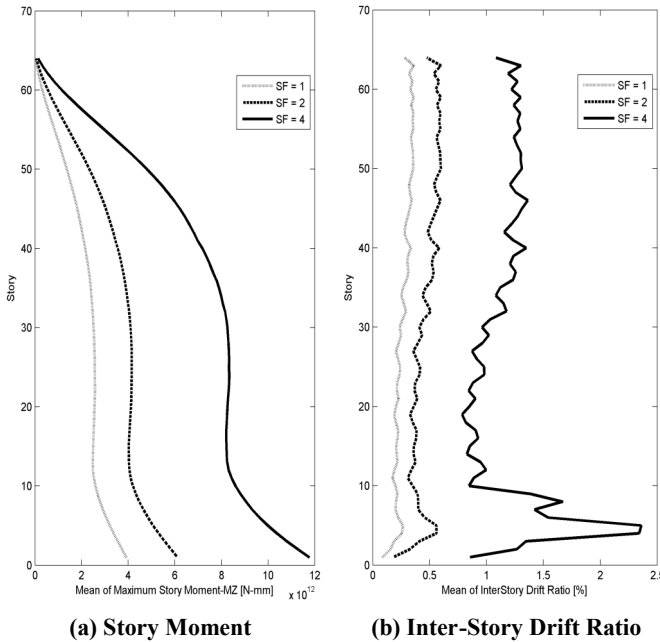


Figure 5. Effects of the Scaling Factor [mean of the responses for each SF]

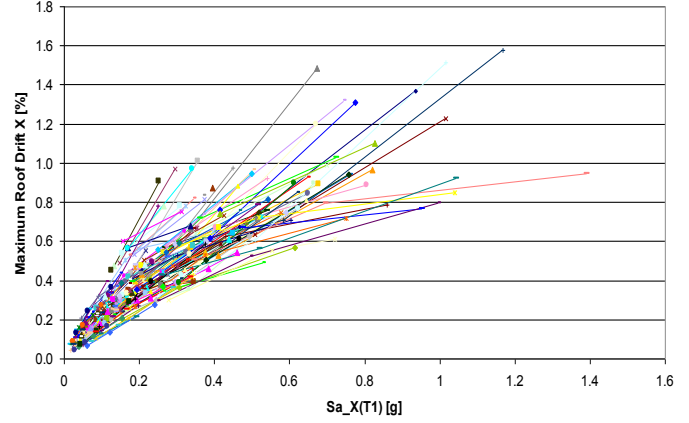


Figure 6. Roof Drift Ratio versus Spectral Acceleration at the 1st Mode Structural Period

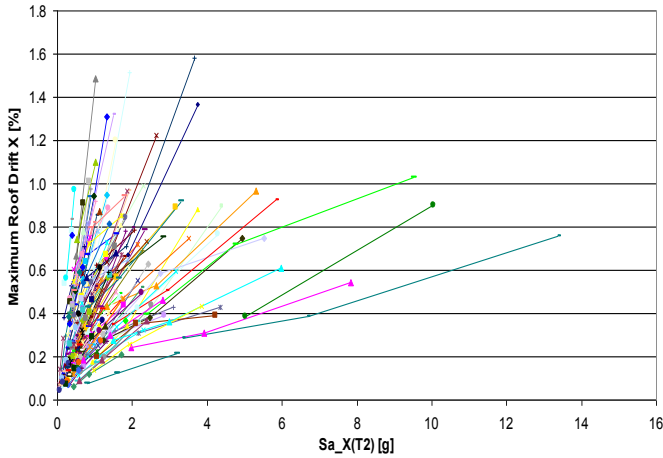
These findings can be used in performance-based designs for high-rise buildings in order to answer such questions as: 1) what is the annual rate (probability) that the roof-drift ratio will exceed 1%?, and 2) what should be the target median roof-drift ratio over a lifetime of 75 years?

Probabilistic Model of EDP Responses

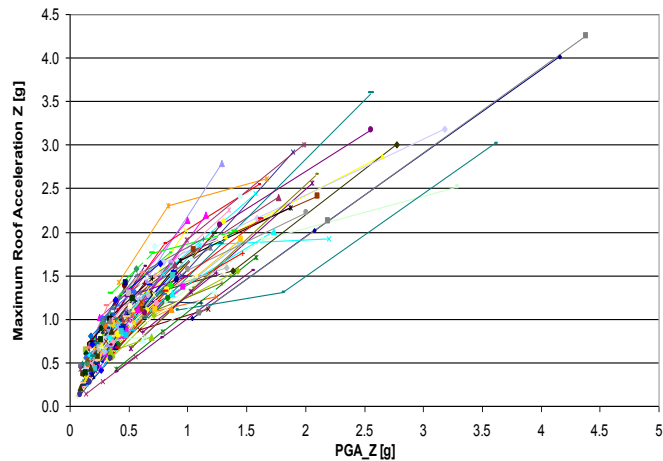
Findings from this study and the theoretical background presented previously were used to develop probabilistic models for critical building responses. First, it is necessary to determine the constants k and k_0 [see Equation (3) and Figure 1] to represent the spectral acceleration hazard curve with a power-law relationship. The technique for obtaining these constants by using spectral acceleration values for 475-year and 2475-year return periods was described earlier. The spectral acceleration values for the 475-year (10% probability of exceedance in 50 years–DBE) and 2475-year (2% probability of exceedance in 50 years–MCE) return periods can be obtained from Figure 3(b), where MCE and DBE response spectra are plotted. The value of k can be calculated using Equation (9):

$$k = \frac{\ln\left(\frac{H_{s(10/50)}}{H_{s(2/50)}}\right)}{\ln\left(\frac{S_{(10/50)}}{S_{(2/50)}}\right)} = \frac{1.65}{\ln\left(\frac{S_{(10/50)}}{S_{(2/50)}}\right)} \quad (9)$$

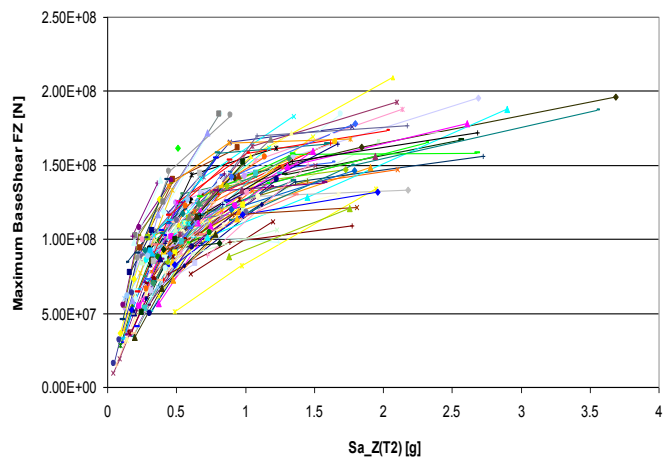
where, $S_{(10/50)}$ is the spectral amplitude for the 10/50 hazard level; $S_{(2/50)}$ is the spectral amplitude for the 2/50 hazard level; $H_{S(10/50)}$ is the probability of exceedance for the 10/50 hazard level = $1/475 = 0.0021$; and, $H_{S(2/50)}$ is the probability of exceedance for the 2/50 hazard level = $1/2475 = 0.00404$.



(a) Roof-Drift Ratio versus Spectral Acceleration



(b) Roof Acceleration versus PGA



(c) Base Shear versus Spectral Acceleration

Figure 7. Roof Drift, Spectral Acceleration, Roof Acceleration, and Base Shear for the 2nd Mode Structural Period

Figure 8 shows the plot of the roof-drift ratio (in the z-direction) from NLTHAs and a fitted regression curve for the 1st mode period (5.0 seconds). Following the methodology described previously, the hazard curve for the roof-drift ratio is presented in Figure 9(a). This curve shows the annual rate of exceedance of roof drift, but it is extremely important to point out that it is applicable only for the Los Angeles area and for a building of the same 1st mode structural period of 5.0 seconds. From this figure, it can be seen that a 1% roof-drift ratio has an annual rate of exceedance of $4e-5$, or a return period of about 25,000 years. Figure 9(b) illustrates the Poissonian probability of exceedance for roof-drift values for structural lifetimes of 50, 75, and 100 years. Also from this figure, if a structure with a fundamental period of 5.0 seconds is designed for the Los Angeles area then a 0.6% roof drift will have a probability of exceedance of 10% over a 100-year lifetime.

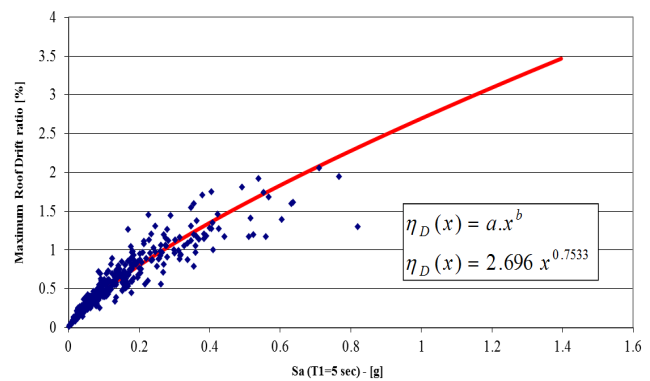
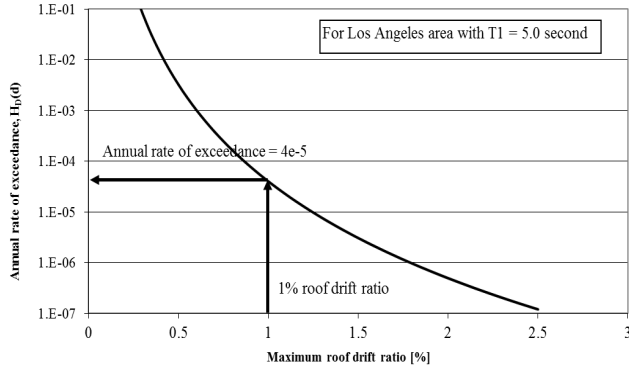


Figure 8. Roof-Drift Ratio from NLTHAs and Fitted Regression Curve for a 1st Mode Structural Period of 5.0 Seconds

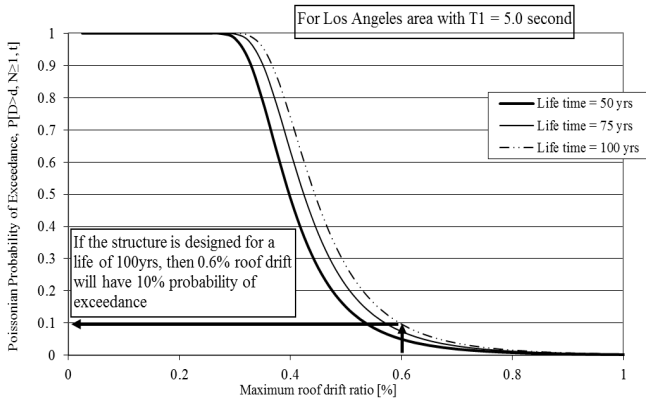
Similarly, Figure 10 shows the hazard curve and Figure 11(a) depicts the Poissonian probability of exceedance of roof drift for a 1st mode structural period of 3.33 seconds. Now, from Figures 9(b) and 11(a), roof-drift values corresponding to 2% probability of exceedance in 50 and 100 years can be extracted and are plotted in Figure 11(b). The horizontal axis of Figure 11(b) represents the fundamental period of vibration of a structure whose performance is sought. The concept shown in this figure is similar to that of a response spectrum. The trend in Figure 11(b) can be predicted with a few more points with different fundamental periods of vibration.

Figure 12 shows the plot of base shear (in z-direction) from NLTHAs and a fitted regression curve for the 2nd mode structural period of 1.429 seconds. The hazard curve for base shear is presented in Figure 13, which shows the annual rate of exceedance of base shear. From this figure, it can be seen that a base shear of $0.25W$ (where, W is the

seismic weight of the structure) has an annual rate of exceedance of 3.2×10^{-3} , or a return period of roughly 300 years. Figure 14 illustrates the Poissonian probability of exceedance for base-shear values structural lifetimes of 50, 75, and 100 years.



(a) Hazard Curve for Roof-Drift Ratio



(b) Poissonian Probability of Exceedance of Roof Drift

Figure 9. Hazard Curve and Poissonian Probability of Exceedance for a 1st Mode Structural Period of 5.0 Seconds

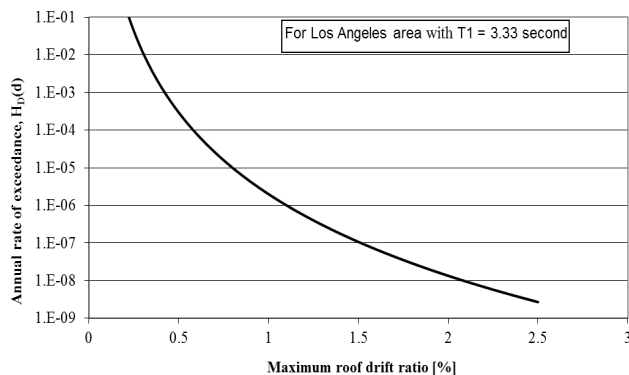
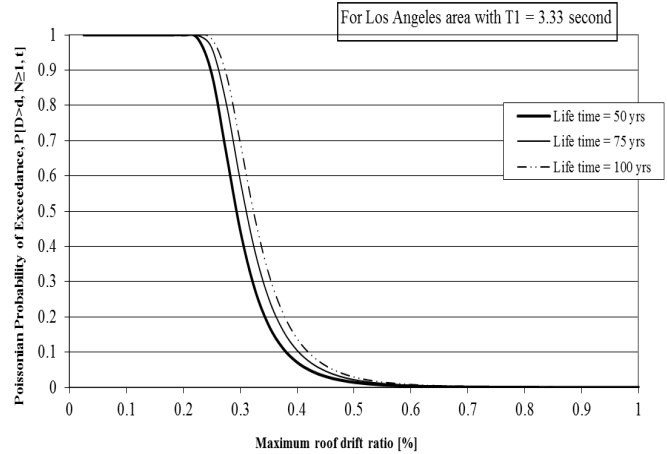
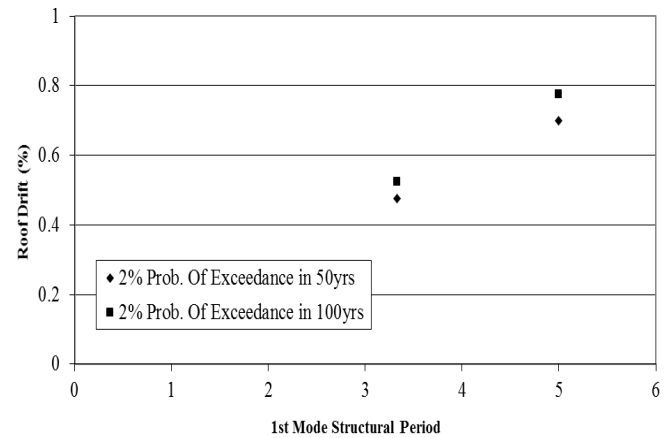


Figure 10. Hazard Curve for Roof-Drift Ratio for a 1st Mode Structural Period of 3.33 Seconds



(a) Poissonian Probability of Exceedance of Roof Drift



(b) Performance of a Structure (defined by fundamental period of vibration)

Figure 11. Poissonian Probability of Exceedance for a 1st Mode Structural Period of 3.33 Seconds

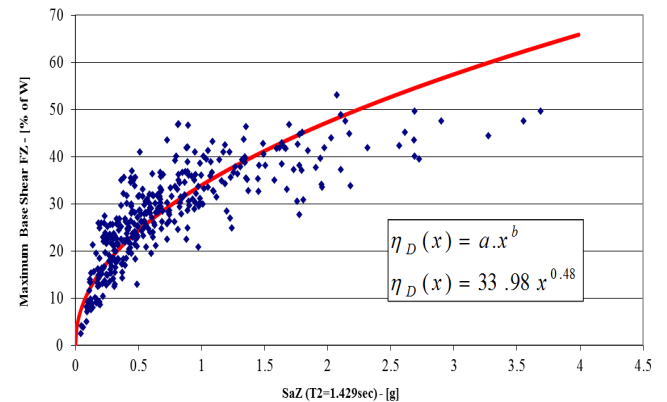


Figure 12. Base Shear from NLTHAs and Fitted Regression Curve for a 2nd Mode Structural Period of 1.429 Seconds

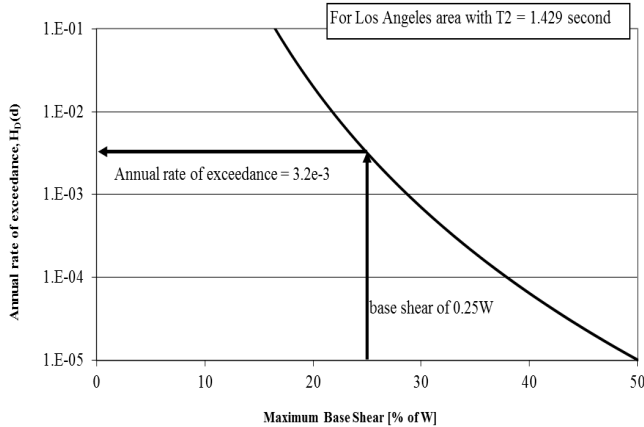


Figure 13. Hazard Curve for Base Shear for a 2nd Mode Structural Period of 1.429 Seconds

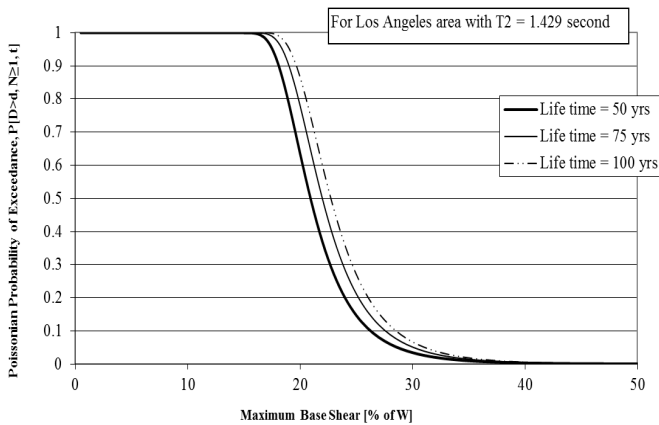


Figure 14. Poissonian Probability of Exceedance of Base Shear for a 2nd Mode Structural Period of 1.429 Seconds

Conclusion

Statistical models for several critical building responses were developed using diagrid tall buildings. These probabilistic characterizations will help in the development and/or assessment of guidelines for the seismic design of high-rise buildings. A total of 435 3D-NLTHAs were conducted to develop probabilistic models of critical building responses (such as roof drift, base shear, etc.). Mathematical models for EDP and ground-motion intensity were developed from regression analyses. Then, annual rate of exceedance and Poissonian probability of exceedance values for each EDP were calculated and plotted. Results indicated that the annual rate of exceedance for roof drift for a building with 1st mode structural period of 5.0 seconds was roughly $4e-5$, or a return period of 25,000 years. Similarly, a structure with a fundamental period of 5.0 seconds and designed for the Los Angeles area for a 0.6% roof-drift limit would have a probability of exceedance of 10% over a 100-year lifetime.

References

- [1] Jalayer, F., & Cornell, A. (2003). *A technical framework for probability-based demand and capacity factor design (DCFD) seismic formats*. PEER Report 2003/08.
- [2] Yang, T., Moehle, J., Mahin, S., Bozorgnia, Y., & McQuoid, C. (2008). Case studies to characterize the seismic demands for high-rise buildings. Presentation at the Annual meeting of the LA Tall building structural design council, Los Angeles, CA.
- [3] DOE. (1994). *Natural phenomena hazards design and evaluation criteria for Department of Energy Facilities*. DOE-STD-1020-94, U.S. Dept. of Energy, Washington, D.C.
- [4] Bhuiyan, M. T. R. (2011). *Response of Diagrid Tall Building to Wind and Earthquake Actions*. Unpublished doctoral dissertation, ROSE School, Pavia, Italy.
- [5] Mahin, S., Yang, T., & Bozorgnia, Y. (2008). Personal Communication between authors.

Biographies

MOHAMMAD T BHUIYAN is an assistant professor of Civil Engineering at West Virginia State University. He earned his BSc in Civil Engineering from Bangladesh University of Engineering and Technology, Dhaka; an MSc in Earthquake Engineering jointly from Universite Joseph Fourier, France, and ROSE School, Italy; and a PhD in Earthquake Engineering from ROSE School with a joint program at Georgia Tech, Atlanta. His research interests include tall buildings, earthquake engineering, and soil-structure interaction. Dr. Bhuiayn may be reached at towhid@wvstateu.edu

ROBERTO LEON is a D.H. Burrows Professor in the department of Civil and Environmental Engineering at Virginia Tech. He is a nationally and internationally recognized faculty member for his research, teaching, and service. He is acknowledged to be one of the leading researchers in the field of steel-concrete composite structures and earthquake engineering. His work has affected numerous national and international design codes. He was president of the Consortium of Universities for Research in Earthquake Engineering (CUREE) and president of the Network for Earthquake Engineering Simulation (NEES). He also served as president of the Board of Governors of the Structural Engineering Institute (SEI) of ASCE. Dr. Leon may be reached at rleon@vt.edu

PHASE TRANSITIONS IN INTERCONNECTION NETWORKS WITH FINITE BUFFERS

Yelena Rykalova, UMass Lowell; Lev B. Levitin, Boston University

Abstract

In this paper, the authors present theoretical models and simulation results for performance of a multiprocessor network modeled as a ring and as a two-dimension wraparound square lattice of nodes with local processors that generate messages with constant rates per time slot. The buffers can hold a limited number of messages. Explicit theoretical results based on first-order (independent queues) and second-order approximation of the queue distributions were obtained for small buffer sizes (1 and 2). For larger buffers the problem appeared analytically intractable and were analyzed through simulations. The average queue lengths and average latency were obtained. The results showed that the model of independent queues, which is valid for networks with infinite buffers, is still applicable for small generation rates, but breaks down for larger loads, which violates the Jackson theorem.

Introduction

Over the last several decades the efforts of many researchers were focused on analyzing computer communication networks as networks of queues. Most of the early important results were obtained for networks with infinite buffers. However, this assumption in many cases does not adequately depict real networks. In practice, buffers are finite, and sometimes quite small. There is a rise of interest in recent years in the performance of networks with small buffers. Analyses showed [1-4] that increase in buffer size does not significantly improve performance in wormhole routing. Moreover, latest research [5-11] proved that the use of smaller buffers does not decrease link utilization for Internet routers.

In interconnection networks, a buffer depth of five packets was shown to offer optimal performance for optical packet-switched clockwork routing [12]. Buffers of size 1, 2, and 50 messages were considered in a study by Rykalova et al. [13]. Larger buffers sizes (5, 10, 20, 30, 40, and 50) were studied by Levitin and Rykalova [14]. The use of smaller buffer sizes offers some advantage in speed and provides possibilities for the use of SRAM or OPS (Optical Packet Switching). Therefore it is very important to study such networks, in spite of analytical difficulties this may present.

In this study, the authors considered several models of networks with different buffer sizes, starting with one; that is, only one message can be kept in a buffer. In general, theoretical analysis of such networks is a very challenging problem. Though the independent-queues assumption is not expected to give an accurate description of the performance of networks with finite buffers, it still makes sense to analyze the networks in terms of the first-order probability distributions (as if the queues were independent). In order to better reflect the correlations between nodes, the second-order probabilities (i.e. joint probabilities of two neighboring nodes) were obtained for certain models. A comparison with simulation results showed that both the first-order probabilities, and especially the second-order distributions, yielded a reasonably good description of the system's behavior until the load reached the critical region.

The simulation results show that when the load approached the critical value, the system's behavior displayed typical patterns of long-range dependences between nodes, on the scale far exceeding the "interaction radius" (the distance between the source and destination). The network performance near the critical point was beyond the framework of Jackson theorem [15]; rather it was similar to the critical phenomena in systems described by statistical physics. Both second-order and first-order phase transitions were observed in networks with finite buffers. Fluctuations with very large amplitudes, slowly changing in time, and instabilities in critical region are characteristic features of the network behavior.

All of the models noted below have the following common properties:

1. All nodes in the network are both the routers and hosts: every node can generate and receive messages as well as store and send further passing messages.
2. Time is discrete: all nodes simultaneously send, receive and generate messages within every time slot.
3. Each node generates at most one message per output port within every time slot with a certain probability. This probability may depend on the state of the node (the number of messages in the local output port).
4. Destination of a message is selected with equal probabilities among the nodes at an exact distance l from the source.
5. Service time is deterministic (therefore, it does not have a rational Laplace transform). In the absence of

queues, a message received or generated during a time slot will appear at the next node in the next time slot.

6. If possible, a message (if there is one) is sent from the output port to the neighboring node at every time slot. This depends on the number of messages in the output port (for the ring topology), or in the router (for the torus topology) in the next (neighboring) node.

In the case of limited buffers, the next state of a buffer depends not only on its previous state (as in the case of infinite buffers), but also on the previous state of its neighbor. The difference between this current work and previous studies [16-18] is in particular, the choice of model features such as discrete time and deterministic service time. While some features of the models used in this study were similar to those used by others [19], no model to-date has incorporated all of them. The authors believe that the reason is that the combination of properties, as described above, makes this model closer to a real supercomputer network, though it is sometimes hard for theoretical analysis. Choice of the deterministic service time implies that, for this model, the service time does not have a rational Laplace transform. The buffer capacities of $m = 1$ and $m = 2$ were chosen for the theoretical model in order to obtain explicit analytical expressions for the steady-state probabilities (first-order probability distribution) of the states and the average queue length in the "mean field" theory similar to that in statistical physics. Explicit expressions for the second-order distributions were also obtained. Experimental results based on simulation were obtained for the ring length of 500 routers and the distance between source and destination of $l = 5$ hops. Later, the authors provide experimental results for a 16×16 toroidal square lattice and $l = 5$ hops.

Ring Topology

In the case of buffer size $m = 1$, it was assumed that a node neither accepts messages nor generates messages, when the number of messages in a buffer is $n = 1$. If, at the beginning of a time slot, a node was in state 0 and then received an incoming message that was not consumed, it would not generate any new message. For a first-order probability distribution, under the assumption of independent queues, the queue state transitions form a simple two-state Markov chain. The balance equation $p_0 p_{01} = p_1 p_{10} = (1 - p_0) p_{10}$ yields Equation (1):

$$p_0 = \frac{1 - \lambda(l+1)}{1 - \lambda}, \quad \bar{n}^{(1)} = p_1 = \frac{\lambda l}{1 - \lambda} \quad (1)$$

$$\lambda_{crit}^{(1)} = \frac{1}{l+1}, \quad \tau^{(1)} = \frac{(1 - \lambda)l}{1 - \lambda(l+1)}$$

where, λ is the nominal probability that a message is generated by a node within one time interval; \bar{n} is the average number of messages in a buffer; and, τ is the average latency.

The actual generation rate, λ_{act} , in all of the models in this study with finite buffers was different from the nominal value λ . Indeed, in the model with $m = 1$, a new message could be generated in state 0 only if no passing message has arrived, and in state 1 only if the message kept in the output buffer has been sent to the next node. A calculation shows that in the first-order approximation the actual generation rate is given by Equation (2):

$$\lambda_{act}^{(1)} = p_0 \lambda \left(1 + \frac{p_1}{l} \right) = \frac{\lambda(1 - \lambda(l+1))}{(1 - \lambda)^2} \quad (2)$$

For a second-order probability distribution, for two neighboring nodes and their combined states the Markov chain has four states. After solving the system of balance equations for this Markov chain, Equations (3) and (4) are obtained:

$$p_0 = 1 - \frac{\lambda l^2(1 - \lambda l)}{\lambda + l(1 - 3\lambda) - \lambda^2(l+1)(l-1)^2} \quad (3)$$

$$\bar{n}^{(2)} = p_1 = \frac{\lambda l^2(1 - \lambda l)}{l - \lambda(3l - 1) - \lambda^2(l+1)(l^2 - 1)}$$

$$\lambda_{crit}^{(2)} = \frac{l^2 + 3l - 1 + \sqrt{(l^2 + 3l - 1)^2 - 4l(l^2 + 3l - 1)}}{2(l^2 + l - 1)}$$

$$\lambda_{act}^{(2)} = p_0 \lambda \left(1 + \frac{p_1}{2l} \right) \quad (4)$$

$$\tau^{(2)} = \frac{\bar{n}^{(2)}}{\lambda_{act}^{(2)}} = \frac{2p_1 l}{\lambda(1 - p_1)(2l + p_1)}$$

For comparison, the corresponding theoretical values for a system with infinite buffers are [20, 21] can be found using Equations (5) and (6):

$$\bar{n} = \bar{n}(\lambda) = \sum_{n=1}^{\infty} nP(n) = \frac{\lambda^2(l-1)}{1 - l\lambda} + l \quad (5)$$

$$\tau = \frac{\lambda(l-1)}{1 - l\lambda} + l \quad (6)$$

Experimental Results

Figure 1 shows the values of \bar{n} from the simulation together with theoretical approximations $\bar{n}^{(1)}$ and $\bar{n}^{(2)}$. The solid red line represents the first-order approximation $\bar{n}^{(1)}$ of Equation (1); the dashed green line represents the second-order approximation $\bar{n}^{(2)}$ of Equation (3); the blue line with bullets shows the experimental data; and, the dotted orange line depicts the theoretical values for infinite buffers given by Equation (5). One can see that the second-order theoretical analysis, compared to the first-order approximation, provides a much better prediction of the network behavior for small network loads up to $\lambda \approx 0.7\lambda_{crit}$. It also can be seen that the second-order analysis results in a better approximation of the real critical point: second-order $\lambda_{crit}^{(2)} = 0.1435$ versus first-order $\lambda_{crit}^{(1)} = 0.1667$.

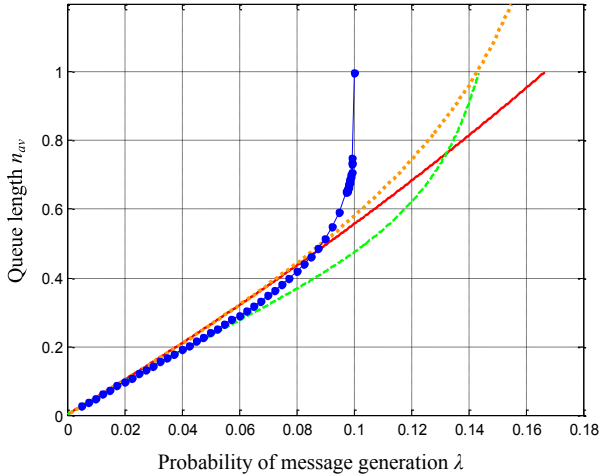


Figure 1. Queue Length, \bar{n} , as a Function of Network Load λ

The interesting observation is that the network performed better than theory of the independent queues predicts. Paradoxically, the first-order approximation gives an upper bound on \bar{n} for small network loads when the probability of message generation is $\lambda < 0.8\lambda_{crit}$, while the second-order approximation provides a lower bound on \bar{n} for all λ . Figure 2 shows a plot of the empirical value of the latency τ , its analytical approximation, $\tau^{(1)}$ and $\tau^{(2)}$, and the latency τ_{inf} for the network with infinite buffers. The solid red line represents the first-order approximation $\tau^{(1)}$ of Equation (1); the dashed green line shows the second-order approximation $\tau^{(2)}$ of Equation (4); the blue line with bullets depicts the experimental data; and, the dotted orange line represents theoretical values for infinite buffers given by Equation (6).

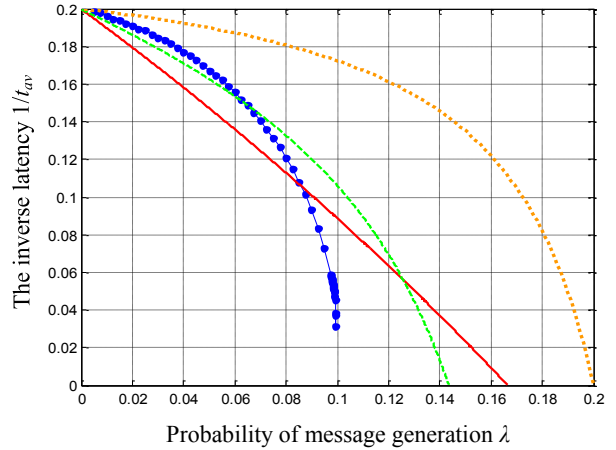


Figure 2. Inverse Average Latency, τ , as a Function of Network Load λ

A remarkable result is that the actual latency, τ , was considerably smaller than $\tau^{(1)}$ for $\lambda < 0.6\lambda_{crit}$, and close to, but slightly smaller than $\tau^{(2)}$ for $\lambda < 0.6\lambda_{crit}$. The reason for this paradoxical behavior is that, in the first-order approximation (independent queues) the probability of having a pair of neighboring nodes both in state 1, namely, $p_{11} = p_1^2$ is substantially larger than in the reality: a pair (11) is unstable at small values of λ and most probably will become (10) pair of states at the next time interval, since a node in state 1 does not accept messages. Thus, states 0 and 1 were negatively correlated for small λ and positively correlated for large λ ($\lambda > 0.85\lambda_{crit}$). It is tempting to compare this phenomenon with the antiferromagnetic-ferromagnetic transition in solid-state physics. The network behavior near the critical point displays a pattern of the second-order phase transition. The average latency, τ , follows the power law of Equation (7):

$$\tau(\lambda) = \alpha(\lambda_{crit} - \lambda)^{-\beta} \quad (7)$$

where, λ_{crit} is the critical network load and β is the critical exponent.

The data from the simulation with distance between the source and destination ($l = 5$ hops) yielded $\lambda_{crit} = 0.09981$, $\alpha = 4.891 \pm 0.056$, and critical exponent $\beta = 0.2070 \pm 0.0094$.

Model 1: A Node Neither Accepts Messages nor Generates Messages When $n = 1$ or $n = 2$

In the case of a network with buffer capacity $m = 2$, two models were considered. For a first-order probability distri-

bution, under the assumptions described above, only a router with no messages can accept incoming messages or generate messages with probability λ . Figure 3 shows a state diagram with transition probabilities for this model.

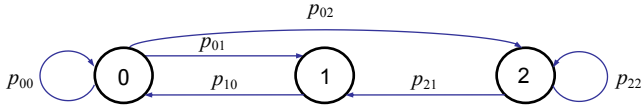


Figure 3. Markov Chain for Buffer Limit $m = 2$, Model 1

Equation (8) shows the system of flow balance equations:

$$\begin{aligned} p_0(p_{01} + p_{02}) &= p_1 p_{10} \\ p_0 p_{02} &= p_2 p_{21} \\ p_0 + p_1 + p_2 &= 1 \end{aligned} \quad (8)$$

The system of flow balance equations of Equation (8) yield Equation (9):

$$\begin{aligned} p_0 &= 1 - \lambda l \\ p_1 &= \lambda l - \lambda^2(l-1)\bar{n}^{(1)} = \lambda l + \lambda^2(l-1) \\ p_2 &= \lambda^2(l-1) \\ \lambda_{act}^{(1)} &= p_0 \lambda = \lambda - \lambda^2 l \\ \tau^{(1)} &= \frac{\bar{n}^{(1)}}{\lambda_{act}^{(1)}} = \frac{l + \lambda(l-1)}{1 - \lambda l} \\ \lambda_{crit}^{(1)} &= \frac{1}{l} \end{aligned} \quad (9)$$

By comparing the expression for $\lambda_{act}^{(1)}$ and $\tau^{(1)}$ for this model and for the model of a network with a buffer limit $m = 1$, one can see that the first-order approximation gives a smaller value of $\lambda_{act}^{(1)}$ and, therefore, a larger latency $\tau^{(1)}$ for $m = 2$, when $\lambda < 0.4 \lambda_{crit}^{(1)}$; but the opposite is true for larger values of λ . The reason for that is that $\lambda_{crit}^{(1)}(m = 2) > \lambda_{crit}^{(1)}(m = 1)$.

For a second-order probability distribution, the second-order approximation becomes more challenging for this model when compared to the second-order approximation described previously. Now, the state transition diagram has nine states, which are combined states of two neighboring nodes. Note that the states are not symmetric, since the messages are always sent from left to right. The global balance equations for such Markov chain as well as probabilities of combined states and marginal probabilities (p_0, p_1, p_2) are too extensive to present here. The equation for λ to solve for $\lambda_{crit}^{(2)}$ is of degree 12 (!). Solving it numerically for $l = 5$ yields the smallest real nonnegative root is shown to be: $\lambda_{crit}^{(2)} = 0.13932314$. The expression for the actual load, $\lambda_{act}^{(2)}$,

has the same form as in the first-order approximation, but the expression for p_0 is different. Correspondingly, the average queue length is $\bar{n}^{(2)}$, as given by Equation (10):

$$\bar{n}^{(2)} = p_1 + 2p_2 \quad (10)$$

Other second-order characteristics are given in Equation (11):

$$\begin{aligned} p_0 &= \frac{(1-\lambda)^2 \pm \sqrt{(1-\lambda)^4 - 4(1-\lambda)\lambda(l-1+\lambda)}}{2(1-\lambda)} \\ p_1 &= \frac{p_0(1-p_0)}{l\lambda} - p_0 \\ p_2 &= 1 - \frac{p_0(1-p_0)}{l\lambda} \\ \lambda_{act}^{(2)} &= (p_0 + p_1)\lambda \\ \bar{n}^{(2)} &= p_0 + 2p_1 \\ \tau^{(2)} &= \frac{\bar{n}^{(2)}}{\lambda_{act}^{(2)}} = \frac{p_0 + 2p_1}{(p_0 + p_1)\lambda} \end{aligned} \quad (11)$$

Numerical Results

Figure 4 shows the approximations for the average queue length $\bar{n}^{(1)}$ and $\bar{n}^{(2)}$, as well as experimental values. The solid red line represents the first-order approximation $\bar{n}^{(1)}$ of Equation (9); the dashed green line represents the second-order approximation $\bar{n}^{(2)}$ of Equation (10); and, the blue line with bullets shows the experimental data.

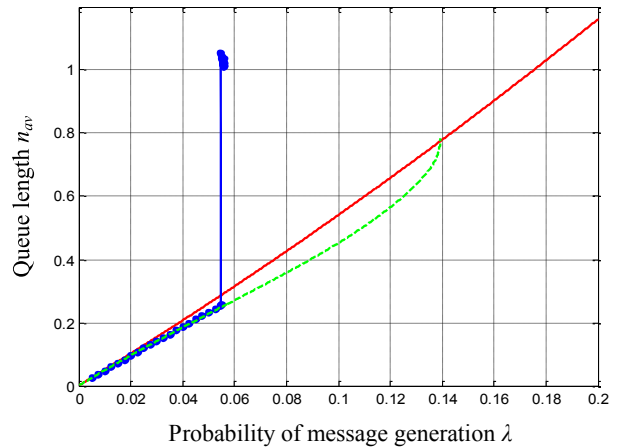


Figure 4. Queue Length, \bar{n} as a Function of Network Load λ

As in the previous model, the second order approximation gives an excellent prediction for network behavior up to the moment when the network becomes saturated. Network goes to the saturation state not only much earlier than the theoretical approximations predict, but it does so abruptly, sharply departing from the second-order approximation curve. Unlike the previous model, there is no continuous transition to the saturation. The picture, then, closely resembles a liquid-gas first-order phase transition. Figure 3 shows that network behavior is very unstable close to the critical point. In one experiment, network goes to saturation; but the next time, even when the network load is larger than before, it does not show any sign of reaching the saturation state. Therefore, in this case, there is a first-order phase transition. The critical load can be roughly estimated as $\lambda_{crit} = 0.0546$.

Model 2: A Node Does Not Accept Messages When $n = 1$ or $n = 2$ and Does Not Generate Messages When $n = 2$

In this section, a second model for the buffer capacity $m = 2$ is considered. Here, a node can generate a message when there is one message in the buffer (state 1), but it does not accept messages when $n = 1$ or $n = 2$. Figure 5 shows the Markov chain for this model.

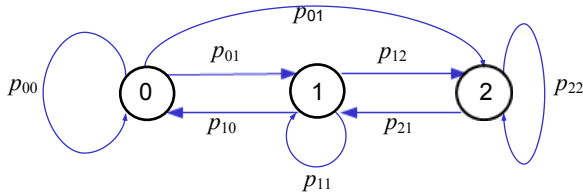


Figure 5. Markov Chain for Buffer Limit $m = 2$, Model 2

The model was described in detail by Rykalova et al. [18]. The second-order probability distribution was not possible to obtain. Using the first-order analysis, the next expressions for actual load, average queue length, and latency were obtained and are given in Equation (12):

$$\begin{aligned} \lambda_{act}^{(1)} &= (p_0 + p_1)\lambda \\ \bar{n}^{(1)} &= p_1 + 2p_2 \\ \tau^{(1)} &= \frac{\bar{n}^{(1)}}{\lambda_{act}^{(1)}} = \frac{p_1 + 2p_2}{(p_0 + p_1)\lambda} \end{aligned} \quad (12)$$

It can be seen that numerical data follow the theoretical prediction very closely, until network load reaches a value of $\lambda \approx 0.0345$. Up to this point, the data from experiments show a slightly better network performance (smaller queue length and latency) than the first-order approximation pre-

dicts. However, Figure 6 shows that numerical experiments indicate a sharp increase in average queue length just before the network reaches saturation and long before the critical transition is expected, according to the mean field theory. Figure 6 shows the queue length \bar{n} as a function of the network load λ . The red line is the first-order approximation $\bar{n}^{(1)}$ of Equation (12) and the blue line with bullets represents the experimental data.

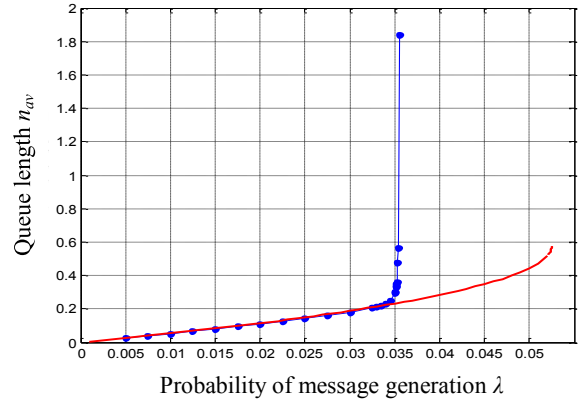


Figure 6. Queue Length, \bar{n} , as a Function of Network Load λ

Figure 7 shows inverse latency, τ , as a function of the network load, λ , where the red line represents the first-order approximation, $\tau^{(1)}$ of Equation (12), and the blue line with bullets represents the experimental data. Figure 8 shows the fluctuations of number of messages in the network during simulation, where the blue line represents the number of messages in the network—averaged over 100 timeslots—and the green line shows the number of messages in the network taken every 100 timeslots. Figure 7 also shows the shape of the latency curve. Figure 8 shows the fluctuation patterns, where the formation of domains of different phases speak in favor of a continuous (second-order) phase-transition. The empirical data on latency agree very well with the power law of Equation (7). Calculations for $l = 5$ yield $\lambda_{crit} = 0.03536$, $\alpha = 1.775 \pm 0.028$, and a critical exponent $\beta = 0.2026 \pm 0.0095$.

Figure 8 shows that large fluctuations in the number of messages in the network and in the number of saturated buffers were observed using this model. The transition of the network to the saturation phase shows characteristics of the second-order phase transition, despite the fact that this transition is more abrupt than those for model 1. This is dramatically different from model 1, which has a first-order phase transition. By comparing model 2, with a buffer limit of $m = 2$, with the earlier model with a buffer limit of

$m = 1$, one can see that increasing the buffer capacity does not necessarily lead to defer the saturation point. On the contrary, the former model reaches the saturation state under a network load almost three times smaller than the latter. The explanation of this fact is that in model 2 a node can generate messages in both state 0 and 1, rather than in state 0 only, as in Section 2.1, which results in a larger effective load.

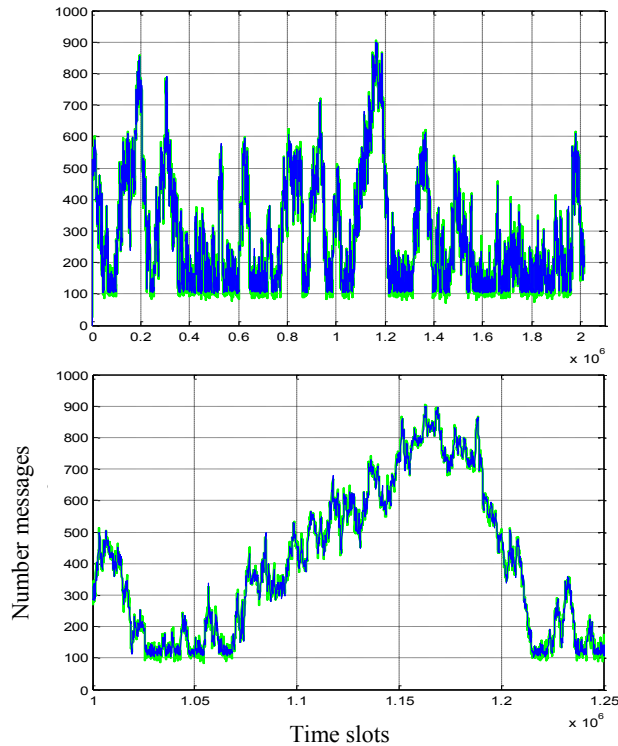


Figure 7. Inverse Average Latency, τ , as a Function of Network Load λ

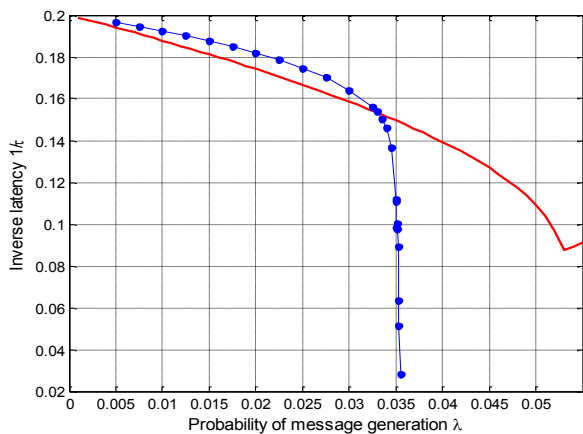


Figure 8. Number of Messages in the Network Taken at Every 100 Clock Cycles ($\lambda = 0.03535$, $l = 5$ hops)

Two-Dimensional Torus Topology

In this study, the authors considered a 16×16 toroidal square lattice network. It was assumed that messages would always be routed along the shortest path to the message destination, but static routing (no fixed path assigned to the message) was not used. When a router receives a passing message and there is a choice between two possible buffers to keep the message, one of the buffers is chosen at random. Therefore, in the case of two-dimensional torus network topology and finite buffers, the authors' choice was to make the decision, whether to send a message to a neighboring node, based not on the queue in any single buffer at the next node along the message path, but rather on the total number of messages in the neighboring router.

The limits on the total number of messages held in the router were set equal to 8 and 20. It was further assumed that the router would stop accepting incoming messages once it accumulated $(m-4)$ messages. Locally generated messages were generated individually and independently for all four directions, and once router accumulated m messages it stopped generating messages. Figures 9 and 10 show these results. The blue line with bullets shows the experimental data for router capacity equal 8 and the green line with crosses presents the experimental data for router capacity equal 20. The red line presents the theoretical prediction for networks with infinite buffers and 2-dimensional torus topology [20] given by Equations (13) and (14):

$$\bar{n} = \frac{\lambda^2(l-1)(11+5l)}{16(1-l\lambda)} + l\lambda \quad (13)$$

$$\tau = \frac{\lambda(l-1)(11+5l)}{16(1-l\lambda)} + l \quad (14)$$

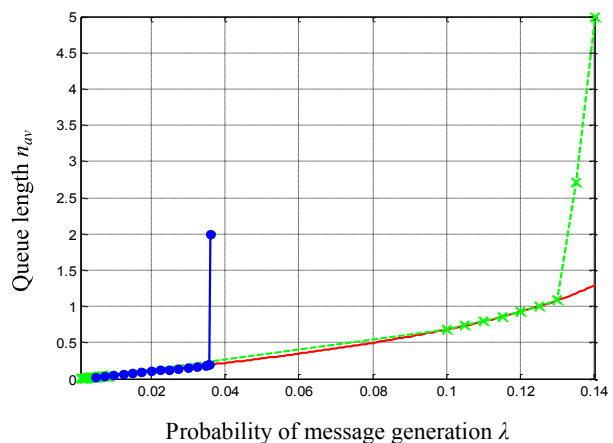


Figure 9. Queue Length, \bar{n} , as a Function of Network Load λ

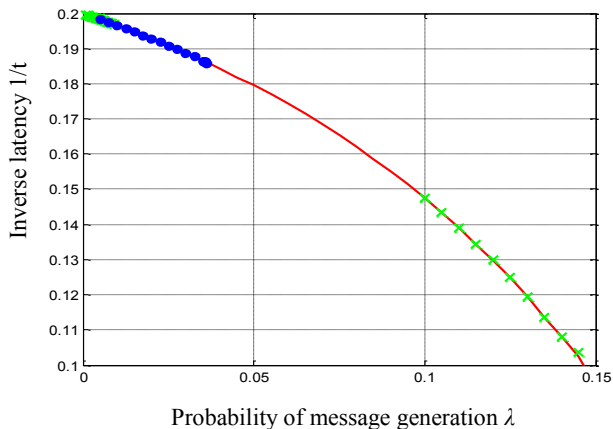


Figure 10. Latency, τ , as a Function of Network Load λ

Surprisingly, until the network load comes close to the saturation value, the network behaves as if there was no buffer limit. An excellent agreement was seen between theoretical prediction and simulation results, as well as no difference in network performance for networks with different total router capacities up to their critical loads. The simulations showed a sharp transition from the steady state regime to the saturated state for both router capacities. Therefore, in the case of torus topology and finite buffers, the network behaved as if it was undergoing a first-order phase transition.

Conclusions

In this study, the authors analyzed networks with finite buffers and proposed a few theoretical models. For small buffer sizes of $m = 1$ and $m = 2$, both first-order probability distributions (independent queue approximation) and second-order distributions (joint probabilities of pairs of neighboring nodes) were obtained. The results showed that theoretical predictions given by the second-order approximation provide a better description of network behavior compared to the first-order (mean field) approximation. But theoretical analysis, even for small values of m , proved to be very challenging, especially for the second-order approximation. Simulations data demonstrated the emergence of long-range dependences between nodes, far exceeding the “interaction radius” l when the network reached the critical region. The most interesting observation was that the network showed both first-order and second-order phase transitions. The type of the phase transition depended not only on the buffer limit, but also on the assumptions for message generation. In particular, with a buffer limit of $m = 2$, a second-order phase transition in model 1 was observed, while model 2 had a first-order transition. The second-order phase transitions

were characterized by non-trivial values of critical exponent. An interesting feature of the first-order phase transitions was that the network behavior followed the second-order approximation (for the ring topology) and “mean field” approximation for networks with infinite buffers (for the torus topology) closely until the load reached the critical value. When that happens, network goes to the saturation state abruptly. It was very difficult to predict when it would happen, even from the experimental data: there were no significant increases in the average latency or queue length right before the critical point. Only the observation of the fluctuations of the average number of messages in the network during the simulation can serve as an indication that the network is close to saturation. These fluctuations increase both in amplitude and in wavelength just before the critical point.

An interesting task for future studies would be to find out how a system with finite buffers “approximates” a system with infinite buffers (which has a second-order phase transition) with an increase in buffer size.

References

- [1] Duato, J., Yalamanchili, S., & Ni, L. M. (2003). *Interconnection Networks: An Engineering Approach*. Morgan Kaufmann, ISBN 1558608524, 9781558608528.
- [2] Kodi, A. K., Sarathy, A., & Louri, A. (2008). Adaptive Channel Buffers in On-Chip Interconnection Networks—A Power and Performance Analysis. *IEEE Trans. Comput.* 57(9), 1169-1181. DOI=<http://dx.doi.org/10.1109/TC.2008.77>
- [3] Enachescu, M., Ganjali, Y., Goel, A., McKeown, N., & Roughgarden, T. (2006). Routers with Very Small Buffers. *Proceedings of the 25th IEEE International Conference on Computer Communications*, (pp. 1-11).
- [4] Yu, G., Towsley, D., Holot, C., & Zhang, H. (2007). Congestion Control for Small Buffer High Speed Networks. *Proceedings of the 26th IEEE International Conference on Computer Communications*, (pp. 1037-1045).
- [5] Appenzeller, G., Keslassy, I., & McKeown, N. (2004). Sizing router buffers. *Proceedings of the 2004 conference on Applications, technologies, architectures, and protocols for computer communications (SIGCOMM '04)*. ACM, New York, NY, USA, (pp. 281-292).
- [6] Enachescu, M., Ganjali, Y., Goel, A., McKeown, N., & Roughgarden, T. (2005). Part III: routers with very small buffers. *SIGCOMM Comput. Commun. Rev.* 35, 3, (pp. 83-90).

- [7] Dhamdhere, A., & Dovrolis, C. (2006). Open issues in router buffer sizing. *SIGCOMM Comput. Commun. Rev.* 36, 1, (pp. 87-92). DOI=<http://dx.doi.org/10.1145/1111322.1111342>
- [8] Enachescu, M., Ganjali, Y., Goel, A., McKeown, N., & Roughgarden, T. (2006). Routers with Very Small Buffers. *Proceedings IEEE INFOCOM 2006. 25TH IEEE International Conference on Computer Communications*, Barcelona, Spain, (pp. 1-11). doi: 10.1109/INFOCOM.2006.240
- [9] Beheshti, N., Ganjali, Y., Ghobadi, M., McKeown, N., & Salmon, G. (2008). Experimental study of router buffer sizing. *Proceedings of the 8th ACM SIGCOMM conference on Internet measurement (IMC '08)*. ACM, New York, NY, USA, (pp. 197-210).
- [10] Vishwanath, A., Sivaraman, V., & Rouskas, G. N. (2011). Anomalous loss performance for mixed real-time and TCP traffic in routers with very small buffers. *IEEE/ACM Trans. Netw.* 19(4), 933-946. DOI=<http://dx.doi.org/10.1109/TNET.2010.2091721>
- [11] Hohlfeld, O., Pujol, E., Ciucu, F., Feldmann, A., & Barford, P. (2014). A QoE Perspective on Sizing Network Buffers. *Proceedings of the 2014 Conference on Internet Measurement Conference (IMC '14)*. ACM, New York, NY, USA, (pp. 333-346). DOI=<http://dx.doi.org/10.1145/2663716.2663730>
- [12] Bravi, E., & Cotter, D. (2007). Optical packet-switched interconnect based on wavelength-division-multiplexed clockwork routing. *Journal of Optical Networking*, 6(7), 840-853.
- [13] Rykalova, Y., Levitin, L. B., & Brower, R. (2008). Interconnection Networks with Heterogeneous Activity or Finite Buffers: Beyond Jackson's Theorem. *Proceedings of the 11th Communications and Networking Simulation Symposium, CNS08* (pp. 9-14). Ottawa, Canada.
- [14] Levitin, L. B., & Rykalova, Y. (2015). Computer Networks with Finite Buffers: Beyond Jackson's Theorem. In Al-Sakib Pathan, Muhammad Monowar, and Shafiullah Khan (Eds.) *Simulation Technologies in Networking and Communications: Selecting the Best Tool for the Test*. CRC Press 2015, 31 - 68. Print ISBN: 978-1-4822-2549-5 eBook ISBN: 978-1-4822-2550-1
- [15] Jackson, P. (1963). Job shop like queueing systems. *Management Sci.*, 10(1), 131-142.
- [16] Asadathorn, N., & Chao, X. (1999). A decomposition approximation for assembly- disassembly queueing networks with finite buffer and blocking. *Annals of Operations research*, 87(1), 247-261.
- [17] Barrenetxea, G., Beferull-Lozano, B., & Vetterli, M. (2005). Efficient routing with small buffers in dense networks. *Proceedings of the 4th international symposium on Information processing in sensor networks. Los Angeles, California*, (pp. 277- 284).
- [18] Mandjes, M., & Kim, J. H. (2001). Large Deviations for Small Buffers: An Insensitivity Result. *Queueing Syst. Theory Appl.* 37(4), 349-362.
- [19] Chang, S. H., & Choi, D. W. (2005). Performance analysis of a finite-buffer discrete-time queue with bulk arrival, bulk service and vacations. *Comput. Oper. Res.* 32(9), 2213-2234. DOI= <http://dx.doi.org/10.1016/j.cor.2004.01.00>
- [20] Levitin, L. B., & Rykalova, Y. (2015). Analysis and Simulation of Computer Networks with Unlimited Buffers. In Al-Sakib Pathan, Muhammad Monowar, and Shafiullah Khan (Eds.) *Simulation Technologies in Networking and Communications: Selecting the Best Tool for the Test*. CRC Press 2015, 3 -30. Print ISBN: 978-1-4822-2549-5 eBook ISBN: 978-1-4822-2550-1
- [21] Levitin, L. B., & Rykalova, Y. (2016). Latency and Phase transitions in Interconnections Networks with Unlimited Buffers. *Proceedings of the 5th IAJC/ ISAM Joint International Conference*, Orlando, FL. ISBN 978-1-60643-379-9

Biographies

LEV LEVITIN is a Distinguished Professor of Engineering Science in the Department of Electrical and Computer Engineering at Boston University. He has published over 200 papers, presentations, and patents. His research areas include information theory; quantum communication systems; physics of computation; quantum computing; quantum theory of measurements, mathematical linguistics; theory of complex systems; coding theory; theory of computer hardware testing, reliable computer networks, and bioinformatics. He is a Life Fellow of IEEE, a member of the International Academy of Informatics, and other professional societies. Professor Levitin may be reached at levitin@bu.edu

YELENA RYKALOVA is a Visiting Researcher in the Department of Electrical and Computer Engineering at Boston University and teaches at UMass Lowell. Her research interests include computer networks, in particular, in application of concepts and models of statistical physics to the analysis of network performance. She is a member of IEEE and the Society for Modeling and Simulation International (SCS). Since 2008, she has been active in organization and preparation for the Spring Simulation Multiconference (SpringSim) as technical committee member, reviewer, and publicity and session chair. Dr. Rykalova may be reached at rykalova@bu.edu

GATE DRIVE AND EFFICIENCY ANALYSIS FOR A SILICON CARBIDE MOSFET-BASED ELECTRIC MOTOR DRIVE

Todd D. Batzel, Pennsylvania State University, Altoona College;
Taylor R. Leach, Pennsylvania State University, Altoona College

Abstract

With increasing interest in vehicle electrification and renewable energy systems, the demand for improved power density and operating efficiency in energy conversion systems is intensifying. The recent widespread availability of silicon carbide (SiC) semiconductor switching components has offered the potential for significant improvements to energy conversion systems used for motor drives and inverters, and DC-to-DC converters. SiC switching devices, such as SiC MOSFETs and Schottky diodes, are particularly attractive to developers of applications requiring compact, high-efficiency energy conversion, because of their low conduction and switching losses, their ability to operate at very high temperatures, and their high-frequency switching capability, as compared to silicon-based MOSFETs and IGBTs.

Though SiC power electronic components offer great potential improvements in power conversion systems, fully realizing their benefits presents a challenge. SiC switches, due to their ultra-fast switching speeds, are susceptible to transients introduced by a rapid change in the drain-to-source voltage. Therefore, the gate drive requirements of SiC MOSFETs require a thorough analysis in order to prevent high dv/dt transients from causing erratic switching behavior or unnecessary switching loss. In addition, stray impedances can be the source of resonance during switching, which can lead to potentially destructive transient overshoots. In this paper, the authors analyze a SiC-based inverter used in motor drives. The gate drive for a half-bridge was developed, and trade-offs involving the optimization of power conversion efficiency within the operating condition limitations of the switching devices were analyzed by simulation. Switching and conduction losses were computed for the system and efficiency was determined. Finally, the overall impact of PWM switching frequency on the conversion efficiency was assessed.

Introduction

The power electronic switches used in commercial electric motor drives have, over the past several decades, been

implemented using silicon-based semiconductor technologies, with CMOS and IGBT devices dominating low-voltage and high-voltage applications, respectively [1]. The development and recent commercialization of silicon carbide (SiC) semiconductors has offered opportunities for significant improvements to electric motor drive systems, and there is a keen interest in integrating SiC-based power switches into electric drives [2]. Though it is not yet a mature technology, SiC power switches promise to play an increasing role as power switches used for motor drives in electric propulsion applications [3]. The advantages of SiC over Si-based semiconductors in power switching applications is mainly due to the lower on-state resistance and faster switching characteristics of SiC that can contribute to lower power losses in the switch itself [4]. SiC devices also have lower parasitic capacitances [5], operate at higher junction temperatures, and are easily paralleled for higher current applications [6]. These characteristics, if fully exploited, promise to improve the efficiency and power density of power conversion systems.

Several SiC electric motor drives for electric vehicle applications have already been developed and demonstrated. Maswood et al. [7] compared the efficiency of 3-phase inverters using SiC JFETs through simulation with an IGBT-based design in the output power range from 13 kW to 22 kW. The results showed increasing efficiency improvements associated with the SiC design, as the PWM frequency increased. Implementations of SiC-based motor drives with output capabilities ranging from 11 kW up to 312 kVA were demonstrated in a number of studies [6, 8-9]. Testing of these implementations confirmed the benefits of using SiC power switches. In the work by Novak et al. [10], the authors discussed the importance of the gate-drive circuit design and consideration of parasitics in fully realizing the potential benefits of SiC power switches. The purpose of this current study was to develop and simulate the power electronics for a 12 kVA SiC MOSFET-based half bridge that could be applied, for example, to an electric propulsion system. Performance of a 12-kVA half-bridge (1/3 of a 36-kVA three-phase inverter) was analyzed through component-level simulation. The gate drive for the SiC power switches was analyzed and the switching behavior was optimized for minimal switching loss, within the constraints of

the device's absolute maximum ratings. Overall conversion efficiency was characterized for various PWM switching frequencies, and opportunities for improved power density of the system were also considered.

Half-Bridge Converter

Figure 1 shows a half-bridge converter, which is the basic building block for electric motor drives. Three of these paralleled half-bridge circuits sharing a common DC voltage source can be used to form a three-phase inverter that is capable of driving the motors used in electric propulsion applications such as induction, synchronous reluctance, and permanent magnet synchronous machines.

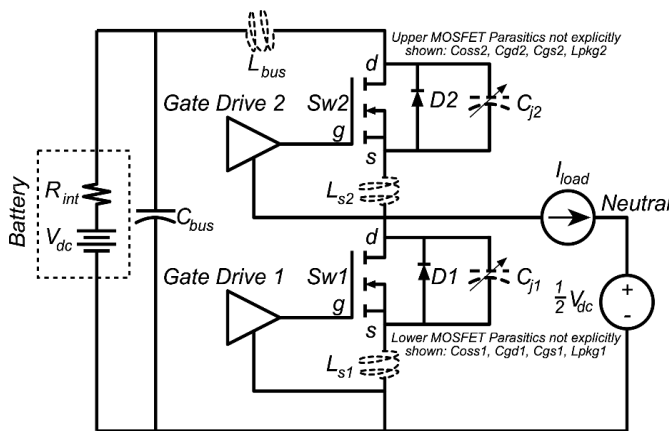


Figure 1. Half-Bridge with Parasitics Shown in Dashed Lines

The electronic switches, SiC MOSFETs Sw1 and Sw2 in this case, are used to connect the DC source to the load. In the application of interest, the DC source is a battery with internal resistance R_{int} . The load in the application is a three-phase permanent magnet synchronous motor. Thus, the load is inductive and, for purposes of analysis, it can be considered to have a constant current, since the PWM switching period of the half-bridge is normally much shorter than the time constant of the motor phase winding. A gate driver, discussed later, is required for each switch. Freewheeling diodes D1 and D2 are required to provide load current paths from the source to the drain.

Turning on a SiC switch involves applying a gate-to-source voltage exceeding the threshold of the device. Conversely, to turn off the switch, the gate driver applies a gate-to-source voltage well below the threshold. In the half-bridge, only one of the two switches can be turned on at a time. Otherwise, damaging shoot-through current will flow from the DC source through the two switches, limited only by the source resistance and the on-resistance of the switches. For positive load current (Figure 1), when Sw2 is turned

on (in which case, Sw1 must be off), the current flow is from the DC source through Sw2 to the load. Conversely, when switch 1 is on (and Sw2 is off), the load current flows through freewheeling diode D1 of the lower switch. Negative load current (opposite direction from the current in Figure 1) reverses the roles of switches Sw1 and Sw2. With Sw1 on, the load current flows through the lower MOSFET; otherwise, load current will be through freewheeling diode D2 of the upper switch. In a motor drive application, the applied phase-to-neutral voltage is controlled by the duty cycle D of the switches through a PWM signal supplied by the controlling processor. The average phase-to-neutral voltage applied to the motor by the half-bridge is given by Equation (1).

$$V_{load} = V_{dc} \left(D - \frac{1}{2} \right) \quad (1)$$

Figure 1 shows the second-order switching effects of the half-bridge—assuming a positive load current—due to the parasitics shown as dashed lines. If the inverter is initially in a state such that both switches are off, the lower flyback diode, D1, is conducting the full load current, and the inductive load current is decaying. The upper switch, Sw2, is operating at zero current, and the full DC bus voltage, V_{dc} , is across its drain-to-source connection. Figure 2 shows the output characteristics corresponding to the point labeled A in the SiC MOSFET; Figure 3 shows the actual switching waveforms. If the gate driver then turns the upper switch on, the gate-to-source voltage, V_{gs} , rises but V_{ds} of Sw2 is clamped, due to the lower diode, D1, conducting. As V_{gs} rises, the SiC MOSFET acts as a voltage-controlled current source, and the switch begins to conduct current I_d . In Figure 2, this corresponds to movement from point A to point B. When the drain current, I_d , is equal to the load current, the lower diode can turn off and V_{ds} of Sw2 is no longer clamped. Figures 2 and 3 show how the operating point moves horizontally from point B to C. At point C, the device is turned on and operates in the ohmic region. At point C, the on-resistance of the switch is rather low, and the product of the drain-to-source voltage and the drain current is conduction loss. These two figures also show that a higher gate-to-source voltage, V_{gs} , will yield lower conduction loss, since they reduce the drain-to-source voltage.

A description of the upper switch turn-off for a positive load current is quite similar. Initially, the upper switch, Sw2, is in the on state, corresponding to operating point C in Figures 2 and 3. When the gate driver lowers the gate-to-source voltage for turn-off, the drain current is clamped, due to the inductive load current. Thus, the operating point moves horizontally from C towards B in Figure 2, corresponding to an increasing V_{ds} . When operating point B is reached, the lower diode, D1, is able to begin conducting

load current so that the Sw2 current, I_d , can begin to decrease. The upper-switch V_{ds} is now clamped by the lower diode, and the operating point moves from B towards A, as the lower diode assumes more of the load current. At point A, the diode carries the full load current and the upper switch is in the off state with the DC bus voltage across its drain and source.

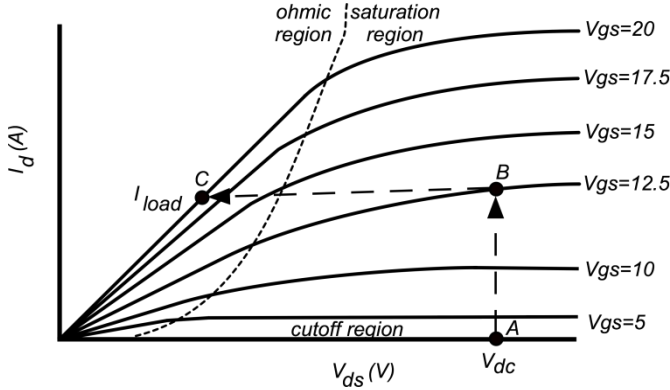


Figure 2. Power Switch Output Characteristics

As indicated earlier, when the upper switch is in the on-state (point C), there is a conduction energy loss that is dependent on the drain-to-source voltage in the on-state, $V_{ds,on}$, the drain current, and the duty cycle, D , of the upper switch. This is given by Equation (2):

$$P_{con} = V_{ds,on} I_d D \quad (2)$$

Likewise, during each PWM cycle, the MOSFET is turned on and off, resulting in a corresponding switching energy loss, E_{sw} . This switching loss can be determined by the path of the operating point in Figure 2 and the corresponding switching transition times (the turn-on and turn-off times), as explained via Equation (3):

$$E_{sw} = \int_{turnon} V_{ds}(t) I_d(t) dt + \int_{turnoff} V_{ds}(t) I_d(t) dt \quad (3)$$

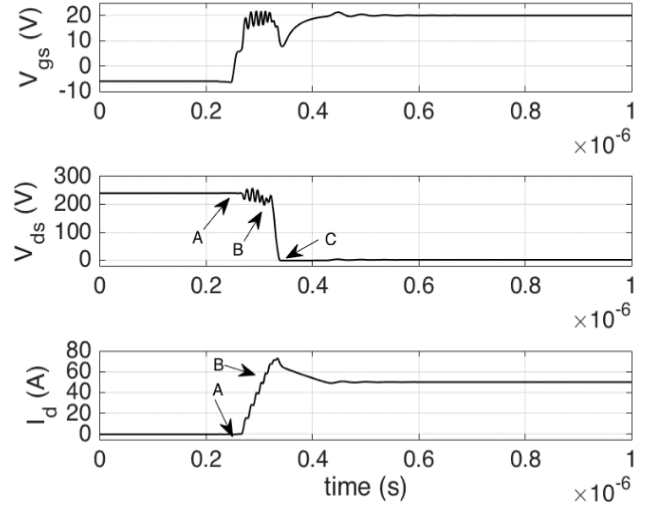
The power loss, due to switching, P_{sw} , depends on the PWM switching frequency, f_{sw} , as determined by Equation (4):

$$P_{sw} = E_{sw} f_{sw} \quad (4)$$

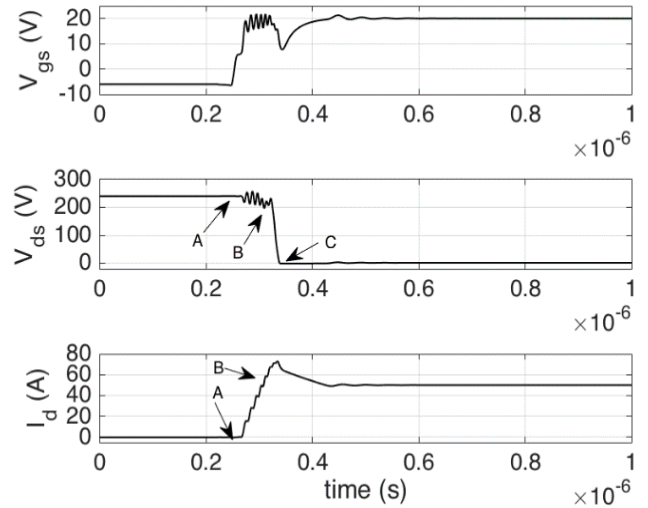
Parasitics and Resonance in SiC MOSFETs

In the absence of a soft-switching scheme [11], these switching losses are unavoidable, but steps can be taken to minimize them. Figure 1, showing the half-bridge circuit,

includes several parasitic impedances, indicated by the dashed lines. The connection of the DC bus has an associated inductance, L_{bus} . Likewise, the connection between the gate driver and the source connection of the SiC MOSFET packages has associated inductances of L_{s1} and L_{s2} for the lower and upper switches, respectively. The flyback diode model of Figure 4 includes nonlinear junction capacitances, C_{j1} and C_{j2} for the lower and upper diodes, respectively. When the flyback diodes are forward biased, the junction capacitance is essentially short-circuited.



(a) At Turn-On



(b) At Turn-Off with Gate Resistors of 5Ω

Figure 3. Waveforms for the Upper Switch

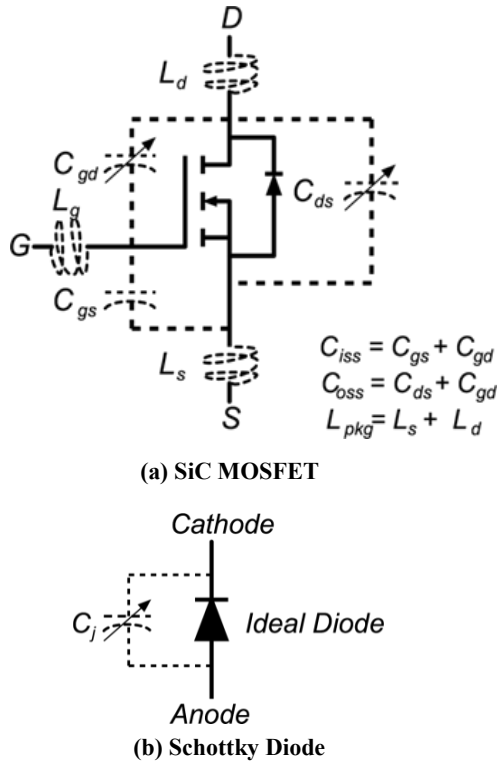


Figure 4. Circuit Models including Parasitics

In addition to the half-bridge parasitics in Figure 1, the SiC MOSFET also has parasitic impedances that must be considered for high device switching speeds. Figure 4 shows the SiC MOSFET model, which includes a gate-to-source capacitance, C_{gs} , gate-to-drain capacitance, C_{gd} , and a drain-to-source capacitance, C_{ds} . Most datasheets specify total effective output capacitance, C_{oss} , and effective input capacitance, C_{iss} . Figure 4(a) shows how these effective values can be determined. Some of these parasitic capacitances depend on the drain-to-source voltage, with the highest capacitance occurring at a low drain-to-source voltage, V_{ds} .

The parasitics play an important role in the switching of SiC devices. One mode is when the parasitics form a resonant circuit in the power circuit that, during switching transients, can cause overshoots and ringing in the output voltage and current of the device. Another mode is the Miller Effect [12], where the gate-to-drain capacitance forms a feedback loop such that a changing drain-to-source voltage can cause a plateau in the applied gate-to-source voltage or, in more severe cases, can cause unintended turn-on or turn-off of the switch. Yet another consideration is the formation of a resonant circuit in the gate drive circuit and the interaction of the gate driver output impedance with the gate parasitic components.

To illustrate these parasitic effects, simulations were performed on the half-bridge circuit. Figure 3 shows how the switching waveforms use a 125 MHz ringing at turn-on of the signals V_{ds} and I_d during the transition from operating point A to B of Figure 3(a). This ringing is the result of the resonant circuit formed by the various parasitic components of the half-bridge at that operating condition. The parasitics in play are L_{bus} , C_{j2} , C_{oss2} , and L_{pkg2} . The lower half of the bridge is not critical for this state, since the flyback diode, D1, is forward-biased and the parasitics associated with the lower switch are short-circuited. Equation (5) shows the resonant frequency for a circuit composed of the upper switch parasitics, upper flyback diode and its parasitics, as well as the DC voltage bus and its parasitic inductance.

$$f_{res} = \frac{1}{2\pi} \sqrt{\frac{\alpha + \beta \pm \sqrt{\alpha - \beta}}{\beta}} \quad (5)$$

where,

$$\alpha = C_{oss2}^2 (L_{pkg2} + L_{bus})^2 + L_{bus}^2 C_{j2} (C_{j2} + 2C_{oss2})$$

$$\beta = 2C_{oss2} C_{j2} L_{bus} L_{pkg2}$$

From the SiC MOSFET (Cree C2M0025120D) datasheets, $C_{oss2} = C_{j2} = 300$ pf at a reverse bias voltage of 240V. The stray inductances used were $L_{pkg2} = 15$ nH and $L_{bus} = 10$ nH. Using these component values in Equation (5), the expected resonant frequency is 130 MHz, which agrees well with the 125 MHz resonant frequency in Figure 3. After the lower diode turns off—between 0.4 and 0.5 μ s in Figure 3(a)—the simulation shows a more subtle resonance at about 23 MHz. At this operating point, the parasitics associated with the lower switch will now affect the circuit, and the resonance is now due to the components L_{bus} , L_{pkg1} , C_{j1} , C_{j2} , C_{oss1} , and L_{pkg2} . The on state of the upper switch in this state makes the output capacitance, C_{oss2} , a non-contributor to the resonant circuit. A compact expression for the resonant frequency, similar to Equation (5) as a function of these components, is not forthright, so the total impedance of the components contributing to the resonant circuit is plotted versus frequency in Figure 5 using $C_{j2} = 2500$ pf (from Schottky diode data sheet—Cree CPW51200Z050B), $C_{j1} = C_{oss1} = 300$ pf, and the same inductance values as noted previously. Note that there are several resonant frequencies associated with this circuit, the lowest of which is 23.1 MHz (145×10^6 r/s). This agrees well with the 23 MHz observed in Figure 3(a).

The ringing and overshoot during switching is undesirable for several reasons. It can stress or damage components, and can be a contributor to radiated EMI [13]. Since it is not practical to insert resistance in the power circuit to overdamp the resonant circuit, other approaches must be

considered. The addition of an external gate resistance can be used to slow the turn-on and turn-off times and, therefore, reduce the ringing and overshoot. This approach represents a trade-off between managing the overshoot and sacrificing some of the fast switching capability (and switching power loss) of the SiC device.

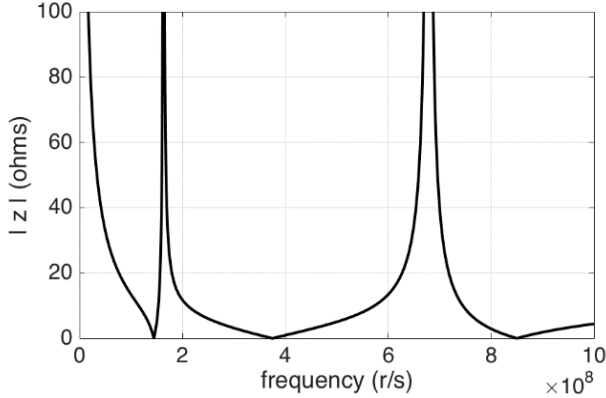


Figure 5. Half-Bridge Circuit Impedance with the Upper Switch in the On State

The other important characteristic of the switching waveforms in Figure 3 is the sudden dip in the gate-to-source voltage, V_{gs} , during the upper switch turn-on [at about $0.33 \mu\text{s}$ in Figure 3(a)] and the rise in V_{gs} during the turn-off [at about $0.15 \mu\text{s}$ in Figure 3(b)]. Both of these deviations in the gate drive voltage during switching are due to the Miller Effect, where the gate-to-drain capacitance, C_{gd} , carries a current that charges or discharges the gate as V_{ds} changes. Furthermore, any change in the drain current, I_d , will result in a voltage across the stray source inductance (L_{s1} or L_{s2} , as in Figure 1) that leads to a change in the effective V_{gs} . One way to reduce the Miller Effect coupling is to keep the output impedance of the gate driver low with high pulse current capability.

Figure 3 shows that V_{ds} drops to about 7V during turn-on [Figure 3(a)], and rises to +1.5V after turn-off [Figure 3(b)]. Although the drop to 7V is not enough to turn off the switch (the gate-to-source threshold voltage is approximately 2.5V), it will increase the on-resistance and contribute to increased switching loss. The rise to +1.5V after turn-off could potentially turn the switch back to the on state, since it is very close to the threshold, which is temperature dependent. If not addressed, these effects can lead to instability or unwanted, sporadic switching of the device [14].

Gate Drive Design

The overall function of the gate driver is to supply the current required to rapidly charge and discharge the effec-

tive gate input capacitance, C_{iss} , to the required voltage level during turn-on and turn-off of the power switch and to maintain the on- or off-state voltage levels during the switching transitions. It is typically recommended that SiC MOSFETs operate with a gate-to-source voltage of +20V for the on state and -5V for the off state. Electrical isolation and level shifting are other functions of the gate driver. Several SiC MOSFET characteristics require extra attention when designing the gate drive, as compared to the needs of silicon-based power switch gate drivers (e.g., IGBT and Si MOSFET). The gate drive issues discussed in this section include the selection of gate-drive voltage levels and drive current, the rise- and fall-time limiting of the gate drive signal to mitigate ringing and overshoots, and the gate driver impedance selection to alleviate the effects of crosstalk and the Miller capacitance—both of which can cause unintended switching or destructive voltage spikes in the half-bridge. Each of these issues will place constraints on the gate driver design and the solution will address these constraints, while minimizing switching and conduction loss. Gate driver implementation with the half-bridge was then simulated using LTSPICE to analyze the design.

The relatively low transconductance ($g_m = \Delta I_d / \Delta V_{gs}$) of the SiC MOSFET requires a rather large voltage swing of V_{gs} in order to optimize performance. Referring to the output characteristic of a typical SiC MOSFET in Figure 2, it is clear that large gate-to-source voltages, V_{gs} , yield the lowest on-state resistance that is necessary to minimize conduction losses. The switch is considered to be fully on when V_{gs} reaches about 17V, and the lowest on-state resistance corresponds to a V_{gs} of 20V. No appreciable reduction in the on-resistance is achieved by raising V_{gs} above 20V. A typical SiC MOSFET begins to conduct at a minimum gate-to-source voltage threshold, V_{th} , of approximately 2.5V, so V_{gs} should be well below that threshold to assure that the switch operates in, and stays in, the off state. Therefore, it is often recommended to use a turn-on voltage V_{gs} of +20V and turn-off voltage of -5V for the SiC MOSFET. It should also be noted that the safe gate-to-source voltage range for the SiC MOSFET is between -10V and +25V, so any noise on V_{gs} that exceeds 5V can be potentially destructive if -5V and +20V are used at the gate-to-source levels.

To realize the fast switching capability of the SiC device and minimize the switching loss, the gate driver must be capable of sourcing and sinking a high peak current that is needed to quickly charge and discharge the gate capacitance to the required on- and off-state voltages. For the SiC MOSFET used in this study, the total gate capacitance, C_{iss} , was specified as 2800 pf (or a bit higher when V_{gs} approaches zero) so that charging and discharging the gate in 10 ns required a gate drive/sink current, as expressed by Equation (7):

$$i_{gate} = \frac{C_{iss} \Delta V_{gs}}{\Delta t_{gc}} \quad (7)$$

where, ΔV_{gs} is the total gate-to-source voltage swing of 25V and Δt_{gc} is the desired gate charge time of 10 ns.

This yields a required gate current of 7A and is implemented with a complementary N- and P-channel MOSFET pair (Si7465DP and Si7884DP) as Figure 6 shows, which also shows the connection to a half-bridge circuit. The gate drive MOSFETs M1 and M2 discharge and charge, respectively, the gate of the lower SiC MOSFET. Likewise, M3 and M4 discharge and charge the gate of the upper SiC MOSFET in the half-bridge. The turn-on and turn-off voltage levels are provided by +20V and -5V isolated DC-to-DC converters that must be referenced to the SiC MOSFET source connection. As discussed in a previous section, the fast switching transitions that the SiC MOSFET is capable of make it necessary to carefully manage the gate driver design, otherwise significant ringing and overshoot can result. One method to reduce this effect is to add an external gate resistance to the gate charge and discharge current paths. Figure 6 shows that R1 and R2 are the added gate resistance for the turn-off and turn-on of the lower SiC MOSFET. R3 and R4 are the added gate resistors for the upper SiC MOSFET driver. Separate resistances are used to better manage the turn-on ($R_{g,on} = R2$ and R4) and turn-off ($R_{g,off} = R1$ and R3) of the switch.

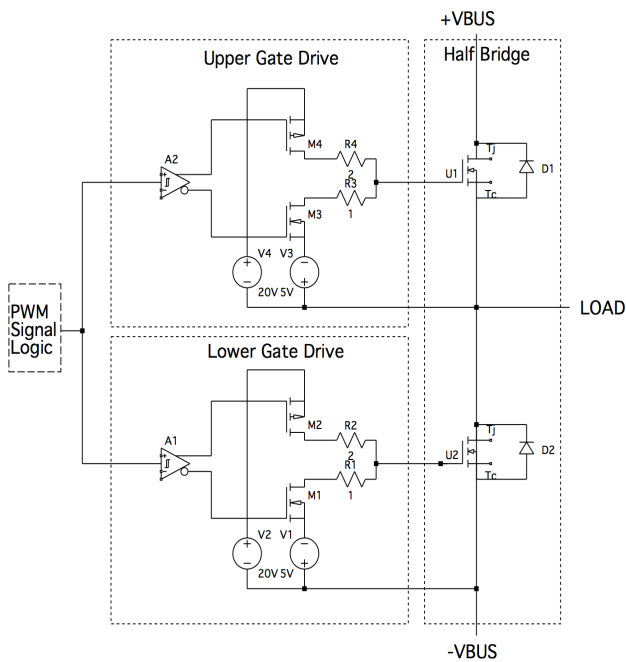
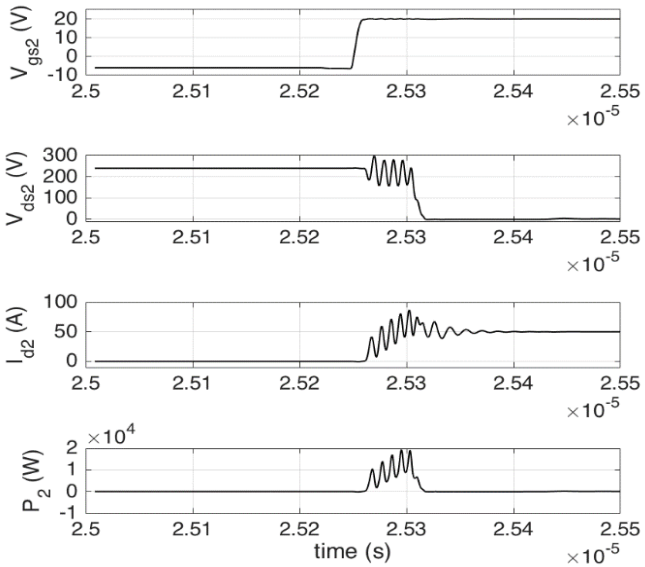


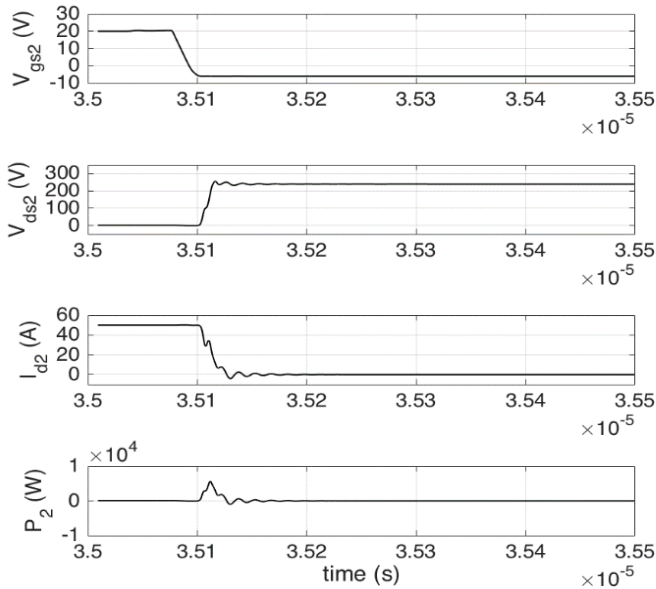
Figure 6. Gate Drive and SiC MOSFET Half-Bridge

To demonstrate the effect of external gate resistance, consider the simulation shown in Figure 7, where no added gate resistance is used. With no added gate resistance, the upper switch drain current, I_{d2} , goes from its initial value to final value of 50A in approximately 30 ns. However, during turn on, there is an ac component on the drain current due to resonance, whose peak-to-peak amplitude is nearly 50A. Similarly, the drain-to-source voltage of the upper switch, V_{ds2} , has a peak-to-peak ripple of 150V. The resultant current overshoot is 40A. This level of overshoot and ringing is unacceptable, as it stresses components and leads to increased EMI emissions. Figure 7 shows that the total switching loss energy for the upper switch (where the fly-back diode is considered to be part of the switch) was obtained by integrating the instantaneous switch power, P_2 , over the switching time interval, and found to be 410 μ J for turn-on, and 62 μ J for turn-off, for a total switching loss of 472 μ J per switching cycle. Note that the overshoots and ringing are not as prominent during turn-off of the upper switch because the gate drive signal has a gentler slope. This difference in slope is largely due to the gate capacitance being a function of V_{ds} , with the capacitance being significantly higher for a low value of V_{ds} . This shows that slowing down the gate drive V_{gs} is useful for overshoot mitigation.

To analyze the effect of increasing the gate resistance, the extra gate resistors (R1-R4 of Figure 6) are set to 10 Ω . Figure 8 shows the simulated switching waveforms. As expected, the gate drive voltage, V_{gs} , switching transition is much slower than was the case with no added gate resistance. The result is significantly less ringing and overshoot in the drain current of the upper switch, I_{d2} , and its corresponding drain-to-source voltage, V_{ds2} . This improvement in ringing obtained by adding external gate resistance, however, comes at considerable expense. The total switching energy for the upper switch, P_2 (the flyback diode is part of the switch), obtained from the instantaneous power dissipation in Figure 8 is 631 μ J for turn on and 164 μ J for turn off, for a total switching loss of 795 μ J per switching cycle. Thus, the switching loss increased significantly (68%) by the addition of the 10 Ω gate resistors. In addition to the increase in switching loss due the added gate resistance, there are now prominent deviations in the gate voltage, V_{gs} . Figure 8(a), for example, shows that during turn on, the gate voltage dips by 2V, which is very close to the threshold voltage, V_{th} , of the device and, therefore, must be addressed. This sudden drop in the gate voltage could lead to unintentional turn-off at worst, or at least unnecessary switching loss, since the on-state resistance is inversely proportional to the gate voltage. The cause of this drop in gate voltage is the sudden decrease in the drain voltage, which diverts current from the gate to the drain through the Miller capacitance, C_{gd} .



(a) Upper Switch Turn-On

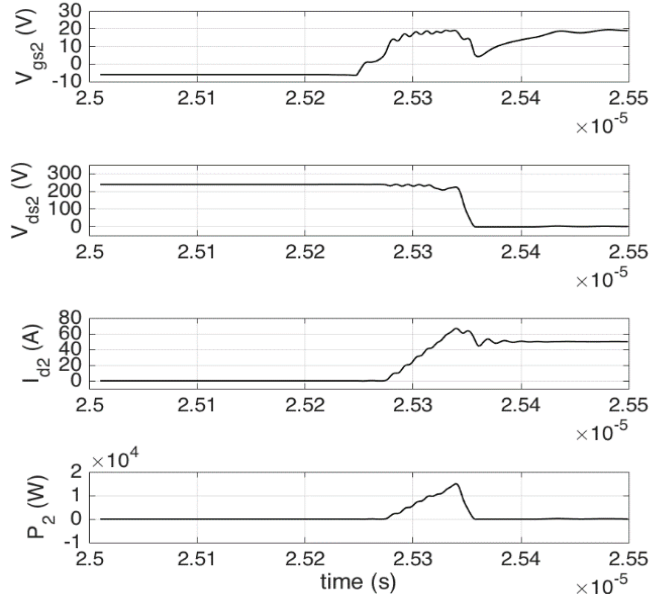


(b) Upper Switch Turn-Off

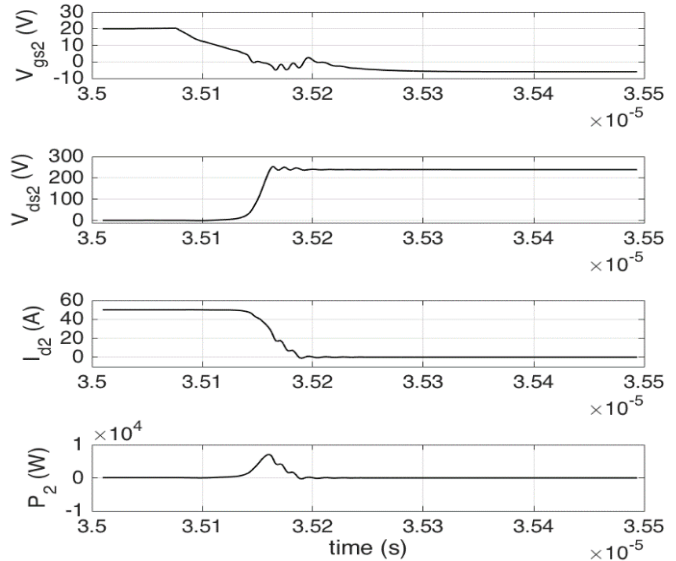
Figure 7. Upper Half-Bridge Switching Waveforms Showing a Positive Load Current and 0Ω in Gate Drive

This current was also present in the case where no external gate resistance was added, but the effect was not prominent, due to the low-impedance of the gate driver. With the added 10Ω in the gate drive, the currents in the parasitic Miller capacitance can lead to significant gate voltage drops, as in Figure 8(a). Another contributor to the drop in gate voltage is the sudden change in the upper switch drain

current, I_{d2} . This causes a change in the voltage across the stray source inductance, L_{s2} , which couples even more current into the gate via the gate-to-source capacitance, C_{gs} . These two phenomena are responsible for the significant drop in gate voltage in Figure 8(a), at approximately 2.535×10^{-5} seconds.



(a) Upper Switch Turn-On



(b) Upper Switch Turn-Off

Figure 8. Upper Half-Bridge Switching Waveforms with 10Ω in Gate Drive

A similar situation arises during the turn-off of the upper switch, as in Figure 8(b). During turn-off, the gate voltage increases from its desired value of -5V to +2.5V. This is very close to the gate threshold voltage and, therefore, could potentially turn the switch back on. The rise in gate voltage is due to the resonance in the circuit, a change of current in the stray source inductance, and the Miller coupling. Note, however, that parasitic coupling is not as severe as turn on, since the applied V_{gs} has a lower slope for turn off.

Figure 9 shows what happens at the lower switch at the same time that the upper switch turn-on and turn-off waveforms from Figure 8 occur. For the positive load current used in the test, the lower half-bridge is self-commutating, since the flyback diode is carrying the load current. In Figure 9, note that spikes in V_{gs} correspond to the upper switch transitions from Figure 8. This is the crossover effect, where switching in the upper half-bridge influences the lower half-bridge signals and vice versa. In Figure 9(a), the gate signal of the lower SiC MOSFET switch is driven low, but since the flyback diode is carrying the positive load current, the gate signal has no effect on the state of the switch. Shortly after the lower switch gate is driven low, the upper switch gate is driven high (see Figure 8). When the upper switch in the half-bridge starts to turn on, V_{ds} of the lower switch increases rapidly so that a current is driven from the drain to the gate through C_{gd} . This current must go through the gate resistor, $R_{g,off}$, and the gate driver impedance into the -5V source. This causes a rise in V_{gs} to +4V, as in Figure 9(a) that starts to drive the lower switch mildly into the conducting state and initiates some unstable switching behavior. Due to resonance, the gate-to-source voltage, V_{gs} , of the lower switch reaches levels of -20V during this resonance at about 2.53×10^{-5} seconds. This is well below the maximum negative gate-to-source voltage of -10V and could damage the SiC MOSFET.

Figure 9(b) also shows the crossover effect. In this case, the upper SiC MOSFET is turned off at about 3.515×10^{-5} seconds, which causes a drop in V_{ds} across the lower switch so that a current flows from the lower switch gate to drain through C_{gd} . This current flows through the external gate resistance, $R_{g,off}$, so that the gate voltage, V_{gs} , drops below -5V. The crossover coupling is not as pronounced in Figure 9(b) since dv/dt of the drain-to-source voltage is comparatively low. Regardless, it is clear that the selection of the gate resistance is important in reducing the effects of crosstalk as well as overshoots and ringing.

Gate Drive Resistance Selection

Using no additional external gate resistance gives the fastest possible switching transitions and, thus, very low

switching losses. However, as in Figure 7, the very fast switching can also yield excessive ringing and overshoot. Adding external gate resistance can be added to slow down the switching and can mitigate the overshoot, but this increases the switching loss and the added gate drive impedance can lead to stability issues or operation of the SiC MOSFET outside of its rated V_{gs} operating range of -10V to +25V. The choice of gate drive resistors, therefore, represents an engineering tradeoff and requires careful assessment.

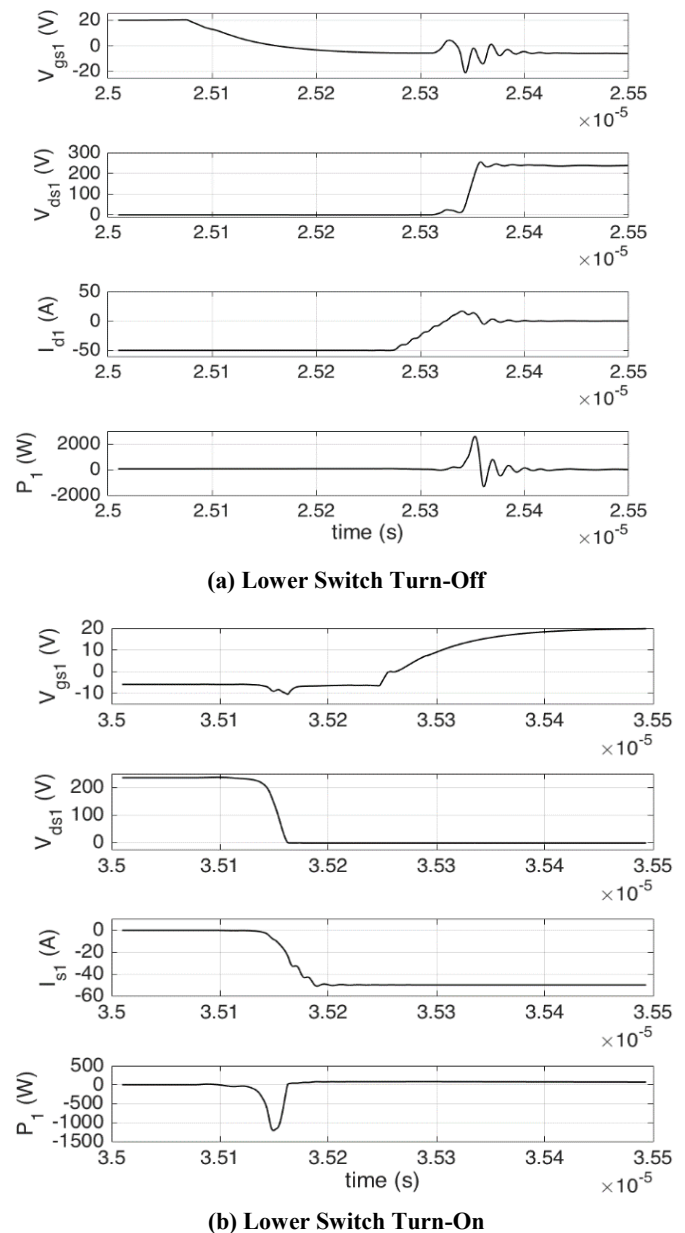


Figure 9. Lower Half-Bridge Switching Waveforms with 10Ω in Gate Drive

Component-level circuit simulations were performed using LTSPICE for various combinations of gate resistance, and the switching losses were computed. Figure 10 summarizes the results, which confirm that switching losses increase with external gate resistance. Specifically, the addition of gate resistance $R_{g,on}$ increases the turn-on switching loss, while adding $R_{g,off}$ increases turn-off switching loss. Figure 11 shows the total switching loss per switching cycle, as a function of the selected gate resistance.

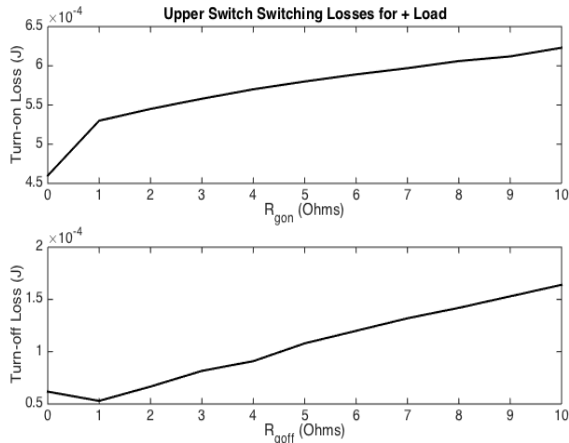


Figure 10. Turn-On and Turn-Off Loss versus External Gate Resistance

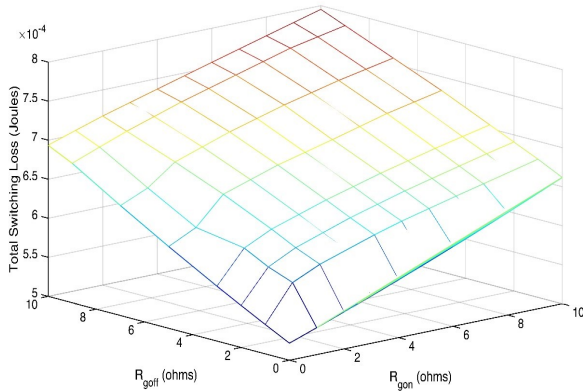


Figure 11. Total Switching Loss per Cycle for Various External Gate Resistor Values

The simulation results were also analyzed to see the correspondence between gate resistance values and the V_{gs} excursions that may violate device ratings. The simulations reveal that, for positive load current, higher $R_{g,on}$ leads to more severe dips in the upper switch V_{gs} during turn-on, while larger $R_{g,off}$ tends to create higher surges in upper switch V_{gs} , while the device is being driven off. Due to crosstalk, the lower switch deviations for positive load current depend largely on the slope of the upper switch V_{ds} . A

negative load current reverses the roles. That is, the lower switch gate resistances determine deviations in the lower switch V_{gs} , while the upper switch V_{gs} deviations are due to crosstalk from the lower gate transitions. In general, the results showed that any combination of $R_{g,on} \leq 2\Omega$ and $R_{g,off} \leq 1\Omega$ led to gate-to-source voltages that were safely within device ratings, with no danger of inadvertent turn-on or turn-off of the device. Based on this analysis, the values of $R_{g,on} = 2\Omega$ and $R_{g,off} = 1\Omega$ were selected as a compromise between minimizing switching loss, maintaining the device within its safe operating range, and avoiding excessive overshoots and ringing. Figures 12 and 13 show the switching transitions of the upper and lower switches, respectively, for this selection of gate resistance.

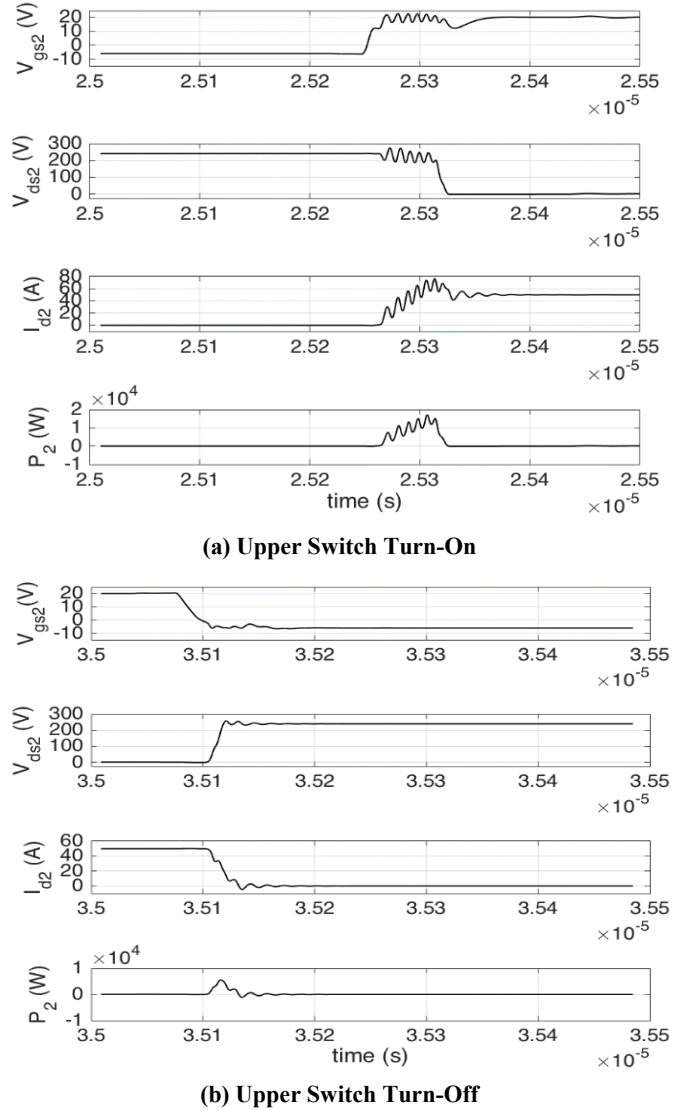
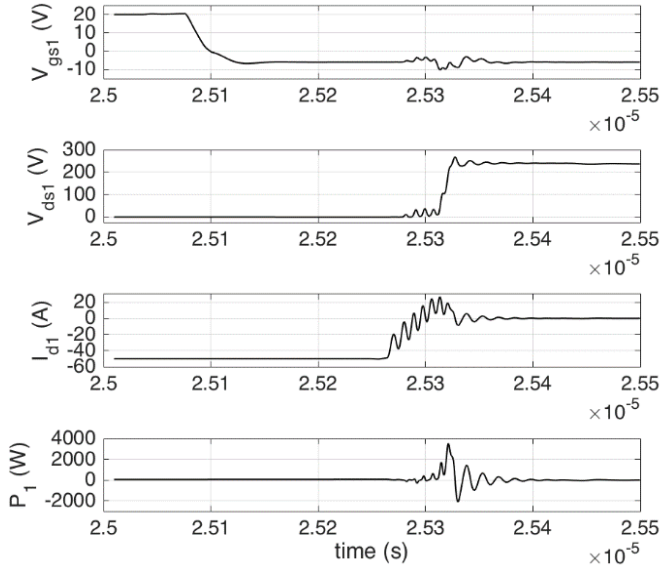
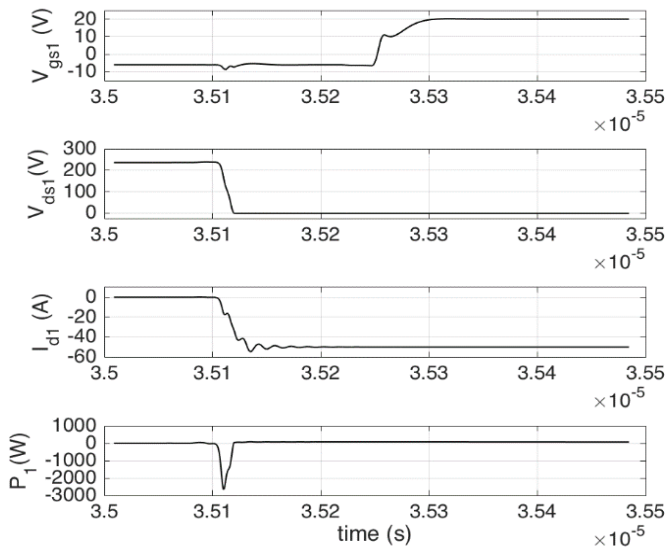


Figure 12. Upper Switching Transitions for $R_{g,on} = 2\Omega$ and $R_{g,off} = 1\Omega$



(a) Lower Switch Turn-Off



(b) Lower Switch Turn-On

Figure 13. Lower Switching Transitions for $R_{g,on} = 2\Omega$ and $R_{g,off} = 1\Omega$

Analysis of Switching and Conduction Losses in the Half-Bridge

Using the selected gate-resistor combinations from the previous section, the switching and conduction losses are now analyzed for a range of load current up to 50A, the rated maximum continuous current for the SiC MOSFET used in the study. The simulations assume operation at a case temperature of 25° C. Table 1 presents compiled results.

Table 1. Switching Loss for Positive Load Current

	$I_{load} = 50\text{ A}$	$I_{load} = 40\text{ A}$	$I_{load} = 30\text{ A}$	$I_{load} = 20\text{ A}$	$I_{load} = 10\text{ A}$
Upper turn-on	547 μJ	380 μJ	258 μJ	150 μJ	76.2 μJ
Lower turn-off	23.7 μJ	25.4 μJ	24.6 μJ	24.2 μJ	25.4 μJ
Upper turn-off	53.1 μJ	40.6 μJ	23.7 μJ	21.7 μJ	22.4 μJ
Lower turn-on	-19 μJ	-19.7 μJ	-20.5 μJ	-21.7 μJ	-22.6 μJ
Total W_{sw}	604.8 μJ	426.3 μJ	285.8 μJ	164.2 μJ	101.4 μJ

Note that the switching losses for the upper switch are approximately proportional to the load current level, as expected, while the lower switching loss is not. In addition, the results of the table can be used for negative load current as well, by translating the upper and lower switching energies. The total half-bridge switching loss for each PWM switching cycle, W_{sw} , is obtained by adding the appropriate column of losses from Table 1, and the average switching power loss, P_{sw} , is dependent on the PWM switching frequency, f_{sw} , shown in Equation (8):

$$P_{sw} = W_{sw} f_{sw} \quad (8)$$

The switch conduction energy loss for each PWM switching cycle, W_c , is determined by the voltage across the active switch, the current through the active switch, and the time of each steady-state part of the PWM cycle. For example, when load current is positive, the upper switch is active for part of the PWM cycle, and the lower flyback diode is the active component for the other part of the PWM cycle. In general, a switch will be conducting for part of the PWM cycle and a diode for the other part. The total conduction energy loss per PWM cycle can be determined using Equation (9):

$$W_c = V_{ds,on} I_d t_{on} + V_{diode} I_{diode} t_{off} \quad (9)$$

where, t_{on} and t_{off} are the time the SiC MOSFET and diode, respectively, are in steady-state conducting. The terms $V_{ds,on}$ and V_{diode} are the on-state voltage drops across the conducting SiC MOSFET and flyback diode, respectively. Their values for the devices used in the simulations are a function of current (see Table 2).

Table 2. SiC MOSFET and Flyback Diode Conducting Voltages

	$I_{load} = 50\text{ A}$	$I_{load} = 40\text{ A}$	$I_{load} = 30\text{ A}$	$I_{load} = 20\text{ A}$	$I_{load} = 10\text{ A}$
$V_{ds,on}$ (V)	1.5	1.2	0.87	0.57	0.28
V_{diode} (V)	1.12	1	0.86	0.57	0.28

The average conduction power loss is then given by Equation (10):

$$P_c = W_c f_{sw} \quad (10)$$

The length of time in the conduction on- and off-states, t_{on} and t_{off} , for any switching device can easily be determined by the PWM cycle time ($t_{sw} = 1/f_{sw}$), the total time per PWM cycle for which the switches are in transition (i.e., the times for which there are switching losses, such as shown in Figure 12, and the PWM duty cycle, D). As Figure 12 shows, for example, the upper switch is in transition for approximately 50 ns during turn-on and 50 ns during turn-off.

Efficiency of the Half-Bridge

The efficiency of the half-bridge was then analyzed over the range of load currents and for PWM switching frequencies of 20 kHz, 50 kHz, 200 kHz, and 500 kHz. Note that commercially available motor drives using silicon-based switching devices tend to use PWM switching frequencies of about 25 kHz or lower in order to keep switching losses to a minimum and achieve good efficiency. For consistency, the tests were conducted with a PWM duty cycle of 50%, the load is a constant current source equal to the load current, and the SiC MOSFET is operating with a case temperature of 25° C. The power output of the half-bridge is obtained from the output voltage (V_{ds} of the lower switch) and the load current, while the input power is the output power plus any switching and conduction losses in both the upper and lower switches. Results of the tests, as Figure 14 shows, demonstrate that efficiencies above 99% are possible at both 20 kHz and 50 kHz PWM switching frequencies. At the higher PWM switching frequency of 200 kHz, the switching losses begin to limit efficiency to 96%–97%. Finally, at 500 kHz, the achievable efficiency begins to drop significantly to below 94%, since the switching losses begin to dominate.

Conclusion

The authors presented a design of a SiC MOSFET half-bridge converter with emphasis on the effects of the gate drive on overall converter performance. The trade-offs be-

tween overshoot and ringing in the output, switching loss, and managing deviations in the gate-to-source voltage due to the Miller Effect and crosstalk were carefully considered in order to choose the gate drive components. Simulations were then performed on the half-bridge to analyze the switching and conduction losses in the converter, and to determine the conversion efficiency. The results show that efficiencies of over 99% are achievable at PWM switching frequencies of 20 kHz and 50 kHz, while 97% efficiency can be reached at 200 kHz. Efficiencies of silicon IGBT and MOSFETs can also reach 99%, but only at relatively low PWM frequencies. The advantages of SiC devices can be leveraged in one of several ways. One option is to operate the SiC converter at relatively low PWM frequencies (20 kHz or 50 kHz) to achieve higher efficiencies than silicon-based switches. Another option is to operate at high PWM frequencies (200 kHz, for example) and at efficiencies comparable to silicon switches operating at much lower PWM frequencies. The higher operating frequencies will allow the use of smaller components in the system and increase overall converter power density.

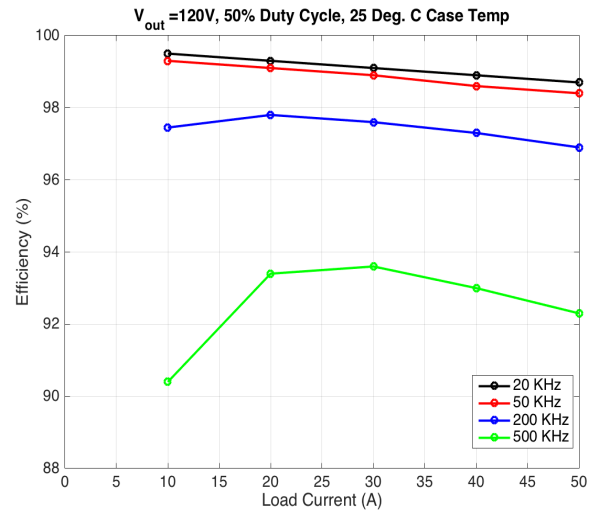


Figure 14. Half-Bridge Efficiency versus Load Current for Several PWM Frequencies

References

- [1] Vobecky, J. (2013). The current status of power semiconductors. *Electronics and Energetics*, 28(2), 193-203.
- [2] Davis, S. (2011). 1200V SiC MOSFET poised to replace Si MOSFETs and IGBTs. *Power Electronics Technology*, 36-40.
- [3] Stefanskyi, A., Starzak, L., & Napieralski, A. (2015). Silicon carbide power electronics for electric vehicles. *Proceedings of the 2015 Tenth International*

-
- Conference on Ecological Vehicles and Renewable Energies* (pp. 1-9). Monte-Carlo, Monaco.
- [4] Kondrath, N., & Kazimierzczuk, M. K. (2010). Characteristics and applications of silicon carbide power devices in power electronics. *International Journal of Electronics and Telecommunications*, 56(3), 231-236.
- [5] Ryu, S., Krishnaswami, S., Das, M., Richmond, J., Agarwal, A., Palmour, J., et al. (2004). 2 KV 4H-SiC DMOSFETS for low loss, high frequency switching applications. *International Journal of High Speed Electronics and Systems*, 14(3), 255-259.
- [6] Colmenares, J., Pefitsis, D., Rabkowski, J., Sadik, D., Tolstoy, G., & Nee, H. (2015). High-efficiency 312-kVA three-phase inverter using parallel connection of silicon carbide MOSFET power modules. *IEEE Transactions on Industrial Applications*, 51(6), 4664-4676.
- [7] Maswood, A. I., Benbrahim, L., & Harikrishnaraj, P. (2016). An investigation into the efficiency of silicon carbide based power inverters. *Proceedings of the 2016 4th International Conference on the Developments in Renewable Energy Technology* (pp. 1-6). Dhaka, Bangladesh.
- [8] Wang, G., Wang, F., Magai, G., Lei, Y., Huang, A., & Das, M. (2013). Performance comparison of 1200V 100A SiC MOSFET and 1200V 100A silicon IGBT. *Proceedings of the 2013 IEEE Energy Conversion Congress and Exposition* (pp. 3230-3234). Denver, CO.
- [9] Rabkowski, J., Pefitsis, D., & Nee, H. P. (2013). Design steps towards a 40-kVA SiC JFET inverter with natural-convection cooling and an efficiency exceeding 99.5%. *IEEE Transactions on Industrial Applications*, 49(4), 1589-1598.
- [10] Novak, M., Novak, J., & Sivkov, O. (2015). An SiC inverter for high-speed permanent magnet synchronous machines. *Proceedings of IECON2015* (pp. 2397-2402). Yokohama, Japan.
- [11] Batzel, T. D., & Adams, K. (2013). Variable timing control for ARCP voltage source inverters operating at low DC voltage. *International Journal of Modern Engineering*, 13(2), 1-8.
- [12] Lemmon, A., Mazzola, M. S., Gafford, J., & Parker, C. (2013). Stability considerations for silicon carbide field-effect transistors. *IEEE Transactions on Power Electronics*, 28(10), 4453-4459.
- [13] Han, D., & Sarlioglu, B. (2015). Study of the switching performance and EMI signature of SiC MOSFETs under the influence of parasitic inductance in an automotive DC-DC converter. *Proceedings of the 2015 IEEE Transportation Electrification Conference and Expo* (pp. 1-8). Detroit, MI.
- [14] Chen, H., & Divan, D. (2015). High-speed switching issues of high power rated silicon-carbide devices and the mitigation methods. *Proceedings of the IEEE Energy Conversion Congress and Exposition* (pp. 2254-2260). Montreal, Québec, Canada.

Biographies

TODD BATZEL received his BS and PhD degrees in electrical engineering from the Pennsylvania State University in 1984 and 2000, respectively, and MS degree in electrical engineering from the University of Pittsburgh in 1989. Currently, he is a professor of electrical engineering at Penn State University Altoona. Dr. Batzel may be reached at tdb120@psu.edu

TAYLOR LEACH is presently an undergraduate student in the BS in Electromechanical Engineering Technology (BSEMET) program at Penn State Altoona. Mr. Leach may be reached at trl5162@psu.edu

MODELING FLUID FLOW THROUGH A FLEXIBLE TUBE

Abdessamad Mehdari, Mohammed V University; Mohamed Hasnaoui, Royal Air Force School;
Mohamed Agouzoul, Mohammed V University

Abstract

In this study, the authors were interested in modeling the behavior of an instationary viscous flow in a tube with a flexible wall. This phenomenon is an interesting problem that is often encountered in industrial systems: biological, renewable energies, and, recently, in the field of transporting gaseous materials under pressure. In this paper, the authors provide a review of recent modeling with the goals of understanding the effects of the tube wall's characteristics on fluid flow. First, the Newtonian incompressible fluid was analyzed following the process of an asymptotic approach, according to a large Reynolds number and a small aspect ratio. Second, the wall was assumed to be a thin shell and generate a small axisymmetric vibration. The mathematical model for the wall was developed by using thin-shell theory. In this technique, the quadratic approach is applied to model the tube. Finally, the different parameters of the fluid and shell characteristics were studied on amplitude ratios.

Introduction

The importance of studying flow in deformable tubes is due to its occurrence in a variety of industrial systems such as biology [1], micro-fluidic devices [2, 3], renewable energies [4], and, recently, in the field of transporting gaseous materials under pressure [5]. Besides the large difficulty in analytically solving the Navier-Stokes equations, the system in this current study was characterized by three types of parameters: parameters related to the rheological behavior of the fluid [6, 7]; parameters characterized by the nature and geometry of the wall [8, 9]; and, hydrodynamic conditions [10]. In this study, the authors were interested in the symmetric and three-dimensional flow through an elastic tube with a variable radius in the presence of the force of gravity.

From another point of view, since the unicity of the solutions of the Navier-Stokes equations holds only for two-dimensional problems, it is of importance, in the three-dimensional case, to use asymptotic modeling to determine approximate solutions. In this model, there exists a small parameter, ϵ , characterizing the aspect ratio of the tube. This parameter governs the asymptotic expansion of the analysis, and the solution depends on the pressure behavior. An expansion of the solution was constructed by means of asymptotic tools, including the effects of several fundamental

physical parameters. Some examples were considered for which the application ranges of this model were estimated. The results were matched with other results obtained by means of numerical methods and experimental results.

Formulation of the Problem

The phenomenon considered in this study was caused by the interaction of the fluid with its container, the tube. The tube was assumed to be straight, long, and have circular cross sections of variable radius. It was assumed that the fluid was incompressible and Newtonian. To express the problem, the cylindrical coordinates of r' , θ' , z' (the physical variables are denoted using primes) were used. In this configuration, the length of the domain was denoted by L . Figure 1 shows how the z -axis, along the axis of the tube was chosen.

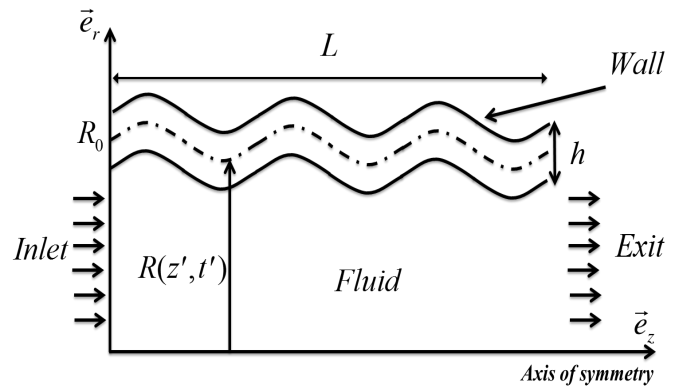


Figure 1. The Deformed Domain

The variable radius, $R(z', t')$, is a function of the longitudinal variable and time. The lateral boundary is assumed to be elastic and to deform as a result of the interaction between the fluid and the structure. Moreover, we assume that it behaves as a homogenous, isotropic, linear elastic membrane shell with thickness h .

The Fluid

The flow was instationary and axially symmetric in the presence of the force of gravity. The fluid, moving in an elastic tube, was incompressible and viscous. The motion was governed by the Navier-Stokes and the continuity equations. The scaled variables are shown in Equation (1):

$$\left\{ \begin{array}{l} r = \frac{r'}{R_0} \quad z = \frac{z'}{L} \quad t = \frac{t'}{T_{ref}} \quad \varepsilon = \frac{R_0}{L} \\ U = \frac{U_r}{\varepsilon W_0} \quad W = \frac{U_z}{W_0} \quad P = \frac{P'}{\rho_f^0 \varepsilon^2 W_0^2} \end{array} \right. \quad (1) \quad \left\{ \begin{array}{l} \tilde{U}_1 = 0 \\ \tilde{W}_1 = 0 \\ \tilde{P}_1 = 0 \end{array} \right. \quad (5)$$

where, T_{ref} is the reference time; $\varepsilon = \frac{R_0}{L}$ is the aspect ratio; W_0 is the axial velocity ρ_f^0 is the density; ν is the kinematic viscosity of fluid; P' is the pressure; and, U_r and U_z denote the components of the fluid velocity along directions r' and z' , respectively.

Using scaled variables, the non-dimensional equations of the problem are shown in Equation (2):

$$\left\{ \begin{array}{l} \left(\frac{S_t}{\varepsilon} \right) \frac{\partial U}{\partial t} + U \frac{\partial U}{\partial r} + W \frac{\partial U}{\partial z} = -\frac{\partial P}{\partial r} + \frac{\Re_e^{-1}}{\varepsilon} \left[\frac{1}{r} \frac{\partial}{\partial r} \left(r \frac{\partial U}{\partial r} \right) + \varepsilon^2 \frac{\partial^2 U}{\partial z^2} - \frac{U}{r^2} \right] \\ \left(\frac{S_t}{\varepsilon} \right) \frac{\partial W}{\partial t} + U \frac{\partial W}{\partial r} + W \frac{\partial W}{\partial z} = -\varepsilon^2 \frac{\partial P}{\partial z} + \frac{\Re_e^{-1}}{\varepsilon} \left[\frac{1}{r} \frac{\partial}{\partial r} \left(r \frac{\partial W}{\partial r} \right) + \varepsilon^2 \frac{\partial^2 W}{\partial z^2} \right] \\ \frac{\partial U}{\partial r} + \frac{U}{r} + \frac{\partial W}{\partial z} = 0 \end{array} \right. \quad (2)$$

where, $\Re_e = \frac{R_0 W_0}{\nu}$ is the Reynolds number and $S_t = \frac{R_0}{W_0 T_{ref}}$ is the Strouhal number.

For the system of this study and Equation (2), a large Reynolds number and low Strouhal number are valid under the asymptotic restriction of Equation (3), which shows the relationship between the Reynolds, the Strouhal number, and the aspect ratio of the tube:

$$\Re_e^{-1} \equiv \varepsilon \equiv S_t \quad (3)$$

Equation (3) seems to be restrictive. But, from a mathematical point of view, it characterizes a phenomenon where the initial and boundary layers originate competitive influences, and put in evidence an oscillatory phenomenon of fluid-structure system at low frequency. Linearizing Equation (2) about the particular solution at the inlet of tube yields U , W , and P , as given by Equation (4):

$$\left\{ \begin{array}{l} U = \delta_1(\varepsilon) \tilde{U}_1 \\ W = 1 + \delta_2(\varepsilon) \tilde{W}_1 \\ P = \tilde{P}_{amb} + \delta_3(\varepsilon) \tilde{P}_1 \end{array} \right. \quad (4)$$

Equation (5) shows, \tilde{U}_1 , \tilde{W}_1 , and \tilde{P}_1 the perturbed radial and axial velocities, and pressure, respectively.

where, $t = 0$, $r = 0$, and $z = 0$.

\tilde{P}_{amb} is the adimensional ambient pressure in the tube before perturbation and $\delta_i(\varepsilon)$ ($i=1, 2, 3$) are the gauge functions and are determined according to the Least Degeneration Principle, which keeps the maximum terms in Equation (2) consistent. The gauge function is defined in Equation (6):

$$\left\{ \begin{array}{l} \delta_i(\varepsilon) = \varepsilon^{\alpha_i} \\ \text{and} \\ \lim_{\varepsilon \rightarrow 0} \delta_i(\varepsilon) = 0 \end{array} \right. \quad (6)$$

where, α_i is a positive real number and found to be $\alpha_i = 3$.

Inserting Equation (6) into Equation (2), the non-degenerate adimensional equations, Equations (7)—for the 0th order ε^2 terms—and (8)—for the 1st order ε^2 terms—were obtained:

$$\left\{ \begin{array}{l} \frac{\partial \tilde{U}_1}{\partial t} + \frac{\partial \tilde{U}_1}{\partial z} = -\frac{\partial \tilde{P}_1}{\partial r} + \left[\frac{\partial^2 \tilde{U}_1}{\partial r^2} + \frac{\partial}{\partial r} \left(\frac{\tilde{U}_1}{r} \right) \right] \\ \frac{\partial \tilde{W}_1}{\partial t} + \frac{\partial \tilde{W}_1}{\partial z} = \left[\frac{\partial^2 \tilde{W}_1}{\partial r^2} + \frac{1}{r} \frac{\partial \tilde{W}_1}{\partial r} \right] \\ \frac{\partial \tilde{U}_1}{\partial r} + \frac{\tilde{U}_1}{r} + \frac{\partial \tilde{W}_1}{\partial z} = 0 \end{array} \right. \quad (7)$$

$$\left\{ \begin{array}{l} \frac{\partial^2 \tilde{U}_1}{\partial z^2} = 0 \\ \frac{\partial^2 \tilde{W}_1}{\partial z^2} - \frac{\partial \tilde{P}_1}{\partial z} = 0 \end{array} \right. \quad (8)$$

The two appropriate boundary conditions were:

1. Regularity of the solution along the z-axis, given by Equation (9):

$$\left\{ \begin{array}{l} \frac{\partial \tilde{W}_1}{\partial r} = 0 \\ \tilde{U}_1 = 0 \end{array} \right. \quad (9)$$

where, $r = 0$.

2. Kinematic condition on the contact boundary of the fluid and the structure.

In the sequel, taking into account boundary conditions and initial conditions, an expansion of the solution was constructed by means of analytical tools, including the effects of several fundamental physical parameters.

The Tube

The study of the rheological behavior of the tube requires the study of the complex relationship between the stress and strain tensors. In order to explain this relationship, the authors adopted the shell thin theory. In fact, Love [11] adopted Kirchhoff's assumptions for thin plate theory [12] and added to them the thin-shell approximation [13]. In 1970, Koiter [14] confirmed the first coherent approximation of thin shell theory presented by Love. Nevertheless, Hsu and Clifton [15] and Anliker et al. [16] were the ones who exploited Love's assumptions to study analytically the flow in an elastic pipe. These studies analyzed the behavior of blood flow in arteries. Later, in 1978 and 1986, Moddie and Haddow [17] and Bahrar [10], respectively, adopted the assumptions of that theory, which was mostly presented in three theories named: quadratic theory, linear theory, and the theory of membranes [18].

An elastic shell's behavior under the influence of external loads (forces, moments, temperature gradients, etc.) is of course governed by the theory of elasticity. Unfortunately, finding a solution to such a problem has been characterized by difficult and complex systems. The most common shell theories are those based on linear elasticity concepts. Linear shell theories adequately predict stresses and deformations for shells exhibiting small elastic deformations (i.e., deformations for which it is assumed that the equilibrium equation conditions for deformed shell surfaces are the same as if they were not deformed, and for which Hooke's law applies).

Shells of revolution, a very important class of thin shells, have many technical applications in engineering. A cylinder is generated by moving a straight line along a curve, while keeping it parallel to its original position. It follows from this definition that through every point of the cylinder, a straight line can be passed that lies entirely on this surface. These lines are called the generators. All planes that are normal to the generators intersect the cylinder in identical curves, which are called profiles. According to the Kirchhoff's assumptions, deformations throughout the entire volume of the shell material are completely defined by deformations and changes in curvature of the middle surface. Thus, the adoption of these hypotheses reduces the three-dimensional (3D) shell problem to the two-dimensional (2D) problem of equilibrium and straining of the middle surface of a shell. So, the shell will be regarded as a 2D

body (i.e., a collection of material points situated on the middle surface).

The flexible tube of length L , undeformed radius R_0 , and wall thickness h , was modeled as a cylindrical shell and its deformation is described using the geometrically non-linear Kirchhoff–Love. The Kirchhoff–Love assumption states that material lines that were normal to the undeformed mid-plane remain normal to the shell's midplane throughout its deformation and that they remain unstretched. The deformation of the shell is expressed in terms of the midplane displacements. Here, only the radial displacement was considered and is given in Equation (10):

$$\vec{A} = [R(z', t') - R_0] \vec{e}_r \quad (10)$$

The scaled variables are given in Equation (11):

$$\left\{ \begin{array}{l} \bar{R} = \frac{R}{R_0}, \bar{t} = \frac{t'}{T_{0,T}}, \varepsilon_0 = \frac{h}{R_0} \ll 1, \gamma_f^0 = \frac{\rho_f^0}{(\lambda_1 + \lambda_2)} W_0^2 \\ \bar{P}^* = \frac{P_{\text{int-tube}} - P_{\text{ext-tube}}|_{r'=R(z',t')-\frac{h}{2}}}{\rho_f^0 \cdot \varepsilon^2 W_0^2}, \gamma_T^0 = \frac{\rho_T^0}{(\lambda_2)} \left(\frac{R_0}{T_{0,T}} \right)^2 \end{array} \right. \quad (11)$$

where, λ_1 and λ_2 are the Lamé constants; $\lambda_1 = \frac{E}{2(1+\nu_T)}$ and $\lambda_2 = \frac{E\nu_T}{(1-\nu_T)}$ [E is Young's modulus and ν_T is Poisson's ratio]; ρ_T^0 and ρ_f^0 are the density of the tube and fluid, respectively; and $T_{0,T}$ is the characteristic time of the tube.

Thus, the non-dimensional equation for radial displacement of the tube wall is given in Equation (12):

$$\gamma_T^0 \frac{\partial^2 \bar{R}}{\partial \bar{t}^2} - \frac{1}{\bar{R}} \left(1 - \frac{1}{\bar{R}} \right) - \gamma_f^0 \frac{\varepsilon^2}{\varepsilon_0} \bar{P}^* = 0 \quad (12)$$

Equation (12) presents many asymptotic constraints. Taking into account the Least Degeneration Principle, the above constraints are formalized by the subsequent system of Equation (13), which is the relationship between the fluid and tube properties.

$$\varepsilon^2 \equiv \varepsilon_0 \quad (13)$$

Now, Equation (12) is linearized to yield Equation (14):

$$\begin{aligned} \bar{P}^* &= \varepsilon_0 \tilde{P}^* = \varepsilon^2 \tilde{P}^* \\ \bar{R} &= 1 + \varepsilon_0 \tilde{R} = 1 + \varepsilon^2 \tilde{R} \end{aligned} \quad (14)$$

So, at order 0 in ε_0 (ε^2), the solution of Equation (15) is obtained:

$$\tilde{R} = -\gamma_f^0 \bar{P}^* \quad (15)$$

This model describes a linear relationship between pressure and cross-sectional area, and where γ_f^0 is the proportionality factor, which is a measure of the stiffness of the tube wall. This result is valid only for a polymer structure.

The kinematic condition on the boundary is defined by Equation (16):

$$\tilde{U}_1 = \frac{\partial \tilde{R}}{\partial t} \quad (16)$$

where, $r \approx 1$.

Taking into account the above process, the variation of the radius model is given by Equation (17):

$$\tilde{R}(z,t) = -\gamma_f^0 A_3 \left[\frac{\omega \sqrt{2I\omega} J_0(I\sqrt{2I\omega}/2)}{2J_1(I\sqrt{2I\omega}/2)} (-\gamma_f^0 \omega \sqrt{I\omega} J_0(I\sqrt{I\omega})) \right] e^{I\omega t} \quad (17)$$

$$+ J_1(I\sqrt{I\omega}/2) z - I\sqrt{I\omega} J_0(I\sqrt{I\omega})$$

where, $J_{0,1}$ are the Bessel functions; ω is the fluid frequency; and I is a complex number.

Equation (17) shows that the effects lead to interesting coupled fluid-structure problems. Note that the Bessel function comes up in many engineering applications such as heat transfer, vibrations, stress analysis, and fluid mechanics. In order to validate the preceding results, some examples are presented for which the application ranges of the model were estimated. In these examples, the adimensional frequency was defined as $1 \leq \omega \leq 40$, and the adimensional stiffness factor of the tube wall was defined as $0 \leq \gamma_f^0 \leq 0.08$. The aspect ratio was fixed at $\varepsilon = 0.1$. All of the variables (r , z , and t) were non-dimensional.

Figure 2 clearly shows that the elastic tube was deformed non-axisymmetrically. The region of strongest tube deformation occurred near the tube outlet, where the inside pressure was low. Consequently, the tube shape changed to being nearly elliptical. These results are confirmed by the experimental results obtained by Nahar et al. [19]. The deformation of the tube is affected by several fundamental parameters: γ_f^0 , ε , and the frequency of flow. In fact, Figure 2 (a) shows that the deformation occurs on the right side of the elastic tube , compared to the tube at rest . In the frequency range of $1 \leq \omega \leq 30$, the deformation rate is on the order 12%. Figure 2(b) shows that, in the frequency range of $30 \leq \omega \leq 40$, the deformation rate is on the order of 80% on the right and left sides. But, the deformation rate, at the

top, is on the order of 29.6%, and on the bottom it is on the order of 100%. In a certain range of frequencies, an unstable radial position appears, which separates the region where the strongest deformation is directed towards the wall [20].

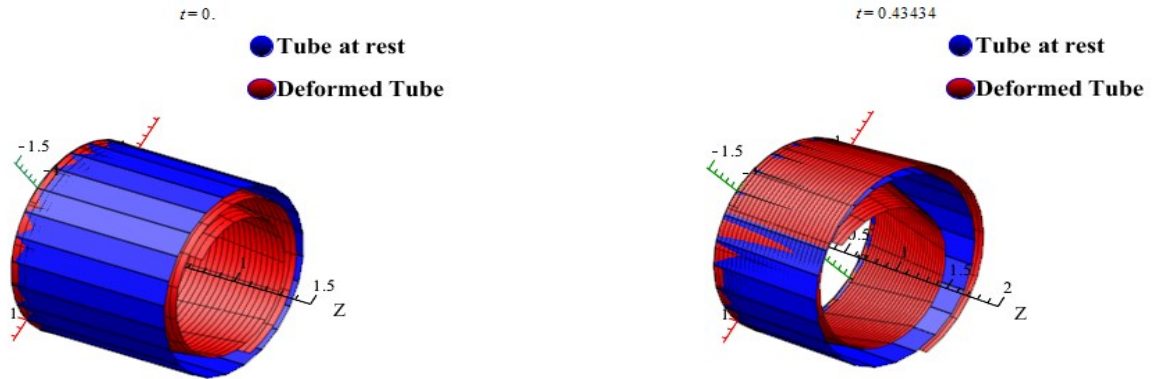
Figure 3 illustrates the influences of the geometrical and the deformation characteristics of the tube on the subsequent development of the initial pressure perturbation. The figure also shows the instabilities of axial flow and developed spontaneous oscillations of the elastic membrane [21, 22]. Figure 4 shows the variation of the wall shear stress with dimensionless time along the z-axis, when the pulsatile laminaire flow has a cosine form. They appear to diminish in the negative sense at the middle of the elastic tube. If Figure 4 is compared with other studies, then the validity of the solution is realized [23].

Conclusion

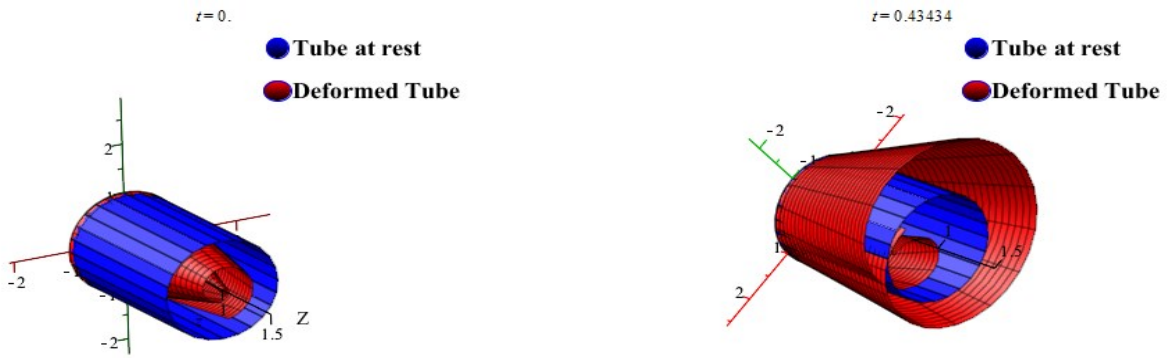
The results obtained in this study globally show the importance of the vibration effect in the modeling of the behaviors and response characteristics of a three-dimensional flexible and elastic tube under laminar flow, and the power asymptotic approach for this modeling. The characteristics usually encountered in fluid-structure interaction are correctly predicted by this current model. When this model is applied to the study of instabilities in flow past deformable solid surfaces, the matching of predictions and numerical simulations with the model remains quantitatively acceptable. Moreover, they allow confirmation of the experimental behavior.

References

- [1] Grotberg, J. B., & Oliver, E. J. (2004). Biofluid mechanics in flexible tubes. *Annual review of fluid mechanics*, 36(1), 121-147.
- [2] Todd, M. S., & Stephen R. Q. (2005). Micro-fluidics: fluid physics at the nanoliter scale. *Reviews of modern physics*, 77(3), 977-1026.
- [3] Eggert, M. D., & Kumar, S. (2004). Observations of instability, hysteresis, and oscillation in low-Reynolds number flow past polymer gels. *Journal of Colloid and Interface Science*, 274, 234-242.
- [4] Babarit, A., Gendron, B., Singh, J., Melis, C., & Jean, P. (2012). *Modélisation numérique et expérimentale d'un système houlomoteur électro-actif déformable*. Paper presented at the '13^{ème} Journées de l'hydrodynamique'. Chatou, France.
- [5] Mitin, A. (2013). Main Gas pipelines: Fracture Resistance Assessment of Pipes. *Journal of Mechanics Engineering and Automation*, 3(3), 127-140.



(a) $20 \leq \omega \leq 30$ at $t = 0$ and $t = 0.43434$



(b) $30 \leq \omega \leq 40$ at $t = 0$ and $t = 0.43434$

Figure 2. Evolution of the Elastic Tube Radius $\bar{R}(z, t)$ in the Frequency Domain Model:

$$1 \leq \omega \leq 30, \gamma_f^0 = 0.08, \varepsilon = 0.1, \text{ and } A_5 = 0.01$$

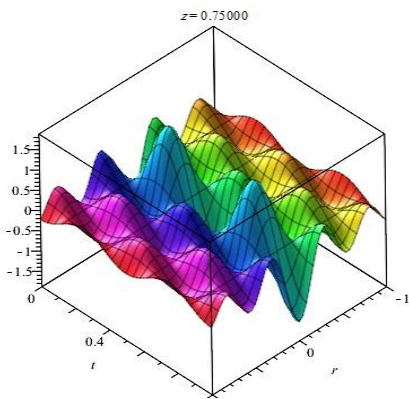


Figure 3: Evolution of the pressure $\bar{P}^*(r, z, t)$ along the z -axis and Behavior at $z = 0.75$ for $-1 \leq r \leq 1$ and $0 \leq t \leq 1$

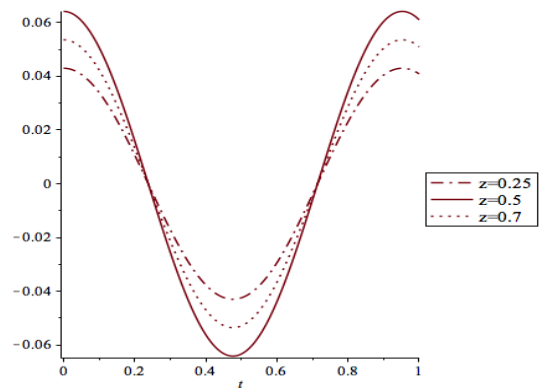


Figure 4. The Variable Radius $\bar{R}(z, t)$ of Cross-Sections, with Scaled Variables $z = 0.25, z = 0.50, z = 0.75,$ and $0 \leq t \leq 1$

- [6] Casson, N. (1959). A flow equation for pigment oil-suspensions of printing ink type. In C.C. Mill (Ed.), *Rheology of disperse systems*. Pergamon press. London.
- [7] Bellet, D. (1973). *Relations entre comportements rhéologiques et échanges thermiques*. Unpublished doctoral dissertation, University of Paul Sebatier, Toulouse.
- [8] Ly, D. P., Bellet, D., Bousquet, A., & Boyer, P. (1981). Ecoulements pulsés de fluide inélastiques en conduites tronconique ou déformable. *Revue de Physique Appliquée*, 16, 323-331.
- [9] Rakotomalala, A. R., & Bellet, D. (1991). Ecoulements transitoires et périodiques de fluides non newtoniens en conduits tronconiques. *Journal de Physique*, 1, 87-102.
- [10] Bahrar, B. (1986). *Influence sur les écoulements transitoires en conduites, des termes d'inertie de la paroi, ainsi des déformations de flexion et de cisaillement*. Unpublished doctoral dissertation, National Institute of Applied Sciences, Lyon.
- [11] Love, A. E. H. (1888). On the Small Free Vibrations and Deformations of the Elastic Shells. *Journal of Philosophical Transaction of the Royal Society*, A (17), 491-549.
- [12] Kirchhoff, V. G. (1850). Uber das Gleichgewicht und Bewegung einer elastischen Scheibe. *Journal of Reine und angewandte mathematik*, 40, 51-88.
- [13] Callegari, A. J., & Reiss, E. L. (1968). Nonlinear boundary value problems for the circular membrane. *Archive Rational Mechanics and Analysis*, 31, 390-400.
- [14] Koiter, W. T. (1970). On the foundations of the linear theory of thin elastic shells. *Proceedings of the Koninklijke Nederlandse Akademie van Wetenschappen*, B73, 169-195.
- [15] Hsu, J. C., & Clifton, R. J. (1956). Wave in a thin-walled tube due to sudden release of radial ring pressure. *Journal of Acoustical Society of America*, 23, 563-568.
- [16] Anliker, M., Rockwell, R. L., & Ogdem, E. (1968). Nonlinear analysis of flow pulses in arteries. *Journal of Fluid Mechanics*, 55, 492-511.
- [17] Moddie, T. B., & Haddow, J. B. (1978). Dispersive effects in wave propagation in thin-walled elastic tubes. *Journal of Acoustical Society of America*, 64, 522-528.
- [18] Serge, L. (2005). *Mecanique des structures Tome 1 : Solides elastiques, plaques et coques*. 'Cépaduès' E., Editor number: 710.
- [19] Nahar, S., Jeelani, S. A. K., & Windhab, E. J. (2012). Influence of elastic tube deformation on flow behavior of a shear thinning fluid. *Journal of Chemical Engineering Science*, 75, 445-455.
- [20] Massimiliano, M. V., Francesco, G., Martien, A. H., & Pier, L. M. (2016). Numerical simulations of deformable particle lateral migration in tube flow of Newtonian and viscoelastic media. *Journal of Non-Newtonian Fluid Mechanics*, 234, 105-113.
- [21] Hilmi, D. (1996). Solitary Waves In Prestressed Elastic Tubes. *Bulletin of Mathematical Biology*, 58(5), 939-955. doi :10.1007/BF02459491.
- [22] Womersley, J. R. (1955). Oscillatory motion of a viscous liquid in a thin walled elastic tube. The linear approximation for long waves. *Journal of Philosophical Magazine*, 46, 199-219.
- [23] Maddah, S., Navidbakhsh, M., & Atefi, G. (2013). Continuous Model for Dispersion of Discrete Blood Cells with an ALE Formulation of Pulsatile Micropolar Fluid Flow in Flexible Tube. *Journal of Dispersion Science and Technology*, 34, 1165-1172.

Biographies

ABDESSAMAD MEHDARI is an aircraft maintenance engineer. He graduated from the Royal Air Force School in 2006. He is responsible for helicopter maintenance and at the same time is a PhD in the Research and Development and Mechanical Multimedia Modeling Team Department, which is a division of the Mohammadia Engineering School at Mohammed V University of Rabat, Morocco. Abdessamad Mehdari may be reached at abdmehdari@gmail.com

MOHAMED HASNAOUI is a full professor of mechanics at the Royal Air Force school of Marrakech. He is the head of the Structure and Material Department. Dr. Hasnaoui may be reached at hasnaouimohamed@hotmail.com

MOHAMED AGOUZOUL is a full professor of mechanics at the Mohammadia Engineering school of Rabat. He is the head of Research and Development and Mechanical Multimedia Modeling Team Department at Mohammed V University of Rabat, Morocco. Dr. Agouzoul may be reached at agouzoul@emi.ac.ma

SHORT-TERM FORECASTING OF WIND POWER GENERATION BY ADAPTIVE NEURAL NETWORKS

Hong Li, The City University of New York; Ali Setoodehnia, ECPI University

Abstract

In this paper, the authors present a method for short-term forecasting of wind power generation using feed-forward multilayer perceptron (FMP) with an adaptive learning algorithm. Wind power, as an alternative to burning fossil fuels, is clean, renewable, and widely distributed in conjunction with other electric power sources to provide an overall reliable supply. But it is also important to have accurate forecasting for power management. A neural network model was designed in this study with a learning algorithm following the analysis of a convergence of the learning process, based on the backpropagation algorithm. The analysis led to conditions of learning factors to guarantee the convergence. The conditions were further extended to a feasible formula for defining an adaptive learning factor through iteration of the learning process. The results of the simulations using wind power data from European countries sourced from the open power system platform are presented here.

Introduction

Wind power has been used as far back as when humans put sails into the wind. As an alternative to burning fossil fuels, it uses air flow through wind turbines to mechanically power generators for electricity. Wind power is renewable, produces no greenhouse gas emissions during operation, uses no water, and has a small footprint. The effects on the environment are far less problematic than those of nonrenewable power sources. Worldwide there are now thousands of wind turbines operating. Wind generation capacity worldwide more than quadrupled between 2000 and 2006, doubling about every three years. Wind power capacity has expanded rapidly and wind energy production is around 4% of total worldwide electricity usage, and is growing rapidly. Rapid growth in wind power, as well as increases in wind generation, requires serious research in various fields. Because wind power is weather dependent, it is variable and intermittent over various time scales. Thus, accurate forecasting of wind power is recognized as a major contribution for reliable large-scale wind power integration. Wind power forecasting methods can be used to plan unit commitment, scheduling and dispatch by system operators, and maximize profit by electricity traders. Numbers from wind power forecasting models have been used in many studies [1]. Artificial neural networks (ANNs) have been proven in many real

-world applications to be useful in various tasks of modeling nonlinear systems such as signal processing, pattern recognition, optimization, and weather forecasting, to name a few. It has drawn many researchers in power generation forecasting. The ANN approach was applied to provide short-term wind power forecasting, based on historical wind power data from Portugal [2]. A new fuzzy-based cost function was proposed with the purpose of having more freedom and flexibility in adjusting ANN parameters used for construction of prediction intervals [3]. In comparison with the other cost functions reported in the literature, this new formulation allows decision makers to apply their preferences for satisfying the prediction internal coverage probability and normalized average width individually.

ANN is a set of processing elements (neurons or perceptrons) with a specific topology of weighted interconnections between these elements and a learning law for updating the weights of interconnection between two neurons. The FMP networks have been shown to obtain successful results in system identification and control [4]. The Lyapunov theorem was used to provide a stability analysis of the backpropagation training algorithm for such networks [5-7]. However, the training process can be very sensitive to initial conditions, such as number of neurons, number of layers, value of weights, and learning factors, which are often chosen by trial and error. In this paper, the authors present a detailed analysis of the FMP architecture and its stability. The backpropagation algorithm was used for learning, or weight adjusting. The least square error function was defined and verified, satisfying the Lyapunov condition, which guarantees the stability of the system. The analysis method defined a range of learning factors [8-9]. Selecting the learning factor within the range at each iteration ensured that the condition for stability was satisfied. A three-layer ANN was trained using the backpropagation algorithm, and was tested on a high volume of historical wind power generation data. The challenge was not in the network architecture itself, but instead in the choice of variables and the information used for training. In this current study, historical data were chosen at 3-hour intervals throughout a 24-hour day. In simulation, instead of selecting a learning factor by trial and error, the authors defined an adaptive learning factor, which satisfied the convergence condition and adjusted the connection weight accordingly. The simulation results are presented here in order to demonstrate the overall performance of the system.

The Basic Principle of FMP

A system identification problem can be outlined as follows: a set of data is collected from the system, including input data and corresponding output data observed or measured as the target outputs of the identification problem. The set is often called a “training set.” A neural network model with parameters, called weights, was designed to simulate the system. When the outputs from the neural network are calculated, an error representing the difference between the target outputs and the calculated outputs from the system is generated. The learning process of the neural network is to modify the network to minimize the error.

Consider a system with N inputs $X = \{X_1, \dots, X_N\}$ and M outputs $Y = \{Y_1, \dots, Y_M\}$. A single-layer system with M outputs can be expressed using Equation (1):

$$Y_{jp} = f(Z) = f\left(\sum_{i=1}^N w_{ij} X_{ip} + \sum_{i=1}^D v_{ij} Y_{j(p-i)}\right) \quad (1)$$

where, w_{ij} is called the connection weight from input X_i to output Y_j ; v_{ij} is called the connection weight of the local feedback at the j th node with the i th delay; $p = 1, \dots, T$; T is the number of patterns; D is the delay used in local feedback; and, $f: \mathbb{R} \rightarrow (-1, 1)$ is a nonlinear sigmoid function defined in Equation (2):

$$f(Z) = \frac{1 - e^{-\theta Z}}{1 + e^{-\theta Z}} \quad (2)$$

where, the constant coefficient, θ , is called the slope.

The backpropagation algorithm is a common algorithm used for training feed-forward multilayer perceptrons. It is a generalized least mean square algorithm that minimizes the mean squared error between the target output and the network output with respect to the weights. The algorithm looks for the minimum of the error function in weight space using the method of gradient descent. The combination of weights, which minimizes the error function, is considered to be a solution of the learning problem. A proof of the backpropagation algorithm was presented as a graphical approach by Rojas [10].

The total error, E , of the network training set is defined by Equation (3):

$$E = \frac{1}{T} \sum_{k=1}^{N_L} \sum_{p=1}^T e_k^2(p) \quad (3)$$

where, $e_k^2(p)$, as shown in Equation (4), is the error associated with the p th pattern at the k th node of the output layer:

$$e_k^2(p) = (d_k(p) - Y_k^L(p))^2 \quad (4)$$

where, $d_k(p)$ is the target output and $Y_k^L(p)$ is the output of network at the k th node.

The learning rule defined in Equations (5) and (6) follows the gradient descent method to update the network connection weights iteratively:

$$\Delta W_j = -\mu \frac{\partial E}{\partial W_j}; j = 1, \dots, M \quad (5)$$

$$\Delta v_j = -\mu \frac{\partial E}{\partial v_j}; j = 1, \dots, D \quad (6)$$

where, $W_j = (w_{1j}, \dots, w_{Nj})$ and $v_j = (v_{j1}, \dots, v_{Dj})$ are weight vectors in the j th node and μ is a constant called the learning factor.

Adaptive Learning Factor

There are no inclusive general concepts of stability for nonlinear systems. Behavior of a system may depend drastically on inputs and disturbances. However, the Lyapunov theory has been used in many studies to examine the stability of nonlinear systems. The definition of the Lyapunov function is a scalar function, $V(x)$, for the system expressed in Equation (7),

$$x(t+1) = f(x(t)), f(0) = 0 \quad (7)$$

if the following conditions hold:

1. $V(0) = 0$ and $V(0)$ is continuous in x
2. $V(x)$ is positive definite; that is, $V(x) \geq 0$ with $V(x) = 0$ only if $x = 0$
3. $\Delta V(x) = V(f(x(t))) - V(x(t))$ is negative definite; that is, $\Delta V(x) \leq 0$ with $\Delta V(x) = 0$ only if $x = 0$

Theorem 1 of the Lyapunov Theorem is where the solution $x(t) = 0$ for the system given by Equation (7) is asymptotically stable if there exists a Lyapunov function of the system in x . The stability of the learning process in an identification approach leads to a better modeling and a convergent process. According to the Lyapunov theorem, determination of stability depends on selection and verification of a positive definite function. For the systems defined by Equations (1) and (2), and assuming that the backpropagation learning rule is applied and the error function and weights updating rule are defined by Equations (5) and (6), then the function, $V(\cdot)$, is defined by Equation (8):

$$V(t) = \frac{1}{N_L T} \sum_{j=1}^{N_L} \sum_{p=1}^T e_k^2(t) \quad (8)$$

Theorem 2 proves that $V(t)$ satisfies the Lyapunov conditions [8], as Equations (9) and (10) assume that the system has one hidden layer:

$$Y_{jp} = f(Z_{jp}^1) = f\left(\sum_{i=1}^N W_{ij}^o X_{ip}^1 + \sum_{i=1}^D V_i^o Y_{j(p-i)}\right) \quad (9)$$

$$X_{ip}^1 = f(Z_{ip}^1) = f\left(\sum_{i=1}^N W_{ij}^h X_{ip}^1 + \sum_{i=1}^D V_i^h X_{j(p-i)}^1\right) \quad (10)$$

Equations (11)-(14) show the gradient descent rule:

$$\Delta W_o^j = -\mu \frac{\partial E}{\partial W_o^j}, j = 1, \dots, M \quad (11)$$

$$\Delta v_o^j = -\mu \frac{\partial E}{\partial v_o^j}, j = 1, \dots, D \quad (12)$$

$$\Delta W_h^j = -\mu \frac{\partial E}{\partial W_h^j}, j = 1, \dots, M \quad (13)$$

$$\Delta v_h^j = -\mu \frac{\partial E}{\partial v_h^j}, j = 1, \dots, D \quad (14)$$

where,

$$W_o^j = (w_{o1}^j, \dots, w_{oN}^j)^T, v_o^j = (v_{o1}^j, \dots, v_{oD}^j)^T$$

$$W_h^j = (w_{h1}^j, \dots, w_{hH}^j)^T, v_h^j = (v_{h1}^j, \dots, v_{hD}^j)^T$$

are weight vectors in the j th node in the output and hidden layers, respectively.

The system is stable when the learning factor from Equations (11)-(14) satisfies the condition shown in Equation (15):

$$\mu < \frac{TM}{2 \sum_{j=1}^M \sum_{p=1}^T \left[\left\| \frac{\partial Y_{pj}}{\partial W_o^j} \right\|^2 + \left\| \frac{\partial Y_{pj}}{\partial v_o^j} \right\|^2 + \left\| \frac{\partial Y_{pj}}{\partial W_h^j} \right\|^2 + \left\| \frac{\partial Y_{pj}}{\partial v_h^j} \right\|^2 \right]} \quad (15)$$

In simulation, the learning factor is generally a predefined constant whose value is selected by trial and error. The simulation performance differed for different values of the learning factor. The learning process may converge or may not reach a satisfactory threshold with different learning factors. From the aforementioned theorem, the convergence is guaranteed if an adaptive learning factor is selected, satisfying the stability condition of Equation (15) at each iteration of the learning factor. For purposes of simplifying the simulation, instead of calculating all $\frac{\partial Y_{pj}}{\partial W^i}$ and $\frac{\partial Y_{pj}}{\partial v^j}$ for

$l = 1, \dots, L; j = 1, \dots, N_L$, the following corollary provides an extended condition with more restriction but fewer calculations.

Consider infinite norm notation for any vector $X = \{x_1, x_2, \dots, x_n\}$ that $\|X\|_\infty = \max_{1 \leq i \leq n} \{x_i\}$; for simplicity, the notation $\|*\|$ was used in this paper and represents). Applying infinite norm from Equation (15) and using the notation $|v_j^l| = \sum_{d=1}^{Dv} v_{jd}^l$, the extended conditions are given as follows:

Corollary 1: The system defined in Equations (9) and (10) converges if the learning factor from Equations (11)-(14) satisfies the conditions expressed in Equations (16) and (17):

$$2 - \theta |v_j^o| > 0 \quad (16)$$

$$\mu < \frac{(2 - \theta |v_j^o|)^2}{4\theta(2 + \theta(|w^o| - |v_j^o|))} \quad (17)$$

Simulation

The changing energy landscape requires rigorous analysis to support a robust investment and policy decisions. Power systems are complex; hence, researchers and analysts often rely on large numerical computer models for a variety of purposes, ranging from price projections to policy advice and system planning. Such models include unit commitment, dispatch, and generation expansion models. These models require a large amount of input data, such as information about existing power stations, interconnector capacity, yearly electricity consumption, and ancillary service requirements, but also (hourly) time series of the load, wind and solar power generation, and heat demand.

Fortunately, most of these data are publicly available from sources such as transmission system operators, regulators, or industry associations. The open power system data platforms provide free and open data of the European power system with restricted use for non-commercial applications. The open power system data are implemented by four institutions: DIW Berlin, Europa-Universität Flensburg, Technical University of Berlin, and Neon Neue Energieökonomik, and funded by the German Federal Ministry for Economic Affairs and Energy. It contains time-series data relevant for power system modeling, including hourly electricity consumption for 36 European countries, and wind and solar power generation from German transmission system operators. The simulations of this study used German wind power generation data available from 2005-2015

for ANN training and mainly demonstrated that the enhanced learning algorithm may avoid many trial-and-error scenarios for selection of learning factors. In general, the initial weights are randomly selected and a learning factor is predefined. The performance of learning is sometimes very volatile, due to selection of the learning factor. To find the optimal fit, trial and error is a common practice that runs the simulation with different values of the learning factors. In this current study, an upper boundary of learning factors, see again Equation (17), was derived from the theory of convergence. At iteration of network training, the norm of weights was calculated and a learning factor was defined to satisfy the convergence condition.

A three-layer neural network structure was defined with eight inputs, six and four nodes in the hidden layers, and one output. For hourly wind power generation as an output, eight inputs were wind power generation at three-hour intervals. Data from 2013 and 2014 were used to train the ANN model. The data from 2015 were used to test the ANN model's performance. Input and output data were normalized to range from 0 to 1. After the ANN network was trained, the forecasts for wind power generation were calculated using the ANN network and then denormalized and compared with the actual wind power generation in 2015. With the constant learning factor, two values were used for the learning trials: 0.05 and 0.1. After several attempts, with the slope set at 0.7, the learning factor set at a constant 0.05, the momentum term set at 0.1, and random-generated initial weights, the system reached an absolute error of 0.028 after 100,000 iterations. Figures 1 and 2 show the error behaviors.

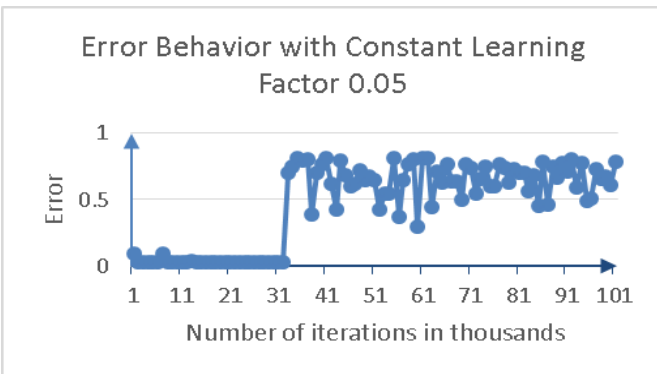


Figure 1. Error Behavior of Neural Network Training with a Constant Learning Factor of 0.05

Applying the same values of slope (0.7) and momentum (0.1), and with initial learning factors of 0.1 and 0.05, the error of neural network learning steadily decreased as the adaptive learning factor was applied at each iteration. Figures 3 and 4 show the error behaviors of learning with the initial learning factors of 0.05 and 0.1, respectively.

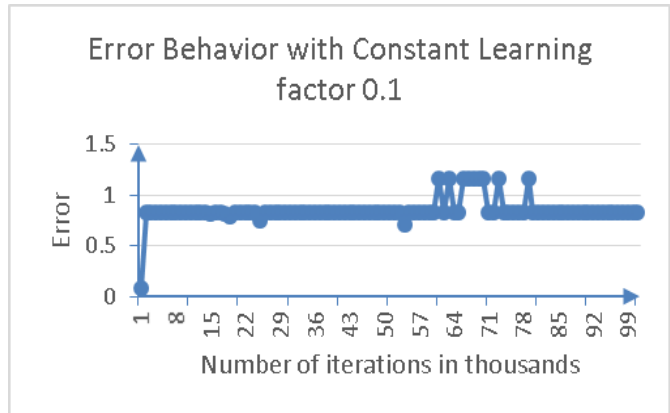


Figure 2. Error Behavior of Neural Network Training with a Constant Learning Factor of 0.1

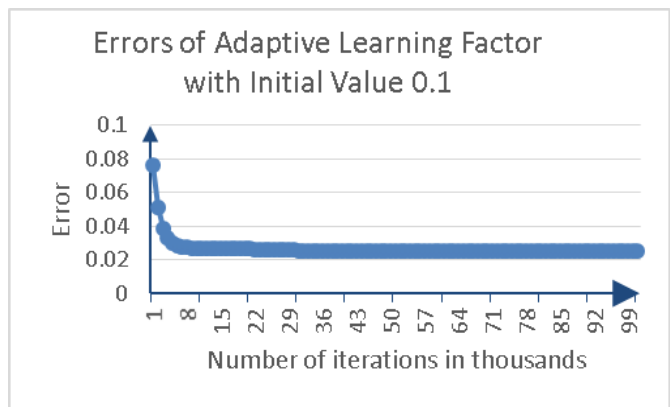


Figure 3. Error Behavior of Neural Network Training with Adaptive Learning Factor Initially Set To 0.1

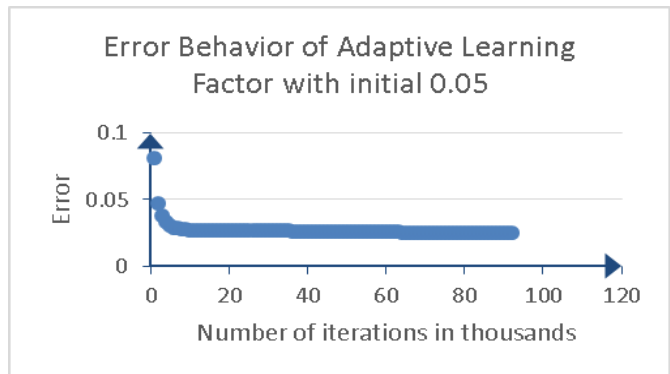


Figure 4. Error Behavior of Neural Network Training with Adaptive Learning Factor Initially Set To 0.05

It was observed that error behaviors did not differ with different initial values of learning factor. However, the constant learning factor caused volatile performance of training. Figures 5-10 show wind power forecasting for 2015 from the neural network model trained with slope 0.7, momentum 0.1, and an adaptive learning factor starting with 0.05.

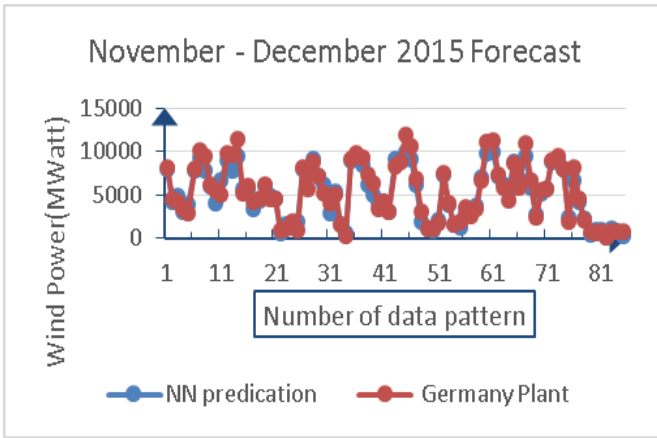


Figure 5. NN Predication and German Plant for November–December 2015

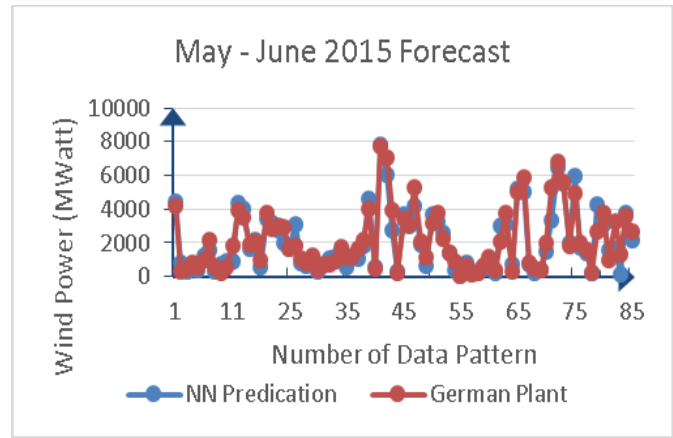


Figure 8. NN Predication and German Plant for May–June 2015

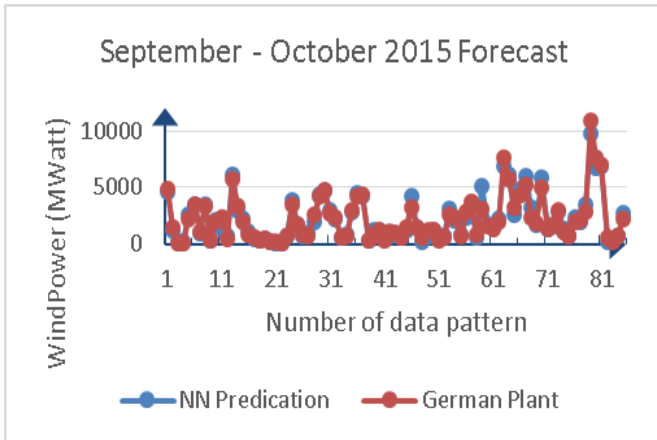


Figure 6. NN Predication and German Plant for September–October 2015

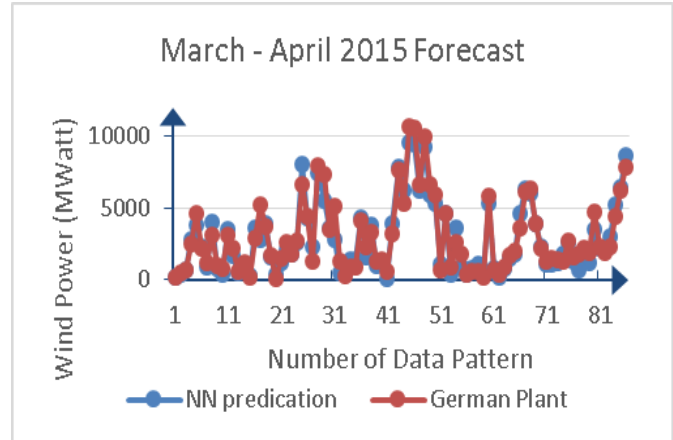


Figure 9. NN Predication and German Plant for March–April 2015

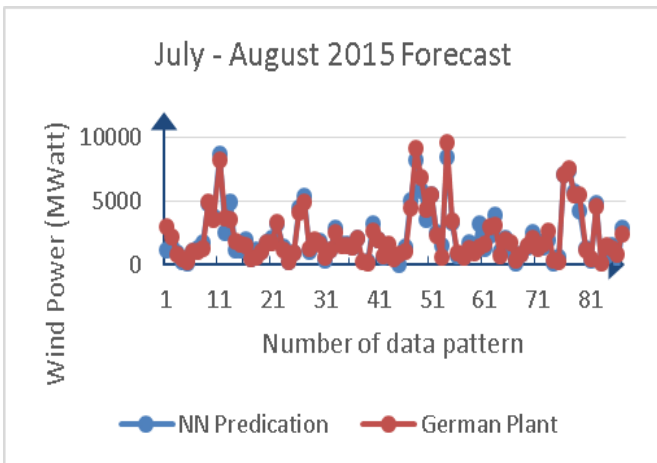


Figure 7. NN Predication and German Plant for July–August 2015

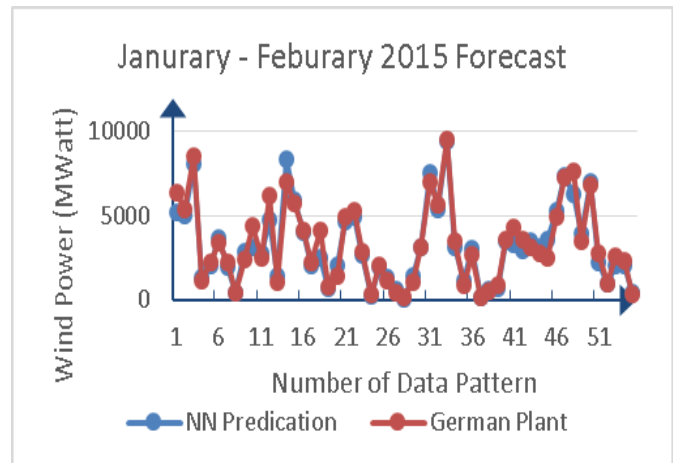


Figure 10. NN Predication and German Plant for January–February 2015

Conclusion

This current study focused on wind power generation forecasting using neural networks. The historical data of time-series wind power generation were sourced from the open power system platform. The data were available from 2005 for hourly wind power generation. Adaptive learning factors were defined at each iteration of training, following the analysis of a convergence theory. The analysis resulted in a condition that provided an upper boundary of the learning factor. Instead of selecting a constant learning factor by trial and error, an adaptive learning factor was calculated at each iteration, satisfying the convergence condition. Furthermore, a more simplified condition was used to provide a feasible implementation of the adaptive learning factor. An adaptive learning factor derived from analysis of stability was selected at each iteration of the learning process, satisfying the convergence condition to avoid unstable phenomena. The simulation results were based on the data from a German wind power plant. The error behaviors were demonstrated for training with an adaptive learning factor as well as with a selected constant learning factor. The comparison demonstrated that an arbitrarily chosen learning factor leads to unstable identification of the considered system; however, an adaptive learning factor satisfying the conditions ensures the stability of the identification system. The neural network was trained with historical data from 2013–2014 and tested for forecasting performance with data from 2015.

References

- [1] Wang, X. Guo, P. , & Huang, X. (2011). A review of wind power forecasting models, *Energy Procedia Elsevier*, 12 ,770-778.
- [2] Catalao, J., Pousinho, H., & Medes, V. (2009). An Artificial Neural Network Approach for Short Term Wind Power Forecasting in Portugal, *Engineering Intelligent System*, 1, 5-11.
- [3] Kavousi-Fard, A., Khosravi, A., & Nahavandi, S. (2016). A New Fuzzy-Based Combined Prediction Interval for Wind Power Forecasting, *IEEE Transaction on Power Systems*, 31(1), 18-26.
- [4] Korkobi, T., Djemel, M., & Ctourou, M. (2008). Stability Analysis of Neural Networks-based System Identification. *Modeling and Simulation in Engineering*, 2008, Article ID 343940
- [5] Akea, H., Alassar, R., & Covachev, V. (2005). Stability of Neural Networks with Time Varying Delays in the Presence Impulses. *Advances in Dynamical Systems and Application*, 1(1), 1-15.
- [6] Choon Ki Ahn, H. (2012). Stability Conditions for Fuzzy Neural Networks. *Advances in Fuzzy Systems*, Article ID 281821.
- [7] Liang, G. (2010). Global Asymptotically Stability of Cellular Neural Networks with Time-varying Delay. *2010 8th World Congress on Intelligent Control and Automation*, (pp. 5031-5036).
- [8] Li, H. (2014). Adaptive Learning Factor of Back-propagation in Feed Forward Neural Networks. *International Journal of Modern Engineering*, 14(2), 47-53.
- [9] Li, H., & Setoodehnia, A. (2014). Convergence Analysis of Adaptive Recurrent Neural Network. *International Journal of Engineering Research and Applications*, 4(6), 48-53.
- [10] Rojas, R. (1996). *Neural Networks*, Springer-Verlag.
- [11] Sontag, E.D. (1998). *Mathematical Control Theory*, Springer-Verlag, New York.

Biographies

HONG LI is an associate professor and Chairperson of the Department of Computer Systems Technology at New York City College of Technology of the University of New York. She earned her PhD in Mathematics from the University of Oklahoma. Her research interests include mathematical modeling, applications for artificial neural networks, and software development. Dr. Li may be reached at hli@citytech.cuny.edu

ALI SETOODEHNIA is a faculty member in Electrical Engineering Technology at ECPI University. He earned his PhD in Electrical Engineering from the University of Oklahoma. Dr. Setoodehnia's research interests include artificial neural networks, power systems, and system identification. Dr. Setoodehnia may be reached at asetoodehnia@ecpi.edu

INSTRUCTIONS FOR AUTHORS: MANUSCRIPT SUBMISSION REQUIREMENTS

The INTERNATIONAL JOURNAL OF MODERN ENGINEERING is an online/print publication. Articles appearing in IJME are centered around engineering-related research. All submissions to this journal, including manuscripts, peer-reviews of submitted documents, requests for editing changes, as well as notification of acceptance or rejection, will be handled electronically.

All manuscript submissions must be prepared in Microsoft Word (.doc or .docx) and contain all figures, images and/or pictures embedded where you want them and appropriately captioned. It is highly recommended that you print, in color, all images in your manuscript in order to determine their quality; the journal editors will be doing the same during the editorial review of your manuscript. If your manuscript is accepted for publication, you will receive instructions regarding all required revisions and the submission of higher-quality images. If you are able to provide such images, it's possible that you will be asked to remove them from the manuscript.

Tables must be created directly in Word, not imported as pictures, and be enclosed on all sides. If you have graphs or charts, they should also be created directly in Word, if possible. If that is not possible, the editor will discuss further options with you. Please be conscientious of the quality of your images and remember that all online and print copies of issues of IJME are in color.

The editorial staff of the International Journal of Modern Engineering reserves the right to format and edit any submitted document in order to meet publication standards of the journal. Included here is a summary of the formatting instructions. You should, however, review the "[sample Word document](#)" included on our website (http://ijme.us/formatting_guidelines) for a detailed analysis of how to correctly format your manuscript.

The references included in the References section of your manuscript must follow APA-formatting guidelines. In order to help you, the sample Word document also includes numerous examples of how to format a variety of sources. If you have a reference source for which you are not able to find the correct APA format, contact me for help anytime (philipw@bgsu.edu). Keep in mind that an incorrectly formatted manuscript will be returned to you, a delay that may cause it to be moved to a subsequent issue of the journal.

1. Word document page setup: Top = 1", Bottom = 1", Left = 1.25", Right = 1.25". This is the default setting for Microsoft Word.
2. Page breaks, tabs, and indents: Do not use page breaks or tabs. Do not use spaces for paragraph indents; use the scroll markers, as shown here. 
3. Paper title: Centered at the top of the first page with a 22-point Times New Roman (Bold), Small-Caps font.
4. Body fonts: Use 10-point Times New Roman (TNR) for body text throughout (1/8" paragraph indentation); 9-point TNR for author names/affiliations under the paper title; 16-point TNR for major section titles; 14-point TNR for minor section titles; 9-point TNR BOLD for caption titles; other font sizes may be noted in the sample Word document.
5. Images: All images should be included in the body of the document. It's ok for images or tables to be centered on the page, and not confined to the 2-column format, if necessary. Irrespective of how Word moves any given image/table, be certain that all captions are located in the document where the images/tables should ultimately be placed. If you are required to submit additional high-quality images, they must be saved/sent as individual files (one image per file) and labeled using the following format, where the first portion of the title is your manuscript number:
M15-F-10 Figure 4
6. In-text referencing: List and number each reference when referring to them in the body of the document (e.g., [1]). In-text references must be in numerical order and follow entries in the References section. Again, see the sample Word document on our website for specifics. Please do not use the End-Page Reference utility in Microsoft Word.
7. Tables and figures: Captions for tables must be above the table, while captions for figures are below; all captions are left-justified unless the table or figure is centered on the page, in which case the caption should also be centered.
8. Page limit: Manuscripts should not be more than 15 pages (single-spaced, 2-column format).
9. Page numbering: Do not use page numbers.



www.ijeri.org

Print ISSN: 2152-4157
Online ISSN: 2152-4165



www.iajc.org

INTERNATIONAL JOURNAL OF ENGINEERING RESEARCH AND INNOVATION

ABOUT IJERI:

- IJERI is the second official journal of the International Association of Journals and Conferences (IAJC).
- IJERI is a high-quality, independent journal steered by a distinguished board of directors and supported by an international review board representing many well-known universities, colleges, and corporations in the U.S. and abroad.
- IJERI has an impact factor of **1.58**, placing it among an elite group of most-cited engineering journals worldwide.

OTHER IAJC JOURNALS:

- The International Journal of Modern Engineering (IJME)
For more information visit www.ijme.us
- The Technology Interface International Journal (TIIJ)
For more information visit www.tiij.org

IJERI SUBMISSIONS:

- Manuscripts should be sent electronically to the manuscript editor, Dr. Philip Weinsier, at philipw@bgsu.edu.

For submission guidelines visit
www.ijeri.org/submissions

TO JOIN THE REVIEW BOARD:

- Contact the chair of the International Review Board, Dr. Philip Weinsier, at philipw@bgsu.edu.

For more information visit
www.ijeri.org/editorial

INDEXING ORGANIZATIONS:

- IJERI is currently indexed by 16 agencies.
For a complete listing, please visit us at www.ijeri.org.

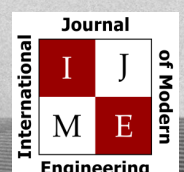
Contact us:

Mark Rajai, Ph.D.

Editor-in-Chief
California State University-Northridge
College of Engineering and Computer Science
Room: JD 4510
Northridge, CA 91330
Office: (818) 677-5003
Email: mrajai@csun.edu



www.tiij.org



www.ijme.us

THE LEADING JOURNAL OF ENGINEERING, APPLIED SCIENCE AND TECHNOLOGY

The latest impact factor (IF) calculation (Google Scholar method) for IJME of 3.0 moves it even higher in its march towards the top 10 engineering journals.

**IJME IS THE OFFICAL AND FLAGSHIP JOURNAL OF THE
INTERNATIONAL ASSOCIATION OF JOURNALS AND CONFERENCE (IAJC)**

www.iajc.org



The International Journal of Modern Engineering (IJME) is a highly-selective, peer-reviewed journal covering topics that appeal to a broad readership of various branches of engineering and related technologies. IJME is steered by the IAJC distinguished board of directors and is supported by an international review board consisting of prominent individuals representing many well-known universities, colleges, and corporations in the United States and abroad.

IJME Contact Information

General questions or inquiries about sponsorship of the journal should be directed to:

Mark Rajai, Ph.D.

Editor-in-Chief

Office: (818) 677-5003

Email: editor@ijme.us

Department of Manufacturing Systems Engineering & Management

California State University-Northridge

1811 Nordhoff St.

Northridge, CA 91330